universität wien

MASTERARBEIT / MASTER'S THESIS

Titel der Masterarbeit / Title of the Master's Thesis

„An Examination of Unsupervised Clustering Strategies with Application to the Human Amygdala"

verfasst von / submitted by

Niklas Leitner, BSc.

angestrebter akademischer Grad / in partial fulfilment of the requirements for the degree of

Master of Science (MSc)

Wien, 2023 / Vienna 2023

Studienkennzahl lt. Studienblatt / degree programme code as it appears on the student record sheet:	UA 066 840
Studienrichtung lt. Studienblatt / degree programme as it appears on the student record sheet:	Masterstudium Psychologie UG2002
Betreut von / Supervisor:	Univ.-Prof. Dr. Claus Lamm
Mitbetreut von / Co-Supervisor:	Ronald Sladky, Bakk.techn. MSc PhD

Abstract

The human amygdala has long been subject of extensive investigation, yielding numerous structural and functional models. In terms of functionality, the amygdala is mostly associated with mechanisms underlying fear in both humans and animals. *In vivo* examination of the human amygdala proves more challenging than in animals, since fMRI group analysis underlies spatial inaccuracies, which interfere with the identification of functionally distinct subregions. This thesis aims to investigate the usefulness of two unsupervised clustering algorithms to obtain functional parcellations of the human amygdala and compares the functional connectivity of obtained subregions to the one of the Jülich Brain Atlas. Analysis of high resolution resting state fMRI data of 123 individuals showed that the used clustering algorithms were able to derive parcellations, that are definitely comparable to the Jülich Brain Atlas. Deviations of structure occurred in the smaller centromedial and superficial amygdala. However, functional connectivity suggests that the clustered subregions are a better fit to the fMRI data at hand. Although some inconsistencies with literature in terms of functionality remain, unsupervised clustering has proven to be a feasible method for obtaining functional parcellations of the human amygdala, which can be built upon in the future.

Die menschliche Amygdala ist seit langem Gegenstand umfangreicher Untersuchungen, die zu unterschiedlichen strukturellen und funktionellen Modellen geführt haben. Was die Funktionalität betrifft, so wird die Amygdala sowohl bei Menschen als auch bei Tieren meist mit den kognitiven Prozessen von Angst in Verbindung gebracht. Die *in vivo* Untersuchung der menschlichen Amygdala erweist sich als schwieriger als bei Tieren, da die fMRI Gruppenanalyse mit räumlichen Ungenauigkeiten behaftet ist, die die Identifizierung von funktionell unterschiedlichen Unterregionen beeinträchtigen. Ziel dieser Arbeit ist es, die Nützlichkeit von zwei unüberwachten Clustering-Algorithmen zu untersuchen, um funktionelle Parzellierungen der menschlichen Amygdala zu erhalten und die funktionelle Konnektivität der erhaltenen Subregionen mit der des Jülich Brain Atlas zu vergleichen. Die Analyse von hochauflösenden fMRT-Daten von 123 Individuen im Ruhezustand zeigte, dass die verwendeten Clustering-Algorithmen in der Lage waren, Parzellierungen zu generieren, die durchaus mit dem Jülich Brain Atlas vergleichbar sind. Strukturabweichungen traten in der zentromedialen und in der oberflächlichen Amygdala auf. Die funktionelle Konnektivität legt jedoch nahe, dass die geclusterten Subregionen besser zu den vorliegenden fMRI-Daten passen. Obwohl einige Unstimmigkeiten mit der Literatur in Bezug auf die Funktionalität bestehen bleiben, hat sich das unüberwachte Clustering als vielversprechende Methode zur Gewinnung von funktionellen Parzellierungen der menschlichen Amygdala erwiesen, auf der in Zukunft aufgebaut werden kann.

Table of Contents

List of Figures

List of Tables

1. Introduction

1.1. Investigating Structure and Function

The human amygdala is a comparably small almond-shaped area in the brain, located in the medial temporal lobe and was first described at the beginning of the 19th century by the German physiologist Karl Friedrich Burdach (Burdach, 1826). However, the region initially identified by Burdach as a cytoarchitectonic independent area was actually just a region now often referred to as the basolateral amygdala and did not include all the areas that are associated with the amygdala today (McDonald, 2003). The basolateral amygdala is only one subdivision among several others, although it might be the largest and easiest to locate. In the 50 years following its partial discovery, first attempts were made to microscopically examine the human amygdala to find histological tissue sections (Swanson & Petrovich, 1998). The rising interest in parcellating the amygdala led to an increase in structural differentiation. About 100 years after Burbach's discovery, Johnston (1923) identified several nuclei that he associated with the "amygdaloid complex", examining the region in a selection of mammalian species. He introduced an extensive and fundamental description of the formation, that is the most commonly referred to until this day. Johnston identified six main nuclei, namely the central, medial, cortical, accessory, basal and lateral nuclei. The first three being declared as a primitive group associated with the olfactory system and the latter three being a phylogenetically more recently developed group (Swanson & Petrovich, 1998). This nomenclature chosen by Johnston is just one amongst many naming systems that arose over time and the specific areas that he chose to associate with each nuclei vary across today's available literature (Heimer et al., 1999; De Olmos, 2004; Yilmazer-Hanke, 2012). Since the first half of the twentieth century, when Johnston made his postulation, a lot more data regarding anatomy and functionality of the amygdala and its surrounding regions has been accumulated. A common interpretation that this data yields is that the amygdaloid complex constitutes a heterogeneous accumulation of expanses of these surrounding brain areas, with the central and medial nuclei and anterior area being an extension of the striatum. The nucleus of the lateral olfactory tract, cortical nucleus, postpiriform and piriform amygdalar areas are being associated with the olfactory cortex and the lateral, basal and posterior nucleus being a ventromedial extension of the claustrum (Swanson & Petrovich, 1998).

In the past five decades the interest in classifying the amygdala in terms of cytoarchitecture has been replaced by the growing importance of comprehensive investigation of its functionality. The most common association today in this regard is its involvement in mechanisms underlying emotions (LeDeux, 2000). The first ones that addressed these mechanisms were William James and C. G. Lange (James, 1884; Lange 1887), who formulated the James-Lange theory of emotion. The theory postulated that emotions are cognitive responses that are evoked by the physiological responses of the body and had nothing to do with the amygdala. Even though it was discovered earlier that century, it was not considered to be involved in the mechanisms underlying emotions. Over the next 75 years progressing investigation associated emotional responses more and more with dedicated areas in the brain and led to the concept of the limbic system, which still did not include the amygdala (Cannon, 1927; Papez, 1937; McLean, 1949; Sah et al., 2003). When Klüver and Bucy (1939) conducted an experiment that aimed to investigate the effects of medial temporal lobe lesions in monkeys, they observed changes in emotional behaviour, but did not attribute these effects directly to the amygdala, possibly because the lesion also included parts of the hippocampus and surrounding cortical areas (Sah et al., 2003). It was not until Weißkrantz (1956) that the amygdala's role in emotional processing was first consolidated, by replicating the findings of Klüver and Bucy with lesions targeting the amygdala directly. Further investigations led to the increasing popularity and development of fear conditioning tasks. Especially in rodents, amygdala's involvement in fear responses can be studied thoroughly with *in vivo* methods not applicable to humans like nuclei specific neurotoxic lesions and harmful conditioning stimuli (Goosens & Maren, 2001). Due to the simplicity and effectiveness of fear conditioning in rodents, paired with the physiological similarities of fear in humans and rodents (Phelps & LeDoux, 2005), the amygdala has gotten a lot of attention. This widespread interest in investigating the amygdala's association with fear processing has greatly reinforced the argument for its involvement in rodents and humans. Although these neural systems of fear can be studied in detail in rodents, they only provide a basis for our understanding how these mechanisms unfold in the human brain and cannot be taken as fully analogous (Davis et al., 2010). Furthermore, this influx in fear conditioning research has resulted in an abundance of studies highlighting the amygdala's involvement in today's literature, a circumstance that can lead to misinterpretation on a meta-analytical level. For instance, if one would search for the term "fear" on the website www.neurosynth.org (Yarkoni et al., 2011), a synthesized activation

map from 363 studies done on humans will appear, that shows highest statistical association with an area encompassing the entire amygdala. Of course, the amygdala is neither the only region involved in fear processing, nor does it function as one homogenous region. It is the nature of the meta-analytical approach which suggests that the considered studies yield activation most prominently in the whole amygdaloid complex. The key takeaway from this example is not the amygdala is consistently the most active area in studies examining fear. It rather emphasizes the misconception that the entire amygdaloid complex is associated with the mechanisms of fear. A notion that is a distortion of contemporary understanding of the amygdala's functionality. The modern understanding is reflected in recent literature where the amygdala is treated as a conglomerate of different nuclei that are distinct from each other through intra- and interconnectivity with other brain regions (LeDoux, 2007). Most commonly, the amygdala is segmented into three functionally distinct subdivisions. The Jülich probabilistic brain atlas (Amunts et al., 2020), which is based on cytoarchitectonic examination of humans, declares these three subdivisions as the laterobasal group, the centromedial group and the superficial group. This specific nomenclature is the one constituted by Heimer et al. (1999). In the Jülich brain atlas the superficial group includes the anterior amygdaloid area, the amygdalo-piriform transition area, the amygdaloid-hippocampal area and the ventral and posterior cortical nuclei. The centromedial group entails the central nucleus, as well as the medial nucleus and the laterobasal group defines the lateral, basolateral, basomedial and paralaminar nuclei (Amunts, 2005). The Jülich Brain Atlas will be used in this thesis as reference along data analysis due to its wide use in recent literature regarding the human amygdala (Roy et al., 2009; Eickhoff et al., 2018; Bzdok et al., 2013). Although the atlas is widely used, a lot of advancements and attempts in structural investigation have brought forth several other valid options (Hawrylycz et al., 2012, Tyszka & Pauli, 2016) and the best fitting number of subdivisions, as well as which specific nuclei of the amygdala they entail, remains a topic of debate until this day. However, even though these mappings are based on human brain tissue examinations and most likely reflect the amygdala's functional parcellation, they do not fully describe it. In other words, *in vivo* investigation of the human amygdala is a challenging task compared to tissue segmentation or *in vivo* investigation of rodents amygdala.

1.2. Contemporary Problems

Even if there would exist an anatomical correct and detailed model of the amygdala, the application to fMRI data would still presents several challenges and limitations. Histological differences in the tissue would not automatically mean that the BOLD signal would follow these borders, due to characteristics of both data acquisition and analysis. Concerning data acquisition, the problem lies within the spatial resolution of fMRI scanners. A wide range of fMRI studies collect their data at a $3\times3\times3mm^3$ voxel size, a resolution that cannot capture a lot of the more fine grained differences in tissue. Additionally, the probabilistic nature of fMRI group analysis, makes it even harder to take full advantage of maximally detailed parcellations, because the investigated region is not spatially aligned across all examined subjects. For capturing functionally distinct subregions which are detectable with fMRI and fine grained enough to yield robust findings, other solutions have to be applied. A promising way to tackle this issue is the use of unsupervised clustering algorithms (Thirion et al., 2014). As can be inferred from their name these algorithms work in an unsupervised manner, meaning that they do not take any additional information into account, except the data they are given and the number of clusters into which the data should be divided. The idea behind using these algorithms is that they might possess the ability to accommodate for the spatial variability of brain regions between subjects, simply because they group voxels with similar signals, doing so without spatial constraints. This means that it might be possible to obtain functional parcellations of certain brain regions that fit the used sample better than a refence atlas, due to their ability to react to possible spatial inaccuracies which change from sample to sample, invoked by the miss-alignment of investigated regions.

A former study conducted by Zhang et al. (2018) has shown that the implementation of semi-supervised clustering of the human amygdala's resting state signal is a powerful tool to functionally parcellate the structure. In this semi-supervised approach the clustering algorithm was informed by the Jülich brain atlas' amygdala subregions, by using the centre of mass of each subregion as a reference point for the algorithm. Another study using semi-supervised clustering informed by the Jülich brain atlas was done by Cheng and Fan (2014) who found similar promising results and argue that this approach yields more favourable outcomes than unsupervised clustering methods. However, informing the algorithm with subregions of a reference atlas might enhance the algorithm's ability to find clusters similar to these

subregions, but also imposes a bias on the results. With the array of nomenclatures and parcellations of the amygdala in the available atlases, this does not clarify what the real intrinsic functional parcellation of the human amygdala looks like. For this reason, this thesis aims to test whether a) unsupervised clustering algorithms are viable tools to obtain a valid functional parcellation of the human amygdala using resting-state fMRI that fit the data at hand better than the Jülich brain atlas and b) how the results of two different clustering algorithms compare to each other.

1.3. Clustering Algorithms

To parcellate the amygdala into subdivisions, two of the most common clustering algorithms were selected – k-means clustering and agglomerative hierarchical clustering. The reason that these two have been chosen is they are being commonly used to cluster resting state fMRI signals (Blumensath et al., 2013; Mezer et al., 2009; Thirion et al., 2014). In principle, these algorithms work in a similar fashion. Data in the format of a two-dimensional matrix of *samples* × *features* is passed to the algorithms and the attributes of the data largely determine the results. Both algorithms will return the data in divided subsets of datapoints that they declare as more similar to each other than to datapoints that are placed in other subsets. The datapoints mentioned here correspond to the *samples* in the matrix and are compared in similarity along their *features*. To put this into the perspective of fMRI data, the *samples* are the voxels of the region that is to be clustered and the *features* are the timeseries of the BOLD-signal of each voxel. Although both algorithms mathematically compare the similarity between datapoints there are some fundamental differences, one of them being how they arrive at the number of clusters that is being returned. In the following section the formalism of both algorithms will be explained to give a better understanding of these differences.

1.3.1. K-Means Clustering

The k-means clustering algorithm is used to divide a dataset into a predefined number of clusters and was firstly developed by Lloyd (1982). It tries to find local minima in the data by reducing the sum of squared distances ϕ between each point and its closest centre-point. This can be expressed with the function:

$$\phi = \sum_{x \in X} \min_{c \in C} \|x - c\|^2$$

In this equation we see that the goal is to minimize the *total error* ϕ, which is the sum of the minimum squared distances of data-points x and centroids (points in centre of mass) c for each Cluster C. To accomplish this goal, the algorithm looks for the optimal centroids of each cluster in an iterative way.

For the algorithm to work we have to pass it a predefined number of clusters k, as it does not make any estimation about the optimal number of clusters (hence, the name k-means). Then the k-means clustering follows a defined set of steps, until a certain criteria is met. The steps as described by Arthur & Vassilvitskii (2007) are as follows:

1. First the algorithm starts by randomly placing k initial centers $C = \{c_1, \dots, c_k\}$ in the data.
2. Then for each $i \in \{1, \dots, k\}$ it assigns the closest points in X to c_i, to cluster C_{i}. As mentioned above each data point can only be assigned to one cluster.
3. After this a new centroid is defined, based on the current distribution of data points in the cluster C_i: $c_i = \frac{1}{\mathrm{C_i}} \sum_{x \in C_i} x$.
4. Now steps two and three are repeated until the centres C no longer change their location.

Assigning the datapoints to a cluster in Step 2 results in the data-clusters, by giving each datapoint of a cluster the same label. In terms of fMRI data this means that each voxel gets a number from 1 to k.

The implementation of the k-means clustering algorithm was done with the Python library scikit-learn (Pedregosa et al., 2018). The exact algorithm that scikit-learn uses as a default is the “greedy kmeans++” algorithm by Arthur & Vassilvitskii (2007). The k-means++ algorithm differs from the standard k-means algorithm above in Step 1. Instead of arbitrarily choosing all initial centroids, only the first one is chosen randomly. The placement of each following centroid is based upon the location of the first one by a method called “D^2 weighting” which they presented in their work cited above. The “greedy version” of the k-means++ algorithm is another optimization in regard to the centroid selection. It samples more than one centroid at each step and chooses the best option among those initialized centroids (Grunau et al., 2022).

1.3.2. Hierarchical Clustering

Hierarchical clustering can be used for the same purposes as k-means clustering but it differs substantially in its functionality. One of the biggest differences is that it does not need a

predefined number of clusters. The way it works is that it either merges or splits nested clusters to the point it has merged the data into only one cluster or until it has split the data into all its smallest possible parts. The approach used in this work is utilizing the merging-approach and it is called hierarchical agglomerative clustering (HAC). The implementation was done similarly to the k-means implementation, with the Python library scikit-learn. Among the different versions of the algorithm that are offered in scikit-learn, the default "ward" linkage method was chosen. The linkage method relates to the strategy for merging similar datapoints. The "ward" method chooses variance as its metric to minimize the sum of squared differences. In other words Ward's algorithm (Ward, 1963) merges two clusters if the resulting combined cluster minimizes the sum of squared differences across all clusters. This happens in a step by step iterative fashion, where at each step two clusters are merged into one until only the whole dataset results in one cluster. Thirion et al. (2014) described this procedure with its application to resting state fMRI formally in the following way. We denote the two clusters under inspection as c_1 and c_2. Our goal is to merge the clusters that reduce the difference $\Delta(c_1, c_2)$:

$$\Delta(c_1, c_2) = \sum_{j \in c_1 \cup c_2} |y^j - \langle Y \rangle_{c_1 \cup c_2}|_2^2 - \left(\sum_{j \in c_1} |y^j - \langle Y \rangle_{c_1}|_2^2 + \sum_{k \in c_2} |y^k - \langle Y \rangle_{c_2}|_2^2 \right)$$

In this equation Y is a vector of our voxel timeseries y, $\mathrm{Y} = [\mathrm{y}^1, \dots, \mathrm{y}^{\mathrm{Q}}]$, where Q is the amount of voxels in our data. $\langle Y \rangle_c$ is the average signal of the voxels in the denominated cluster. The equation compares the sum of squared (Euclidean) distances between each voxel's timeseries and the average signal of a designated group of voxels. The groups of voxels compared are voxels in either c_1 or c_2 (group 1), voxels in c_1 (group 2) and voxels in c_2 (group 3). In the first term, the sum of squared distances between each voxels timeseries and the average signal of all voxels in both clusters combined is calculated. In the second term the summations of squared distances for voxels in each cluster are calculated separately and added together. Then the first term is compared to the second term in form of a subtraction. This comparison shows if merging the clusters results in a smaller sum of squared distances than keeping them separate. So, for instance, if combining c_1 and c_2 is the better option then the result would be $\Delta(\mathrm{c}_1, \mathrm{c}_2) < 0$. This way the algorithm searches for clusters that are most optimal to combine.

To visualize the clustering HAC is often presented with a so called dendrogram. A dendrogram shows which clusters are being merged at each step and how far they are from each other

along the chosen metric. As mentioned above HAC does not require a predefined number of clusters. However, it is common practice to make the cutoff at the step that shows the largest distance of the chosen metric in the dendrogram (Khosla et al., 2019). In this work the amount of clusters was defined in advance, since the algorithm is used to parcellate the amygdala under the assumption that it is functionally divided into three subdivisions, as it is commonly suggested by cytoarchitectonic models, such as the Jülich Brain Atlas (Amunts et al., 2020).

2. Materials and Methods

2.1. Data

For analysis resting-state fMRI data of 123 participants was used. The sample consisted of 48 (26 female, mean age 27.9±8.1) healthy participants and 75 neurodivergent patients. The 75 patients were classified according to ICD-10 as F33.1 (9 female, 4 male, mean age 30.3±8.99), F33.2 (9 female, 7 male, mean age 27.6±8.6), F33.4 (20 female, 13 male, mean age 28.3±7.7), F40.1 (3 female, 2 male, mean age 34.6±9.4), F40.1 remitted (2 male, age 24 and 46), F41.0 (2 male, age 29 and 30), F41.1 (3 male, mean age 35.7±10) and F41.1 remitted (1 female, age 27). The data acquisition was part of a large-scale research project where measures were taken to ensure that the 48 healthy participants had no history of psychiatric or neurological diseases. Furthermore, they underwent urine testing to preclude substance use and, if required, pregnancy. Resting-state fMRI data was acquired with a MAGNETOM 7T whole-body MR scanner (Siemens Medical, Erlangen, Germany). The number of whole-brain volumes per scan was 258, collected with a 32-channel head coil (Nova Medical, USA). The used CMRR multiband EPI sequence collected the data with parameters T = 1.4 s, TE = 23 ms and flip angle = 62°). During resting-state scans participants were instructed to fixate a white cross and think about nothing.

2.2. Preprocessing

Preprocessing steps included slice time correction (FSL; Sladky et al., 2011), bias-field correction (ANTs, Avants et al., 2011), realignment (FSL) and normalisation to MNI space (ANTs), yielding volumes with 1.5x1.5x1.5mm³ voxel-size. To smooth the functional images a Gaussian Filter with a 3mm full-width half maximum (FWHM) parameter was applied (Nilearn).

2.3. Atlas

As an anatomical reference model, the Jülich Brain atlas was used for extracting brain signals in the area of the amygdala and for extracting brain signals of each subdivision in the amygdaloid complex. The atlas is based on 23 postmortem brains (11 female, mean age = 64 years, age range = 30-86 years), which were histologically analysed. The cytoarchitectonic maps are probabilistic representations of cortical areas and subcortical nuclei (Amunts et al., 2020). For the purpose of building a mask all subdivisions of the amygdala available in the atlas

were used. Besides the above mentioned laterobasal, centromedial and superficial group this also included the fibre masses (VTM, IF and MF). For statistical analysis only the first three subdivisions were included.

2.4. Simulation

One of the aims of this thesis is to shed light on the behaviour of unsupervised machine learning methods on fMRI data. As outlined above the described algorithms follow certain mathematical operations which determine how they would most likely react to a certain set of data. For fMRI analysis this data comes in form of timeseries, which each occupy a certain point in a three-dimensional space, resulting in a four-dimensional matrix (*volume x time*). Considering the properties of the data at hand and the detailed operations of the algorithm one could make inferences about their behaviour with a mathematical approach. But since this thesis investigates the issue from the perspective of cognitive psychology it will utilize a simulation where the behaviours of the clustering algorithm is tested under varying conditions. Using a simulation of fMRI data offers the comparison of the results to a ground truth. In this particular case it enables us to make assumptions about the functional parcellation of the amygdala and investigate how good the clustering algorithms are at detecting this parcellation. Especially interesting is how the clustering methods react to noise in the data, since the signal to noise ratio (SNR) is a prominent issue in fMRI analysis. A certain robustness to noise, would mean that these data-driven methods could as well be applied to datasets with smaller sample sizes. Another interesting aspect of entangling functionally similar voxels is how the algorithms perform in the transition areas between subregions.

The simulation was done in Python using the libraries *Numpy* and *SciPy*. Conceptionally it is a four-dimensional matrix that is filled with a signal-noise vector and three signal vectors, where each of the vectors are spatially weighted in different ways. The first three dimensions of the matrix, which represent space, were chosen to fit the size of the amygdala model. The fourth dimension models the timeseries and its length is the same as the timeseries in the real fMRI data. To model the noise, a vector in length of the fourth matrix dimension was created with *numpy.random.normal* and placed at every point in the three-dimensional space. This function draws random samples out of a Gaussian distribution with a predefined standard-deviation. This standard deviation parameter was used to stepwise increase the noise scale, to test how

the algorithms would perform under increasing signal distortion. The signal vectors, opposed to the noise vector, were created in a more informed way. Each vector consists of three different waves with a variety of different functions, which were added together to form the respective simulated signal. A criteria for these vectors was that they should be distinct from each other, which was measured by a correlation coefficient.

To create a model of the amygdala under the assumption that it is functionally divided in the three subregions of the Jülich Brain Atlas, the atlas was used to inform the spatial properties of the signals in the simulation. This was accomplished by using the probabilistic atlas regions as spatial weights. Each of the three regions (LB, CM and SF) was brought into the simulations coordinate space and separately multiplied with one of the three vectors. The probabilistic nature of the atlas had much in common with the properties of the fMRI BOLD signal. In fMRI data, the centre of an area of interest often shows the most activation towards its centre of mass and decays towards its periphery. A characteristic that is caused by the likewise probabilistic nature of statistical analysis of fMRI data, in regard to spatial information. The atlas was thresholded at the 25^{th} percentile mark, in contrary to the 50^{th} percentile for creating the mask, which is applied as a spatial constraint. This was done to obtain signals in the periphery that would fade out closer to the noise signal of the "empty" background voxels. This way the algorithm's ability of separating noise from actual signal could be tested better. The 25^{th} percentile mark was chosen over no threshold at all, because it was assumed that in application to real data some degree of spatial functional distinction is normally given.

The simulation was clustered by both described clustering-algorithms under two conditions, where one condition was run with the simulation as outlined above. In the second condition a mask with a 50^{th} percentile threshold was applied. This condition resembled the analysis of the real fMRI data more closely and was added to show the algorithms performance in a constrained space. In each condition several parameters were manipulated such as the noise scale and the *number of initialisations* for k-means clustering. The outcome of trials varying this parameter *number of initialisations* were used to inform the application of the k-means clustering parameter on the real fMRI data.

2.5. Statistical Analysis

The statistical analysis was done exclusively in Python, most prominently with the *Nilearn* library (https://nilearn.github.io/). A visual overview of the analysis workflow is provided in Figure 1. In the following sections the analysis steps will be described in detail.

2.5.1. Masking

As outlined above the amygdala mask used in this thesis was made with the probabilistic Jülich Brain Atlas. To get a homogenous binary mask that captures the amygdaloid area across subjects a few steps were performed. Firstly a threshold had to be defined to cut off voxel below a certain probability. As a probabilistic atlas is an estimation of the likelihood of each voxel being a part of the corresponding subdivision, voxels with a low likelihood have to be cut off to ensure that the mask does not overextend the area of interest too much. The amount of voxels with a sub 50% chance of being part of a subdivision is often higher than the amount of voxels above 50% likelihood. This occurs especially in small brain areas where the intersubject-variability in terms of anatomical location has a stronger effect. On the other hand, we want to make sure that we do not limit the atlas to a too high probability as this increases the chances that the mask does not capture enough of the area of interest. A good middle ground has to be found that is liberal enough to capture all of the amygdaloid complex in every subject with a high enough probability and at the same time does not overextend too far into brain tissue that is not part of the amygdaloid complex. Because of the arbitrary nature of this decision, previous literature that obtained satisfying results was used as an inspiration (Roy et al., 2009). This resulted in the use of a 50^{th} percentile value of the probabilistic atlas of each of its subdivisions. Additionally to using previous literature as orientation the resulting masks were qualitatively inspected.

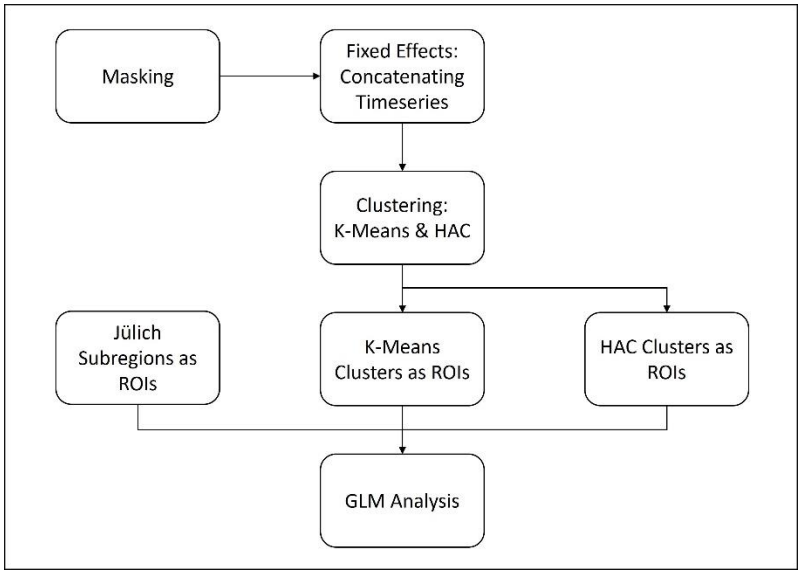

Figure 1 Analysis workflow overview depicting the single steps taken.

After choosing the cutoff strategy, the 50th percentile of voxel-values for each subdivision atlas (of areas LB, CM, SF, VTM, IF and MF) was calculated. Then the *nilearn.image.math_img* function was used to multiply each atlas image with a Boolean-Value-Matrix of itself, that only assigned a Boolean *True* value to the voxels above the 50th percentile threshold. This operation is possible in *nilearn.image.math_img*, because it treats the image as a data matrix. This way simple calculations like the one explained above can be carried out. After obtaining the thresholded atlas regions, smoothing was applied in the same manner as outlined above, to get a homogenous chunk of data, since the mask contained holes in form of missing voxels. Lastly the images were simply added together and binarized with the function *nilearn.image.binarize_img*. Masks for both hemispheres were obtained in this fashion. The masks were then utilized by the *nilearn.maskers.NiftiMasker* to extract a timeseries for each probably-amygdala voxel in the mask.

2.5.2. Fixed Effects Analysis

To prepare the data for clustering, a fixed effects approach was chosen. In a fixed effects model all subject timeseries are treated as one continuous timeseries by simply concatenating them. A mixed-effects model, where the between-subject variability is compared, would be a more powerful way of analysing the data (Chen et al., 2013), because it is more robust against strong effects in a subset of subjects and therefore not as easily biased as the fixed effects model, where the effect of one statistical outlier can have a high influence on the analysis. A fixed

effects approach on the other hand is generally more sensitive. In a fixed effects model each subject makes the same contribution to the activation timeseries without considering random variations from subject to subject. Treating the activation as common to all subjects can reflect aspects of functional anatomy that may be representative of the examined group (Friston et al., 1999). The disadvantage of increased sensitivity is that the inferences made are hard to generalize to other populations except the one where the sample was drawn from. Another problem would be that a fixed effects analysis is unfavourable when comparing different groups of subjects (Friston et al., 1999). But considering these characteristics it can be said that it still remains a suitable approach for cluster analysis, because high sensitivity in regard to effects reflecting functional anatomy is highly desirable for this purpose. Furthermore, the limitation of being able to describe only one group of subjects does not affect the inferences made in this thesis, because no between-group comparisons are made based on the fixed effects model. These characteristics also align with the overall intentions of this thesis of investigating methods to obtain parcellations that fit the data at hand better than general anatomical models.

Another reason for using a fixed effects approach was of a more practical nature. Difficulties arose due to certain characteristics of the clustering algorithms. As outlined above the k-means algorithm randomly places its centroids in the data space. This has the advantage of reducing bias, but comes with the disadvantage that every time the algorithm is run over a set of data, the labels of clusters, which would theoretically occupy the same space across subjects, for the most part carry different values. So if the algorithm would parcellate every single subject, acquiring a mean clustering on a group level was not possible without relabelling the obtained single clusters. A possible solution for this would have been to apply a similarity metric like the Dice-Coefficient (Dice, 1945) and compare which clusters were the most similar. However, the implementation of such an algorithm was not deemed a reasonable decision in the face of the moderate added value gained by a mixed-effects model, compared to the significant time-costs related to the successful accomplishment of the task. The deterministic nature of the hierarchical clustering algorithm would not have caused the problem of alternating labels across subjects, but would have needed further arbitrary decisions. These decisions would have also applied to the k-means algorithm and concerned the threshold at which value a voxel would have been assigned to a certain cluster after group level averaging.

Furthermore, the fixed effects model was only used for running both clustering algorithms. For the final analysis steps, where the comparison of between-subject effects was of higher importance, a different approach was chosen. So considering that this thesis additionally aimed to test an efficient implementation of unsupervised machine learning to individual data, the trade-off made with the fixed effects approach was considered a valid decision.

2.5.3. Clustering

The implementation of the k-means and hierarchical clustering algorithms was, as mentioned above, done in the Python library scikit-learn with the functions *sklearn.cluster.KMeans* and *sklearn.cluster.AgglomerativeClustering* respectively. Both functions are object-based, which means that the properties of each algorithm are defined beforehand in a so called "object". This object is then fitted to the data and gets callable attributes which resemble the results of the calculation. For HAC the only property that had to be defined was the number of clusters that had to be found. For k-means clustering additionally a parameter that dictated the number of times that the algorithm is run with different centroid seeds (number of initializations) had to be passed. The simulation was used to observe the impact of changing this parameter by comparing different variations. These tests indicated an increase in performance when initializing the algorithm 50 times instead of scikit-learns default configuration (number of initializations = 1). This increase of performance was predicted especially for the application at hand, namely masked timeseries data (see Results). The maximum iterations of the k-means algorithm were limited to 300 for a single run, which corresponds to scikit-learns default parameter. Both functions were then applied to the transposed concatenated timeseries of the masked images.

Turning the format of the resulting clusters back into a *NifTI* file format required the help of *Nilearn* functions, since the *scikit-learn* library is not made for fMRI analysis and is not equipped with straightforward solutions. Both clustering functions returned a one dimensional list of the corresponding labels of each voxel, where the label value represented the cluster they were assigned to. The labels had the same index as the voxels in the feature matrix. This way the spatial information was still present in the one dimensional array. To return the list from one dimension into three-dimensional space the *nilearn.maskers.NiftiMasker* was utilized to fit the amygdala mask to the labels. First the labels had to be extended along the

second dimension, in length of the amount of timepoints in the signal timeseries, to replicate timeseries data. This way the amygdala mask could be fit to the “labels-matrix” and transform it into a 3-dimensional NIfTI-image that represented the clusters in the standard coordinate space for fMRI-analysis. This resulting image represents the derived parcellated amygdala for each clustering algorithm and was further used as a map of regions of interest (ROIs) for further analysis.

2.5.4. General Linear Model (GLM)

For obtaining whole brain connectivity maps a General Linear Model was used for each set of subdivisions (Jülich Atlas, k-means clustering, HAC) respectively. The acquisition of the clustering-based subdivision was outlined above. For the subdivisions of the Jülich Brain Atlas the 50^{th} percentile thresholded probabilistic maps from previous steps were used. Additionally, minor overlaps between the subregions were removed, so every voxel was assigned to only one of the three subdivisions. Every parcellation image contained three subdivisions with a set of voxels that were assigned a value from 1 to 3. Nilearn’s *nilearn.maskers.NiftiLabelsMasker* was used to extract the mean timeseries of every subject for every region of interest (ROI) for every of the three methods described above.

For first level GLM analysis the nilearn function *nilearn.glm.first_level* was used. As with the clustering procedure, a first level model object was defined and then fit to the data together with the design matrix of every subject. The design matrix contained every extracted mean timeseries for every ROI, which served as regressors in the GLM. This procedure was done for all three parcellations respectively.

The second level GLM analysis was done in a similar fashion using the function *nilearn.glm.second_level*. The second level analysis contrasts always directly compared each of the three ROIs against the other two, using a paired t-test (e.g. *ROI1* vs *ROI2* & *ROI3*). This direct comparison yielded associations significantly higher in one ROI than in either one of the other two ROIs.

3. Results

3.1. Simulation

3.1.1. K-Means

3.1.1.1. Number of Initializations = 1

Unmasked. The clustering of the unmasked simulation with only one initialization of cluster centroids showed that the k-means algorithm could easily differentiate the ground truth clusters, when no noise was present. After gradually increasing the noise scale the resulting clusters began to decay continually. At a noise-scale of three standard deviations the clustering algorithm could not clearly differentiate the no-signal voxels from signal voxels (Fig. 3). This could be related to the signal strength of voxels lying within the yellow cluster. When the strength of the noise signal reaches a strength similar to the signal strength of the “amygdala signal” then the detection of voxels in the cluster becomes increasingly random.

Masked. Applying a mask to the data as it is standard practice in fMRI analysis, counterintuitively did not improve the clustering results. Looking at (Fig. 4) it can be observed that with an increase of the noise scale, the quality of the results drastically decreases. At a scale of 0.5 standard deviations one of the true clusters disappears and instead the region which appears to be the transition area between the two other true clusters gets detected as its own distinct group. Increasing the noise scale further leads to the formation of nested clusters, suggesting that the algorithm is detecting different signal intensities of the same signal as different regions. At 2.5 standard deviations the algorithm fails to detect more than one cluster of the ground truth. The results of this trial were somewhat unexpected as the mask was thought to improve the quality of resulting subregions, because the data signals are spatially constrained. Due to the similar principle of approach in real fMRI data this raised concern that the results of clustering masked data could be impaired. A possible solution for improving the cluster quality was increasing the *number of initializations* parameter.

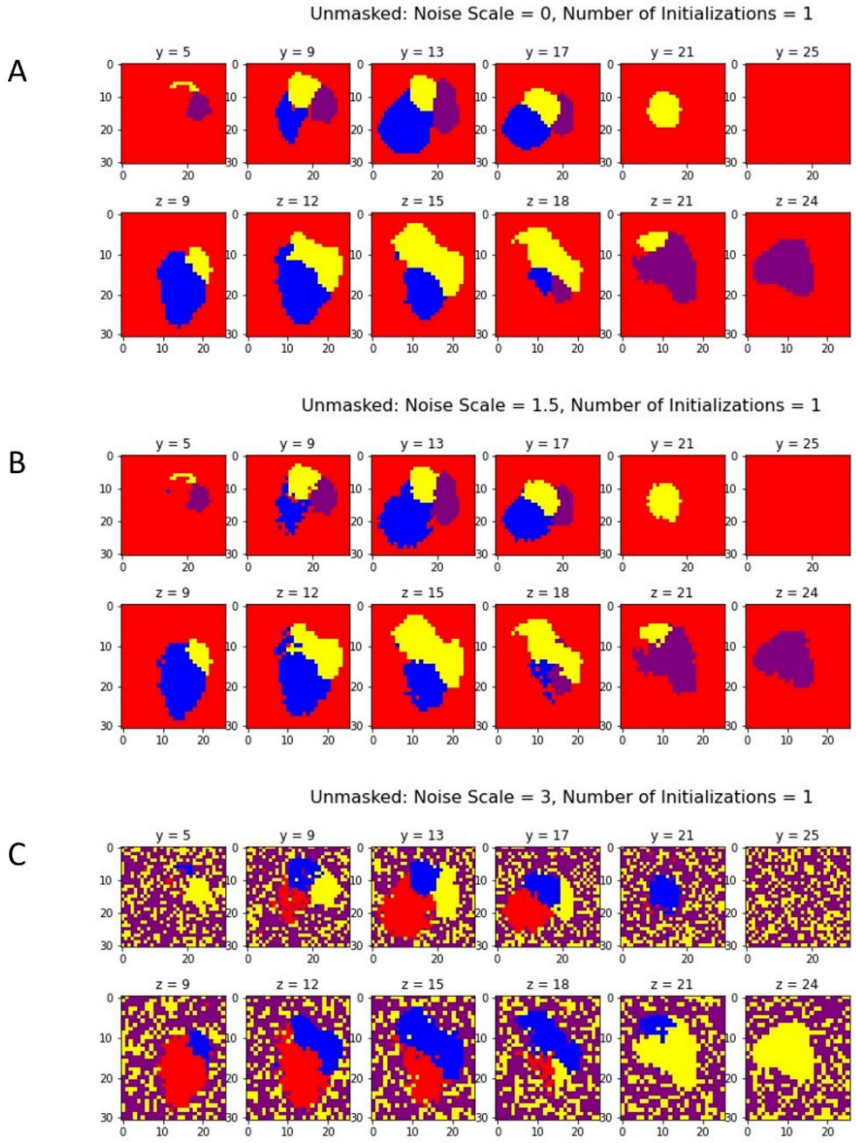

Figure 2 Clustering obtained from applying k-means to unmasked data with number of initialisations = 1. Note that colours of each cluster can change from plot to plot due to random labelling.

3.1.1.2. Number of Initializations = 50

Masked. Increasing the number of initializations to 50 helped to stabilize the clustering and improved the results significantly, compared to the previous trial. Clusters were stable up until the noise scale reached two standard deviations. After passing that point the results showed similar patterns as before when only one initialization was performed. The cluster representing SF disappeared and in its stead the algorithm identified a transition area as an independent region. At the point of three standard deviations noise the algorithm was not able anymore to detect more than one cluster.

These findings strongly suggest to increase the number of initialization for application of the algorithm on real fMRI data due to the comparable properties. It is hard to find an explanation for the observed behaviour, since spatially constraining the data was expected to improve clustering performance. However, a detailed analysis of the algorithm's behaviour is not the aim of this thesis and the mere observation of the behaviour suffices to inform the algorithms parameters in further analysis.

3.1.2. HAC

Unmasked. The performance of hierarchical clustering of the unmasked simulation was similar to the performance of k-means clustering. With no noise at all the algorithm had no problems identifying the underlying subregions. With increasing noise, the identified clusters decayed continually, but in different ways as in the runs with k-means. On the one hand HAC was better at detecting the background noise as one coherent voxel-group, but on the other hand the detected subregions were absorbed quicker (at a lower noise scale) than with k-means clustering.

Masked. Masking increased the performance of the hierarchical clustering algorithm drastically. Compared to the unmasked conditions clustered with k-means, HAC had little problems in detecting the three subregions even in high noise conditions. The subregions decayed marginally, but retained most of their voxels in a coherent cluster.

A

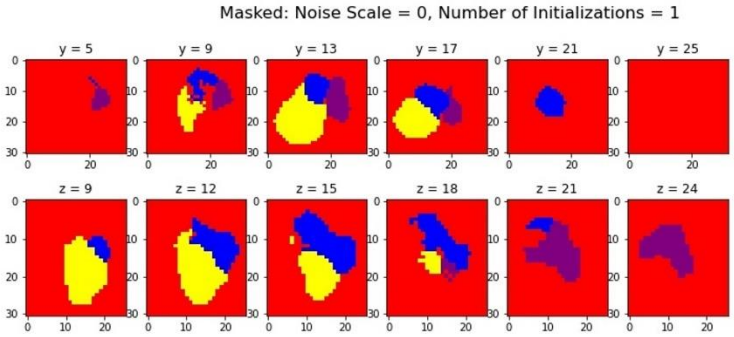

B

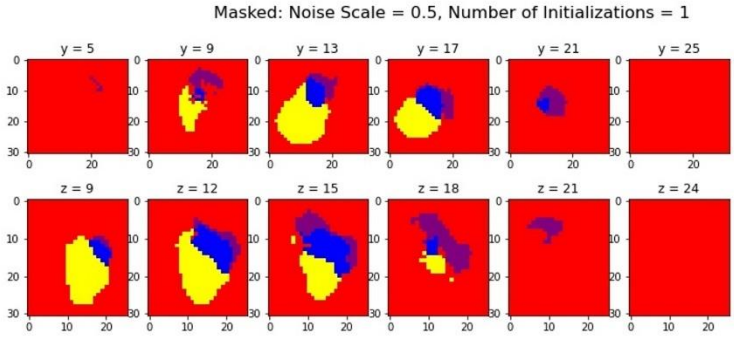

C

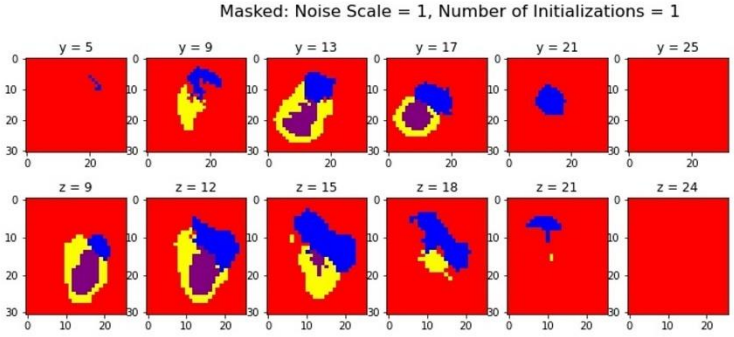

D

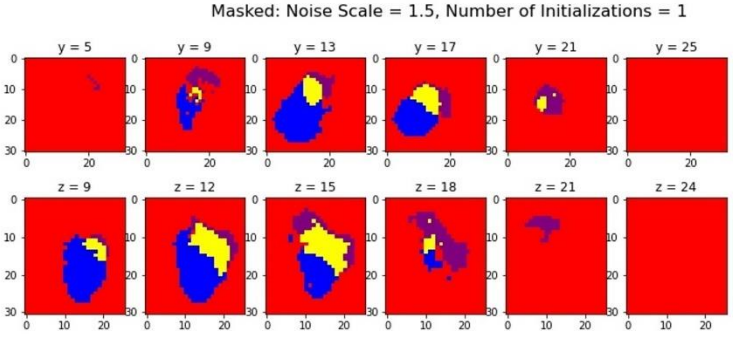

Figure 3 Clustering obtained from applying k-means to masked data with number of initialisations = 1. Note that colours of each cluster can change from plot to plot due to random labelling.

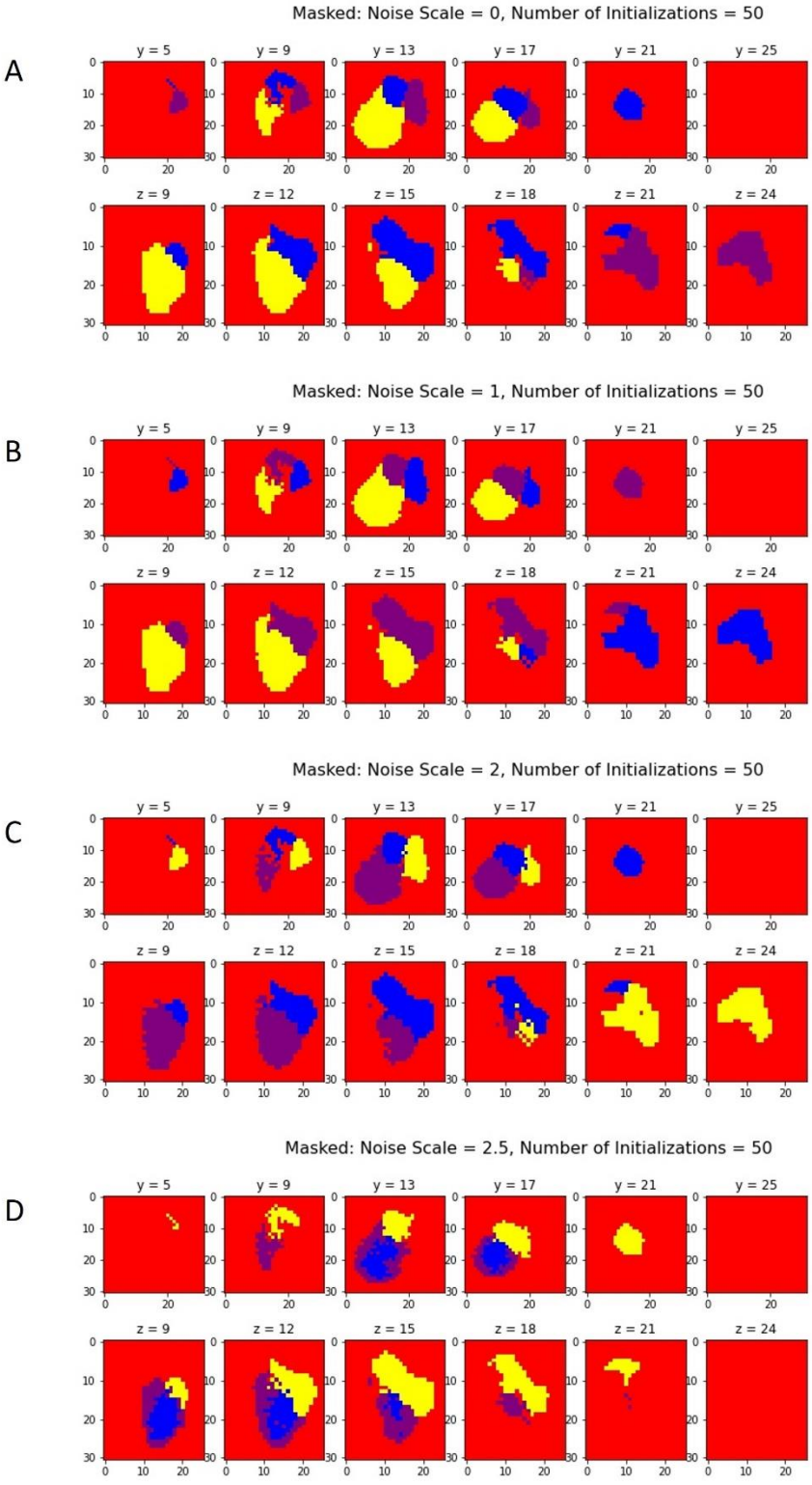

Figure 4 Clustering obtained from applying k-means to masked data with number of initialisations = 50. Note that colours of each cluster can change from plot to plot due to random labelling.

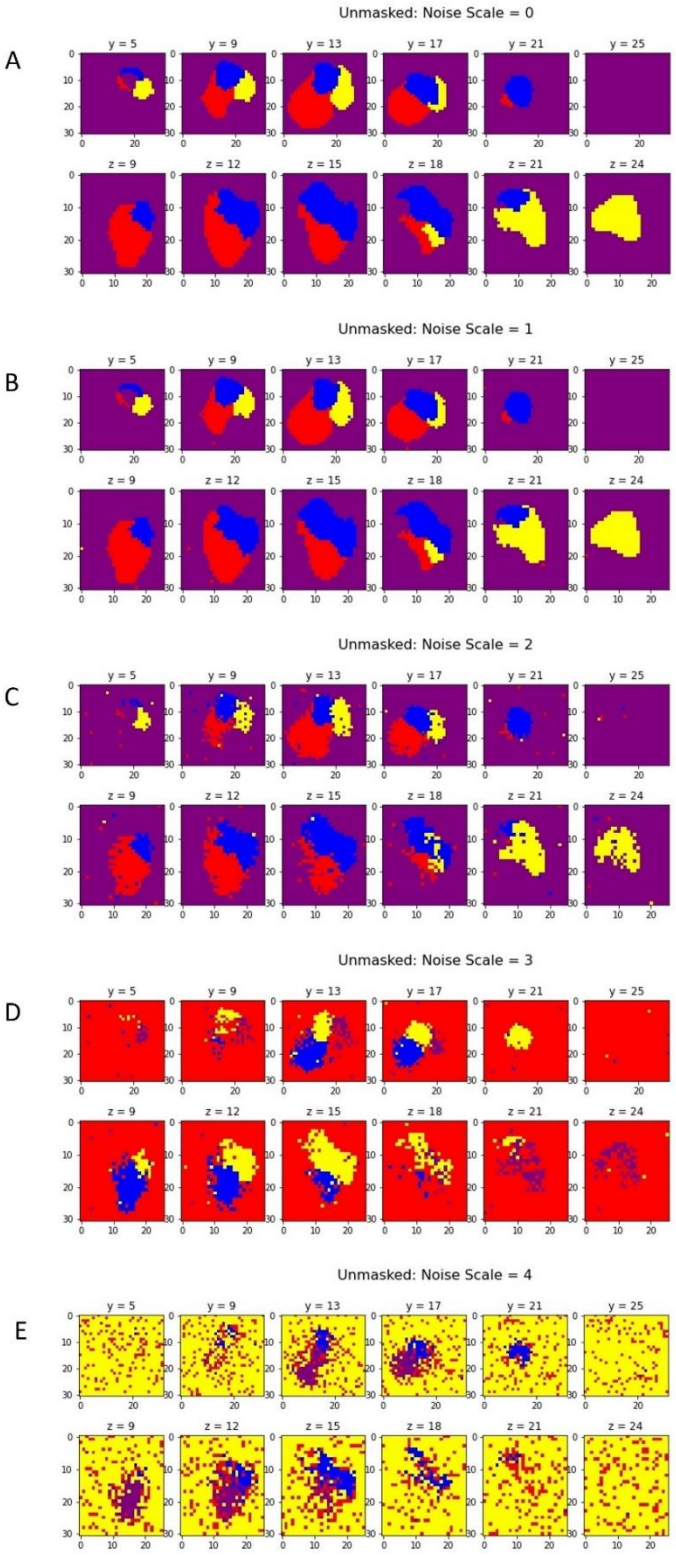

Figure 5 Clustering obtained from applying HAC to unmasked data. Note that colours of each cluster can change from plot to plot due to random labelling.

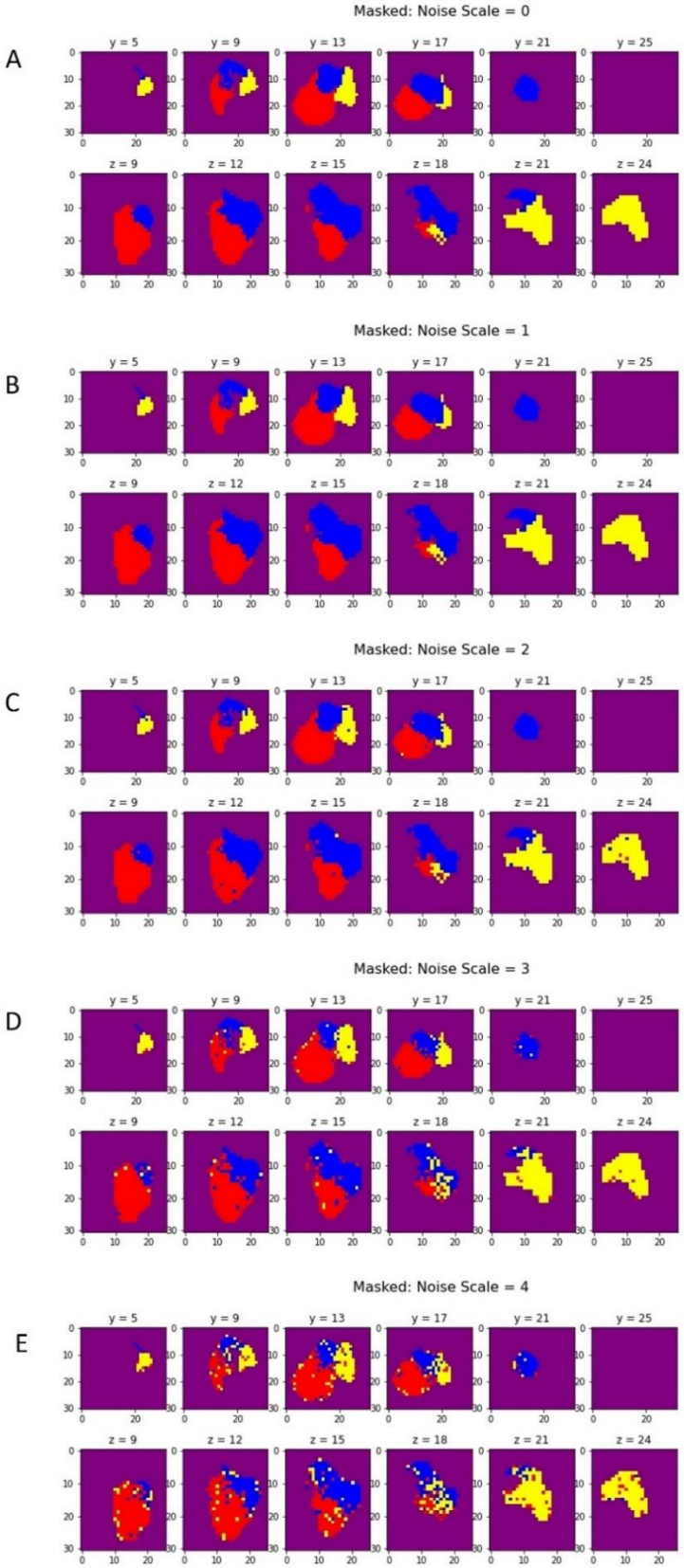

Figure 6 Clustering obtained from applying HAC to masked data. Note that colours of each cluster can change from plot to plot due to random labelling.

3.2. Clustering

The resulting clusters obtained by both k-means clustering and HAC are similar in location to the ones delineated by the Jülich brain atlas but show some notable differences in their size (see Fig. 7). K-means parcellation (Fig. 7A) yielded respective cluster-sizes for left and right hemisphere LB of 2311.5mm³ (39.3%) and 2535mm³ (39.9%), for left and right CM of 1336.5mm³ (22.7%) and 1411.5mm³ (22.2%) and for the two SF clusters, 2233.5mm³ (38.0%) and 2410.5mm³ (37.9%). HAC parcellation (Fig. 7B) resulted in respective cluster-sizes for left and right LB in 2224.5mm³ (37.8%) and 2602.5mm³ (40.9%), for CM in 732mm³ (12.4%) and 564mm³ (8.9%) and for SF in 2925mm³ (49.7%) and 3190.5mm³ (50.2%). In comparison the reference regions of the Jülich Brain Atlas (Fig. 7C) which underwent cut-off at their 50th percentile show larger LB (left: 2466mm³, 47.9%; right: 2563mm³, 47.5%) and CM (left: 1207.5mm³, 23.4%; right: 1303.5mm³, 24.2%). The biggest difference can be seen in SF regions as they are substantially smaller than the clustering derived counterparts with 1477.5mm³ (28.7%) and 1528.5mm³ (28.3%) for left and right hemisphere respectively. In the k-means and HAC conditions parts of the CM have been “swallowed” by SF. However, overall these findings yield satisfactory results and are subjected to validation through connectivity analysis in further sections.

3.3. Connectivity Analysis

The results yielded by brain connectivity analysis will be shown below in three stages. Starting off with so called *glass-brain* plots of the connectivity maps, allowing a brief presentation of the signal distribution across the brain followed by a more detailed comparison of connectivity maps and detailed analysis of signal peaks in the connectivity maps.

3.3.1. Glass-Brain Overview

Laterobasal. The direct comparison results for the laterobasal subdivision yielded similar distributions for positive and negative signal-associations in all three conditions for both hemispheres. Overall the visualizations for each condition indicate positive associations in parietal and frontal regions, as well as negative associations in occipital regions across all three conditions. For the laterobasal subdivision the glass-brain plots suggest similar connectivity across all conditions for both hemispheres.

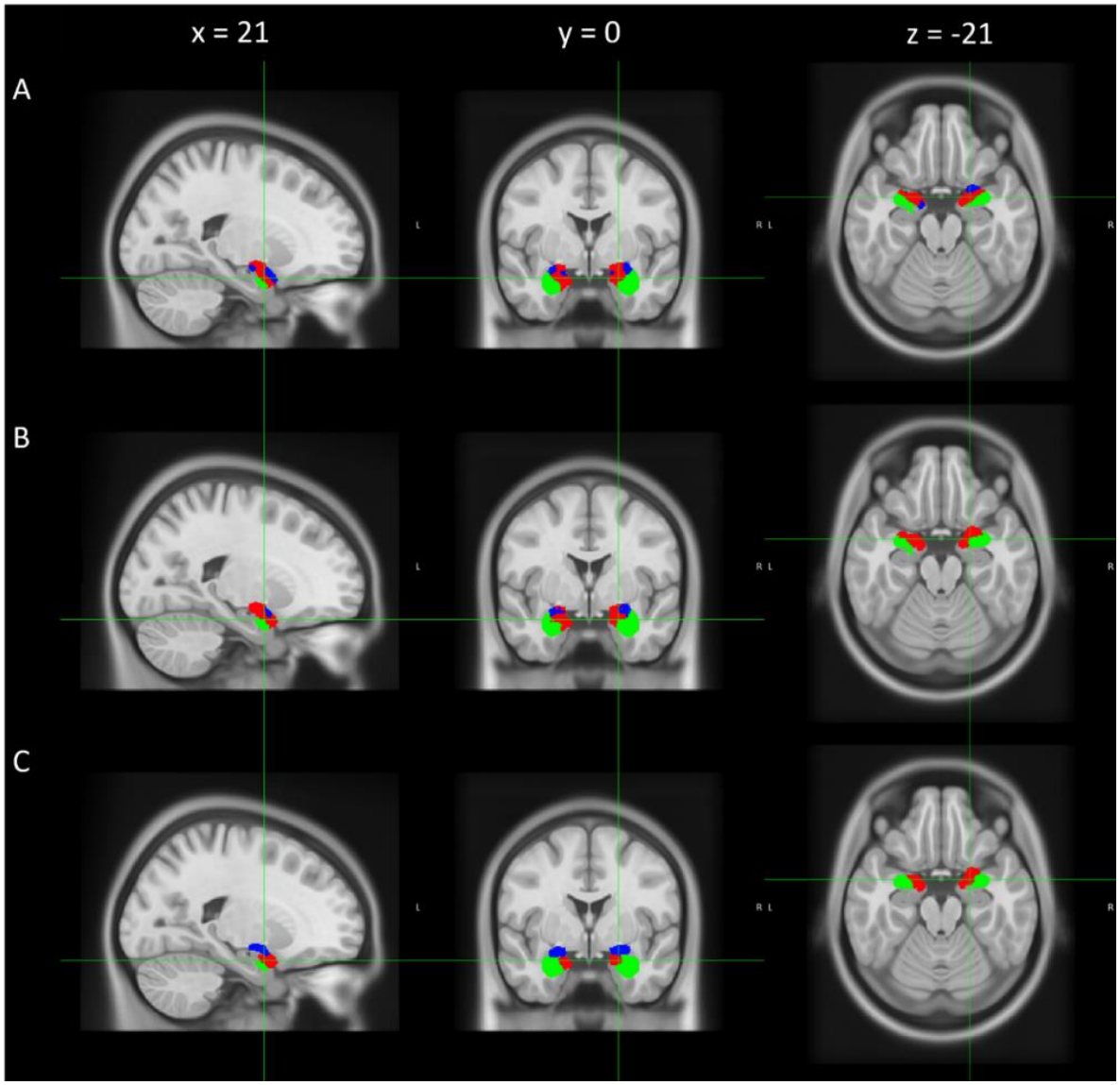

Figure 7 Clustered amygdala obtained by k-means (A), HAC (B) and the Jülich atlas (C). The regions most likely represent LB (green), CM (blue) and SF (red) in all three conditions. Regions have been printed on MNI-Space template.

Centromedial. A more diverse distribution can be seen in the glass-brain plots for the centromedial subdivision, as the signal association map for the k-means condition in the left hemisphere shows negative signal association in latero-occipital regions in contrast to all other maps. By and large, all maps indicate positive associations in areas of the limbic lobe, medio-occipital areas and marginally in the medial frontal lobe. The most significant difference of the k-means derived map of the left hemisphere is, that it suggests a much more distinct connectivity map in limbic regions, compared to the other conditions. This can also be seen in the visualization of the right hemisphere, although to a lesser degree.

Superficial. Another interesting finding was made comparing the association maps of the superficial subdivision. As can be seen in Fig. 10, maps across both k-means and HAC

conditions in both hemispheres indicate resemblance across all areas, including positive associations in the frontal and parietal lobe, negative associations in the occipital lobe and a highly distinct connectivity network in the limbic regions. In contrast, the maps derived from the Jülich atlas show global negative signal associations in the left hemisphere and almost global negative association in the right hemisphere. There are some indications of more diverse signal distributions in the limbic regions. However, these show little more than positive auto-associations.

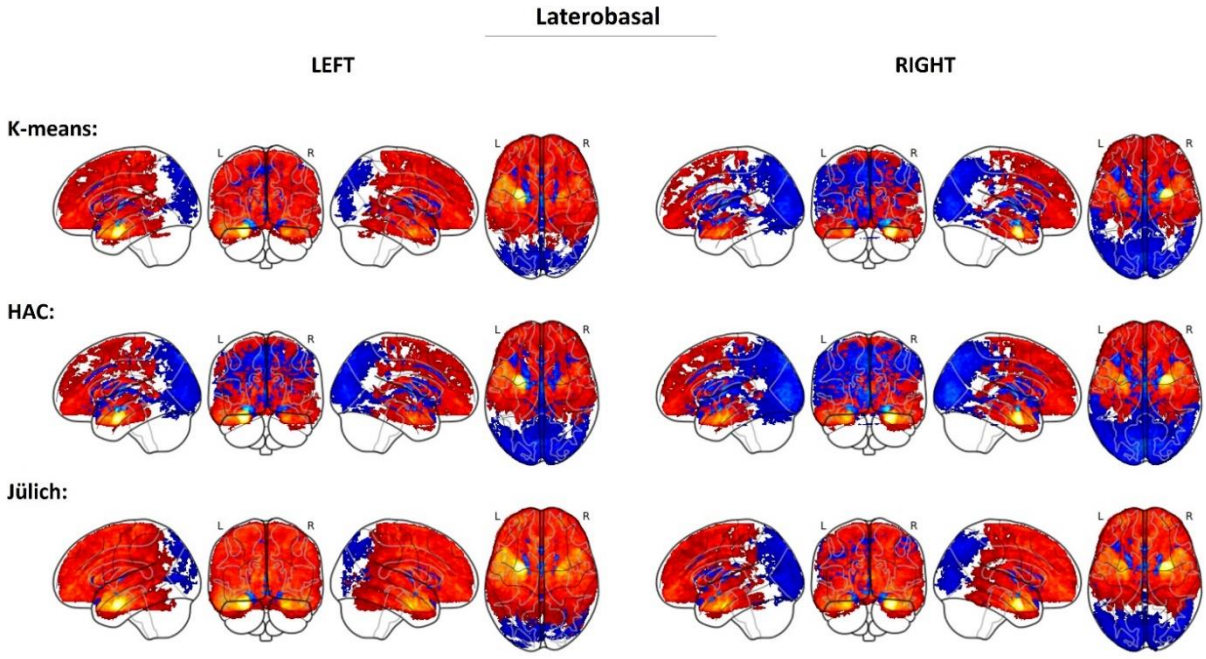

Figure 8 Obtained connectivity maps of the laterobasal amygdala for all three conditions and both hemispheres. Maps were corrected voxel-wise ($p<0.001$) and plotted in glass brains, depicting all voxels at once.

By examining these glass-brain visualizations it can be seen that the association maps derived from each clustering method are comparable across each other and both hemispheres. What stands out though, is the indication, that in maps derived from k-means and HAC more detailed and nuanced networks are present in the limbic regions. The next section will take a closer look at the signal association maps.

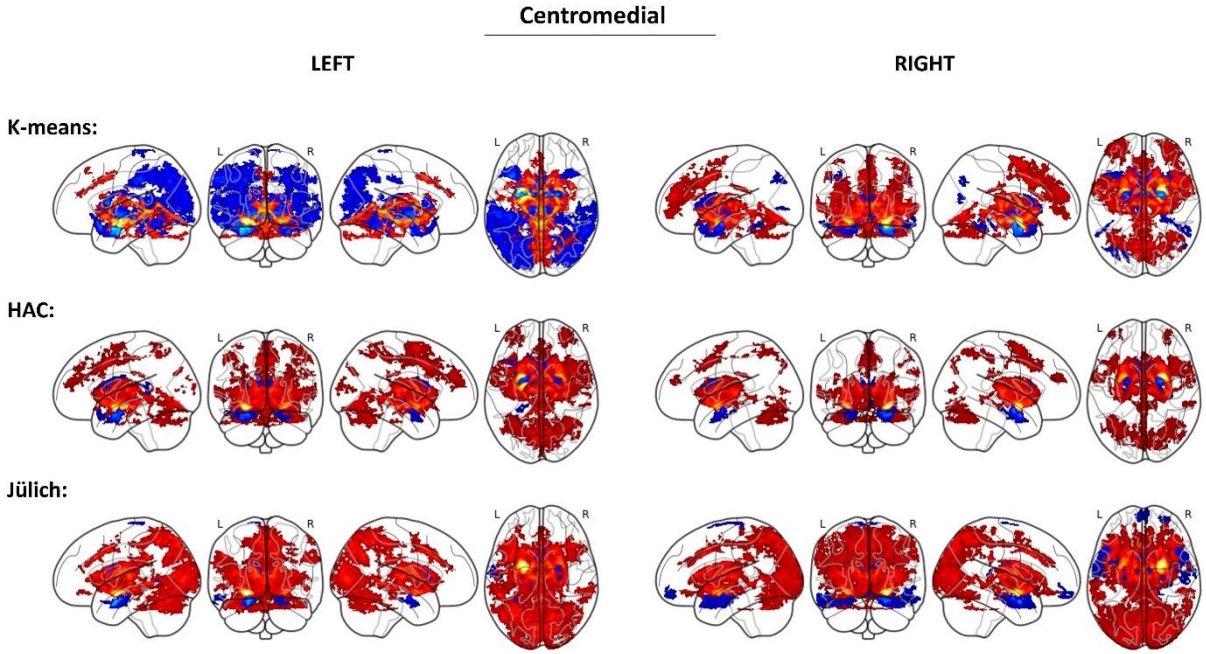

Figure 9 Obtained connectivity maps of the centromedial amygdala for all three conditions and both hemispheres. Maps were corrected voxel-wise (p<0.001) and plotted in glass brains, depicting all voxels at once.

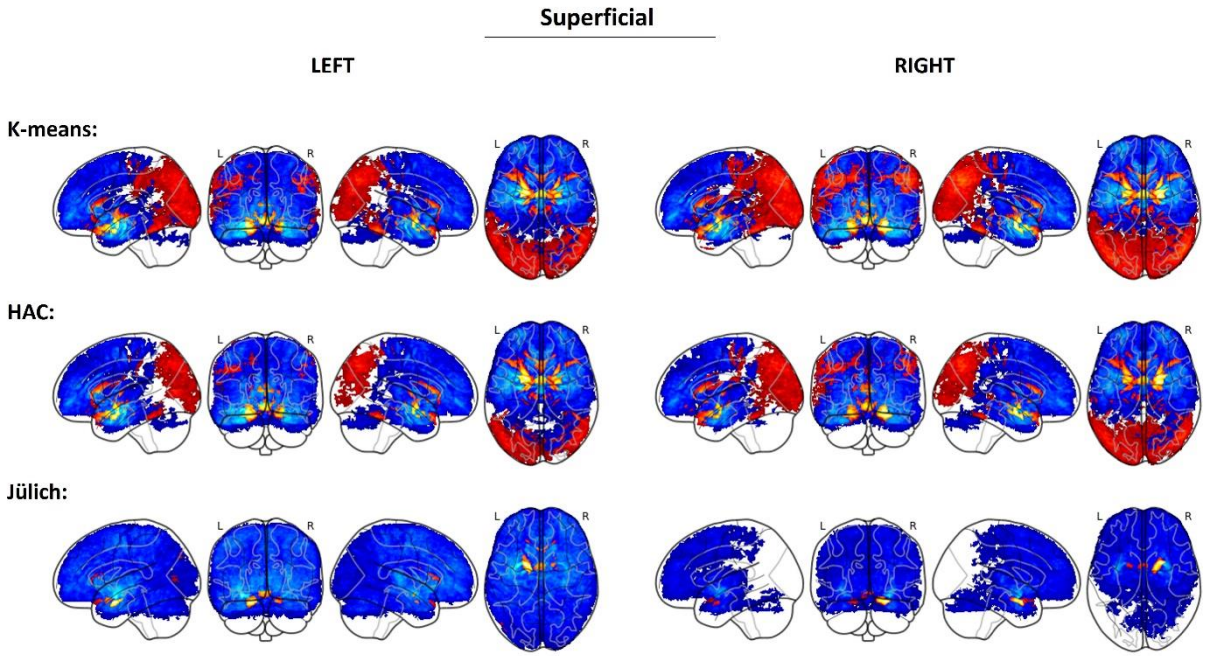

Figure 10 Obtained connectivity maps of the superficial amygdala for all three conditions and both hemispheres. Maps were corrected voxel-wise (p<0.001) and plotted in glass brains, depicting all voxels at once.

3.3.2. Connectivity Comparison

Laterobasal. In Fig. 11 the connectivity maps derived from direct comparison *LB vs. CM+SF* are depicted for the left hemisphere. For all three conditions (k-means, HAC and Jülich) positive connectivity extends from the seed region posterior into hippocampal regions, as well as lateral into superior and middle temporal gyrus (Fig. 11A: x=-30, B: y=0). Other positive

activation in all three regions can be observed in frontal lobe, ventromedial prefrontal cortex, tegmental area, anterior cingular and cingular cortex.

Negative connectivity in all three conditions is evident bilaterally in centromedial amygdala and hypothalamus. Furthermore, negative association can be found in occipital areas in all three conditions, but in strongly varying degrees of cluster size, with k-means and Jülich conditions having substantially smaller clusters than the HAC derived connectivity maps.

Overall the connectivity maps for LB of the left hemisphere show a very similar distribution of positive and negative signal clusters. However, what stands out looking at Fig. 11, is that connectivity maps derived from the Jülich Atlas yield overall bigger clusters with positive association.

Connectivity maps of right hemisphere LB (LBr, Fig. 12) show positive and negative signal associations largely in the same locations as do connectivity maps of left hemisphere LB (LBl), although, the cluster sizes for positive associations appear to be smaller in LBr than in LBl. Although less prominent, positive association is still present in LBr frontal and temporal regions as well as posterior and anterior cingulate cortex. Furthermore, there is no significant positive association in LBr ventral tegmental area. Regarding negative association, LBr shows bigger clusters in occipital areas across all three conditions, with k-means and Jülich differing the most from LBl. Negative connectivity in CM, hypothalamus and thalamus stays the same. Two differences to LBl are that in LBr we can see negative anterior insula connectivity (Fig. 12B: y=10-30, Fig. 12C: z=10) and left somatosensory cortex (Fig. 12C: z=20), especially in k-means and HAC conditions.

Centromedial. When we look at connectivity maps of left hemisphere CM (Fig. 13), the first thing one might see is the positive association along the stria terminalis across all three conditions that extends from CM, however, not to the same degree. For the k-means CM map striatal activity is visible in Fig. 13C: z=-10, but not in Fig. 13A: x=-30, Fig. 13B: y=0. For HAC and Jülich derived maps striatal activity is visible in all of the above plots. Further similarities between HAC and Jülich which are not present in k-means is positive connectivity in anterior insula and putamen (Fig. 13C: z=10), as well as in lateral regions of the thalamus. In contrast to the big clusters in lateral thalamus of HAC and Jülich, lateral thalamus in k-means shows smaller clusters with higher connectivity and additional negative associations (Fig. 13A, x=10,

x=-10). Positive connectivity in posterior thalamus (Fig. 13C, z=0) and anterior cingulate cortex (Fig. 13A, x=0) is present in all three conditions ,as well as in regions of the cerebellum, however more so in HAC and Jülich connectivity maps (Fig. 13A, x=-30, x=30; Fig. 13C, z=-30). All three conditions show negative signal associations with areas adjacent to CM, suspected to be the superficial region of the amygdala. In k-means and HAC conditions this negative connectivity extends to the hypothalamus. Negative connectivity in the visual cortex is only present in k-means derived connectivity maps.

The connectivity maps of derived CM for the right hemisphere (CMr, Fig. 14) are again similar to left hemisphere maps, but with potentially relevant differences. All differences remain the same except for following changes in CMr k-means derived maps: there is no more negative association in visual cortex, it is now the only condition where negative connectivity in the hypothalamus is visible and there is now positive connectivity in the putamen and marginally in the anterior insula.

Superficial. In connectivity maps derived from left hemisphere superficial amygdala (Fig. 15) there is clear positive signal association in bilateral superficial amygdala and hypothalamus across all conditions (Fig. 15B, y=0). The connectivity cluster extends bilateral from SF and hypothalamus to striatal regions in all conditions, but less so in Jülich derived maps (Fig. 15B, y=20). Other clusters of positive connectivity can be found in visual cortex of k-means and HAC derived maps (Fig. 15A, x= -30) and in regions medial of the caudate nucleus in the anterior callosum and nucleus accumbens across all conditions (Fig. 15B, y=20).

Negative signal association is much more present in the SF derived connectivity maps than from the other regions reported above. For the Jülich condition we have negative connectivity covering large portions of cortex which makes it hard to pinpoint regions (see Fig. 15 and 16). Regions that show negative bilateral connectivity across all conditions are the laterobasal amygdala extending into the temporal lobe (Fig. 15B, y=0). This cluster is more detailed in k-means and HAC conditions as can be seen in Fig. 15A (x=-30) and extends partially into hippocampus. Another structure that shows clear negative connectivity across all three conditions is the caudate nucleus (Fig. 15B, y=20, z=0), frontal lobe and ventromedial prefrontal cortex and ventral tegmental area (Fig. 15C, z=-20). In connectivity maps of SF the same regions are associated positively and negatively for both hemispheres, other than functional connectivity of LB and CM.

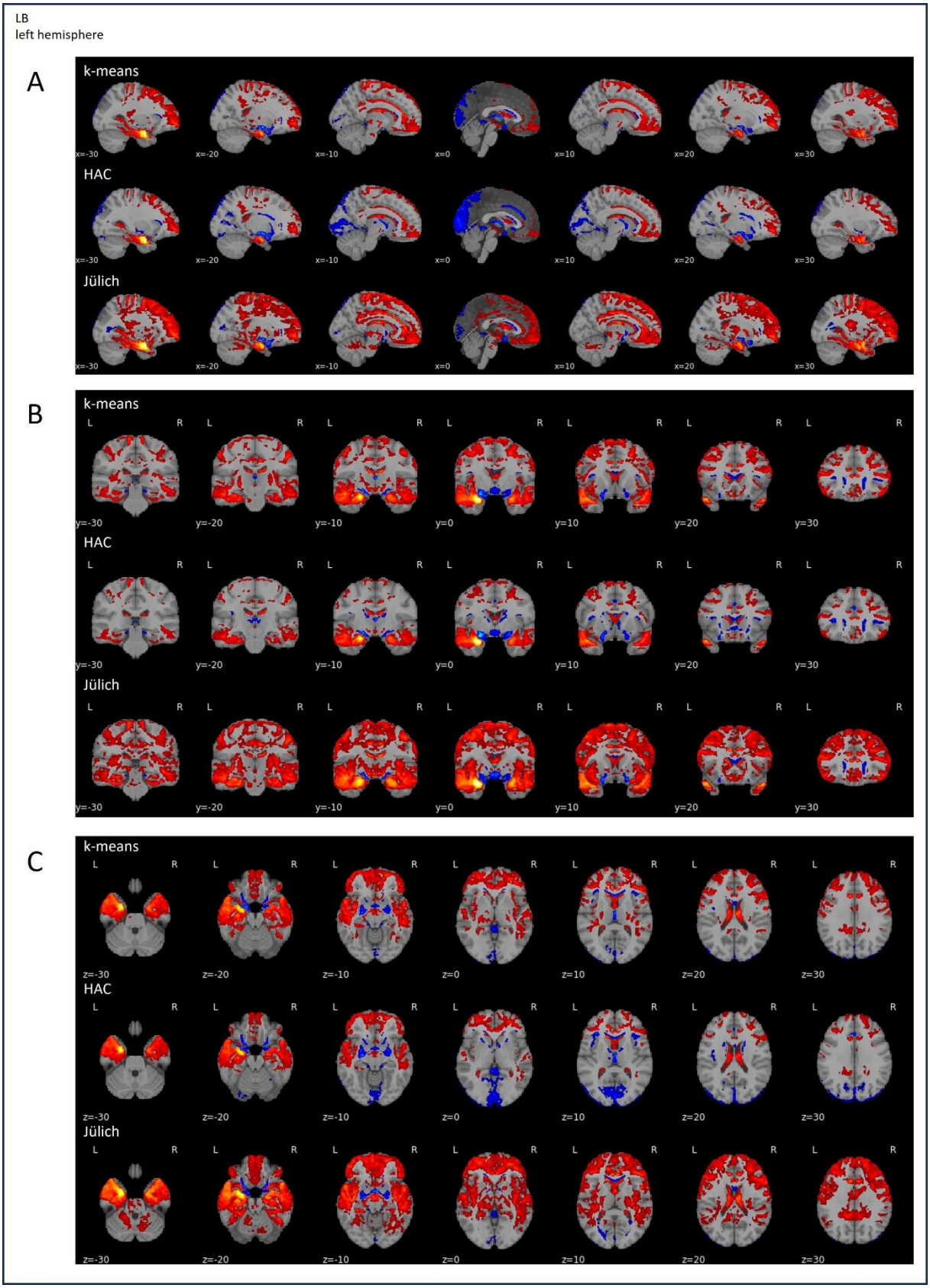

Figure 11 Direct comparison of left hemisphere functional connectivity LB vs. CM+SF. Red areas indicate a significant positive prediction of fMRI signal and blue areas indicate significant negative predictions. Brighter colours indicate stronger signal association. A voxel-wise threshold ($p \leq 0.001$) and cluster size threshold (min. 1000 voxel) have been applied. The maps are displayed sagittal (A), coronal (B) and axial (C) for k-means, HAC and Jülich derived maps.

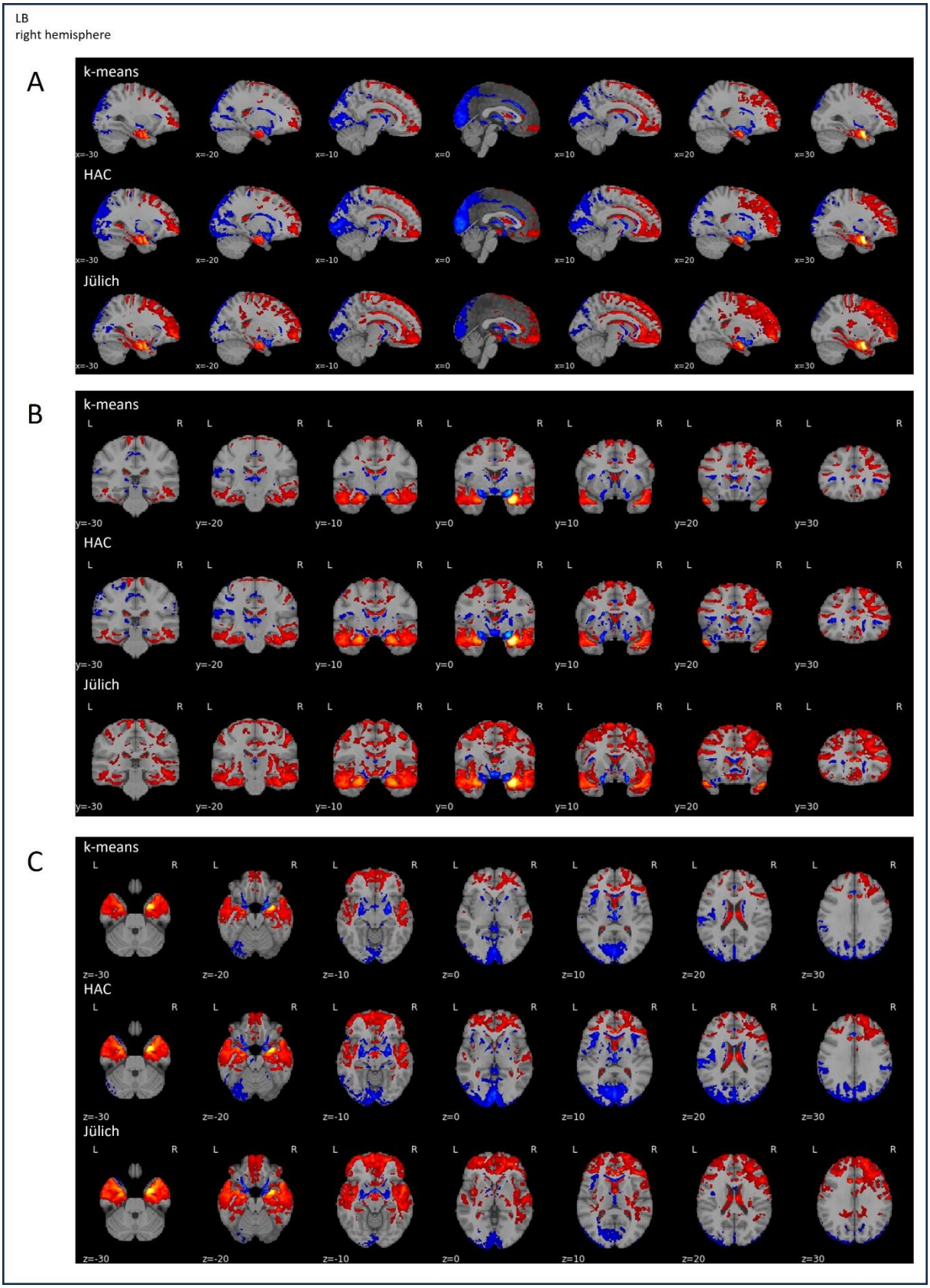

Figure 12 Direct comparison of right hemisphere functional connectivity of LB vs. CM+SF. Red areas indicate a significant positive prediction of fMRI signal and blue areas indicate significant negative predictions. Brighter colours indicate stronger signal association. A voxel-wise threshold ($p \leq 0.001$) and cluster size threshold (min. 1000 voxel) have been applied. The maps are displayed sagittal (A), coronal (B) and axial (C) for k-means, HAC and Jülich derived maps.

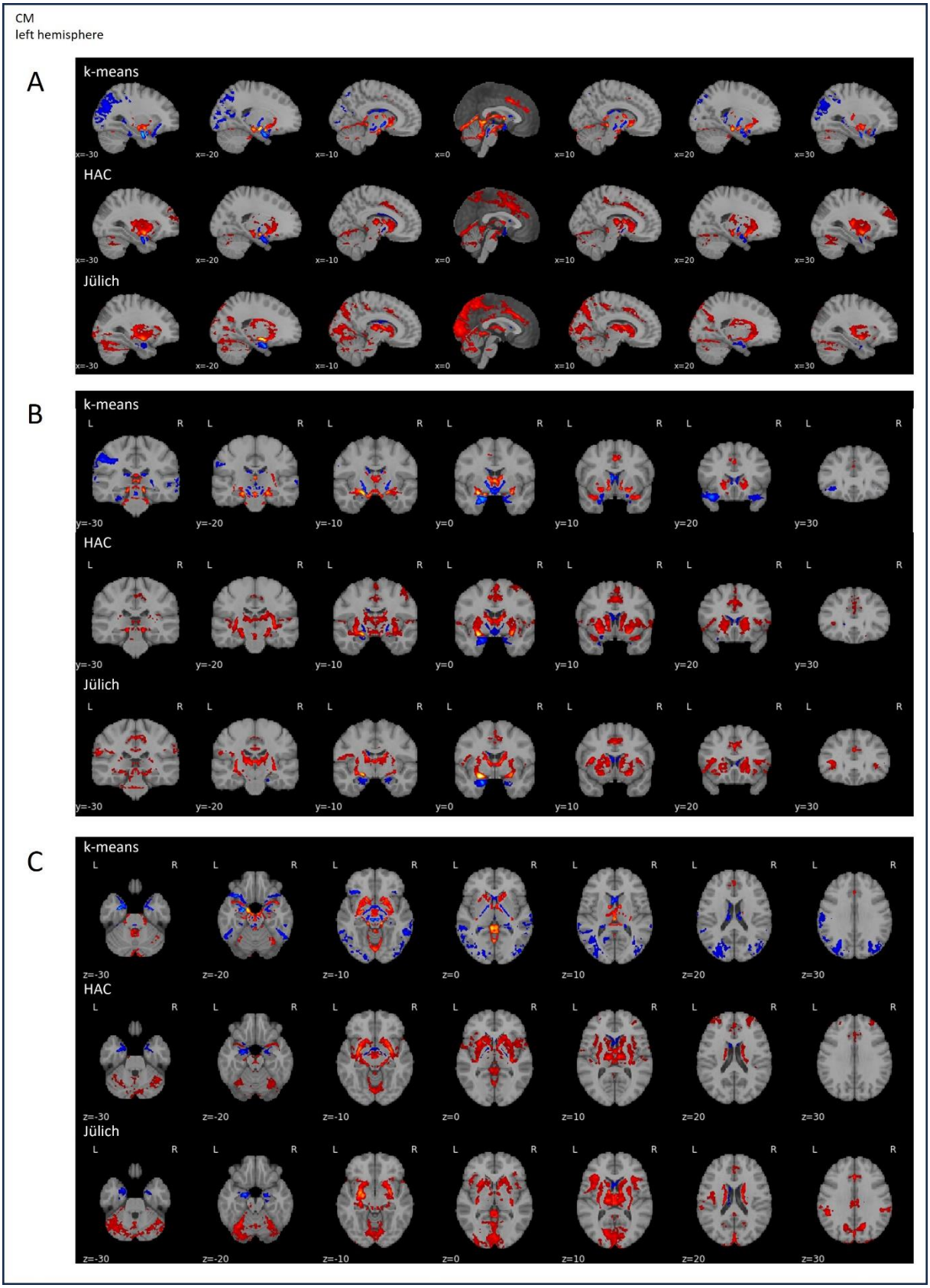

Figure 13 Direct comparison of left hemisphere functional connectivity of CM vs. LB+SF. Red areas indicate a significant positive prediction of fMRI signal and blue areas indicate significant negative predictions. Brighter colours indicate stronger signal association. A voxel-wise threshold ($p \leq 0.001$) and cluster size threshold (min. 1000 voxel) have been applied. The maps are displayed sagittal (A), coronal (B) and axial (C) for k-means, HAC and Jülich derived maps.

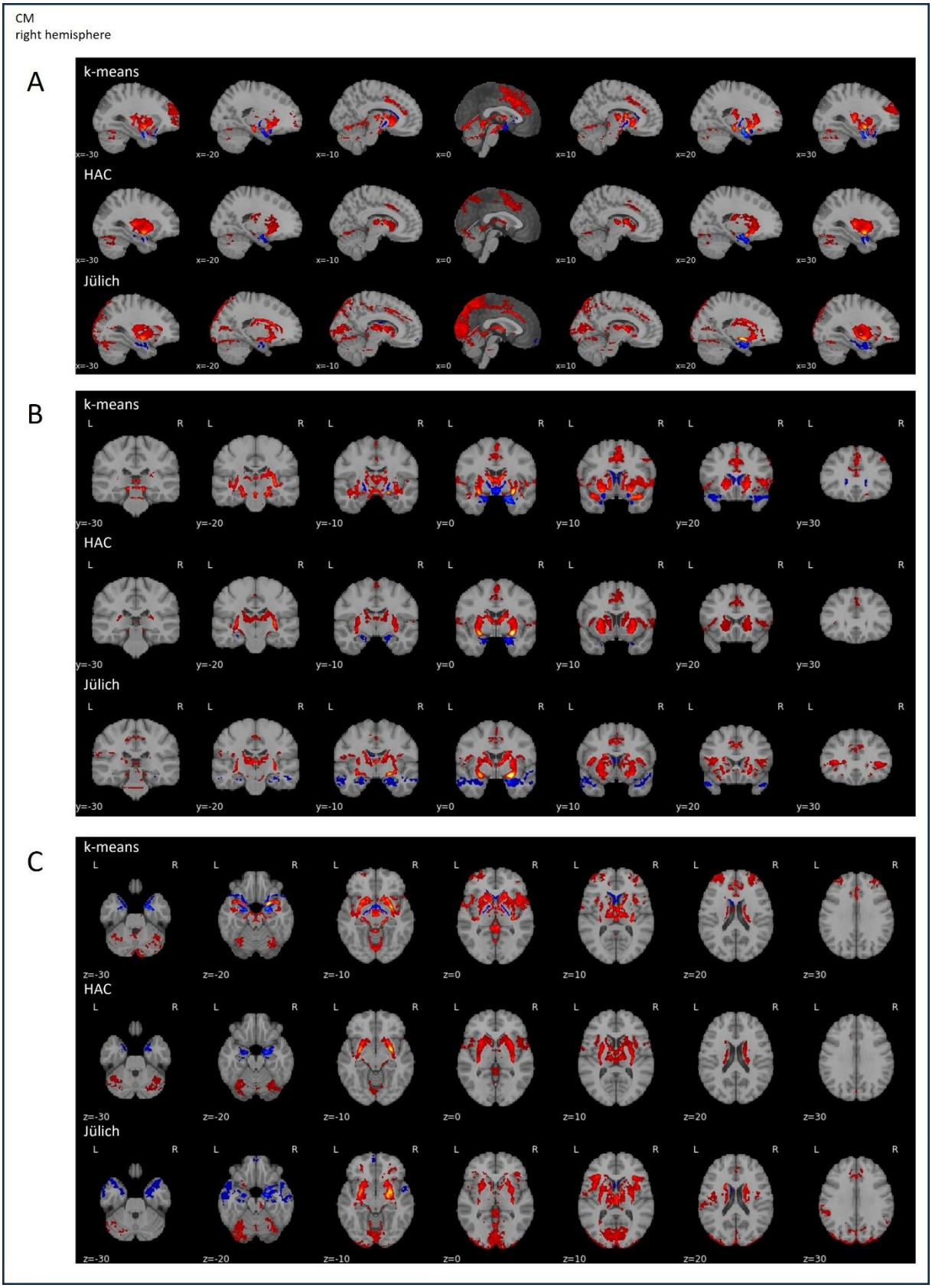

Figure 14 Direct comparison of right hemisphere functional connectivity of CM vs. LB+SF. Red areas indicate a significant positive prediction of fMRI signal and blue areas indicate significant negative predictions. Brighter colours indicate stronger signal association. A voxel-wise threshold ($p \leq 0.001$) and cluster size threshold (min. 1000 voxel) have been applied. The maps are displayed sagittal (A), coronal (B) and axial (C) for k-means, HAC and Jülich derived maps.

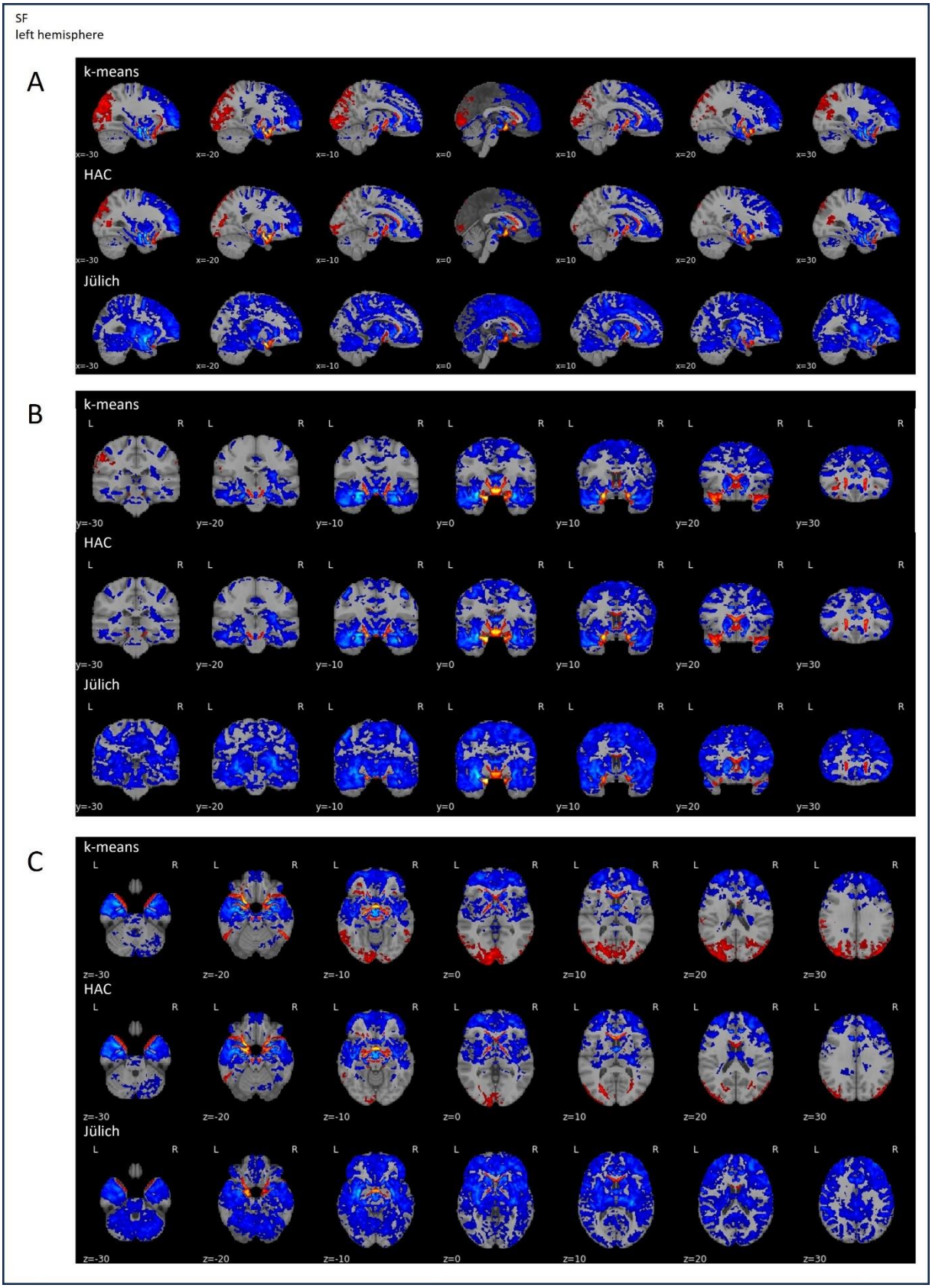

Figure 15 Direct comparison of left hemisphere functional connectivity of SF vs. LB+CM. Red areas indicate a significant positive prediction of fMRI signal and blue areas indicate significant negative predictions. Brighter colours indicate stronger signal association. A voxel-wise threshold ($p \leq 0.001$) and cluster size threshold (min. 1000 voxel) have been applied. The maps are displayed sagittal (A), coronal (B) and axial (C) for k-means, HAC and Jülich derived maps.

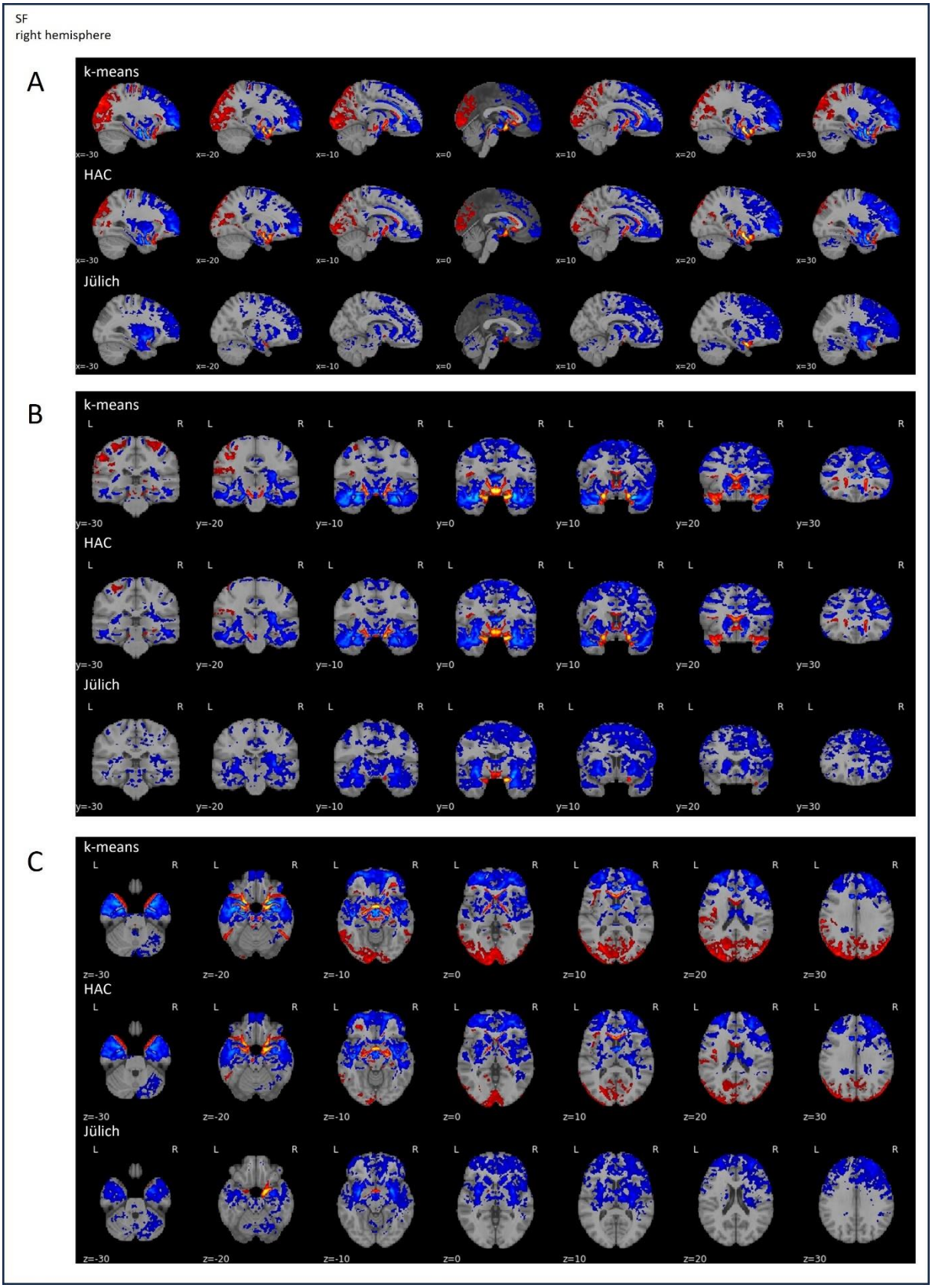

Figure 16 Direct comparison of left hemisphere functional connectivity of SF vs. LB+CM. Red areas indicate a significant positive prediction of fMRI signal and blue areas indicate significant negative predictions. Brighter colours indicate stronger signal association. A voxel-wise threshold ($p \leq 0.001$) and cluster size threshold (min. 1000 voxel) have been applied. For the Jülich condition a cluster threshold of 500 was used to display positive clusters of contralateral SF. The maps displayed sagittal (A), coronal (B) and axial (C) for k-means, HAC and Jülich derived maps.

3.4. Cluster Peaks

In the following section the cluster analysis results, done with *atlasreader* (Notter et al., 2019) will be reported. The *atlasreader* toolbox looks at connectivity clusters and reports the signal peak intensity, size and location of clusters meeting the criteria. The cutoff-criteria used for this analysis is a cluster size of 200 contiguous voxels (1.5 mm^3 per voxel results in clusters of at least 300mm^3). Moreover the algorithm reported peaks within the same cluster, if the Euclidean distance between them was at least 100mm. The identified signal peaks were put into a table along with information describing the clusters they were discovered in and sorted based on their intensity (see Appendix). Only the top ten of both positive and negative signal intensity were considered. The main emphasis of this section will be to report differences and similarities between the k-means, HAC and Jülich derived connectivity maps. An overview of the differences and overlaps in cluster peaks can be found in Table 1 and Table 2.

LB Right

Highest positive and negative signal peak (PSP and NSP) for right hemisphere LB occurred in the right LB itself (Fig. 17) and in right CM (Fig. 18) in all three conditions. K-means and HAC derived connectivity maps showed overlap in the right primary somatosensory cortex (S1) and the ventral tegmental area (VTA), whereas HAC and Jülich derived maps had similar peaks in the premotor cortex (PMC). Coinciding negative signal peaks (NSP's) in all conditions occurred in the left frontal pole, the right anterior insula (aINS) and the anterior cingulate cortex (ACC). Otherwise no overlapping peaks were found.

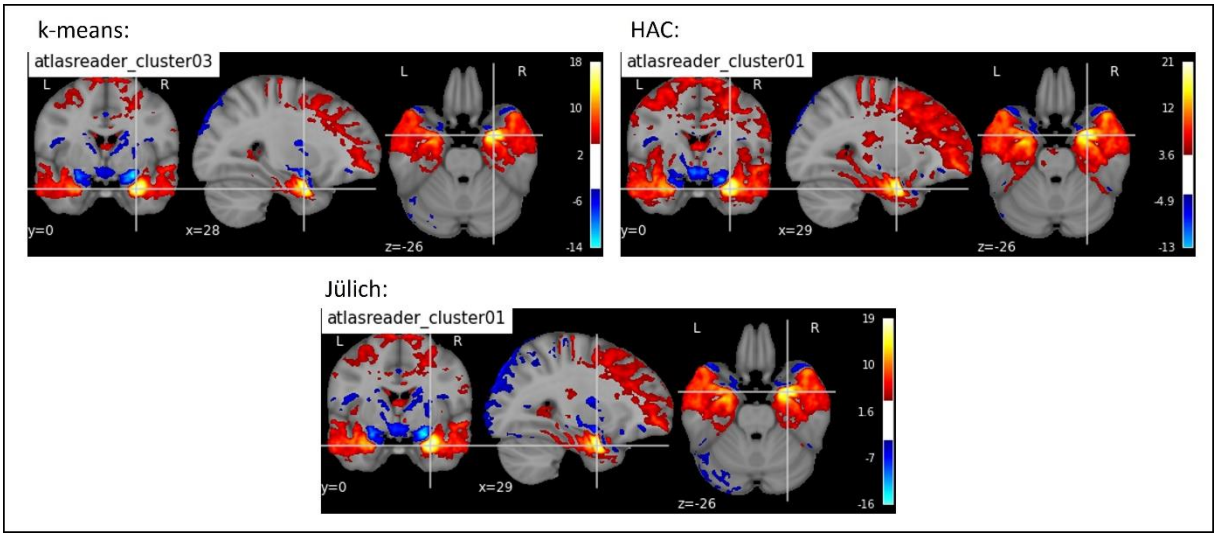

Figure 17 Orthogonal plots at the location of the highest positive cluster peak for right LB in each condition. Cluster ID in the top left corner of each plot correspond to tables in the Appendix. Maps were voxel-wise corrected (*p≤0.001)* and a cluster size thresholded of 200 has been applied.

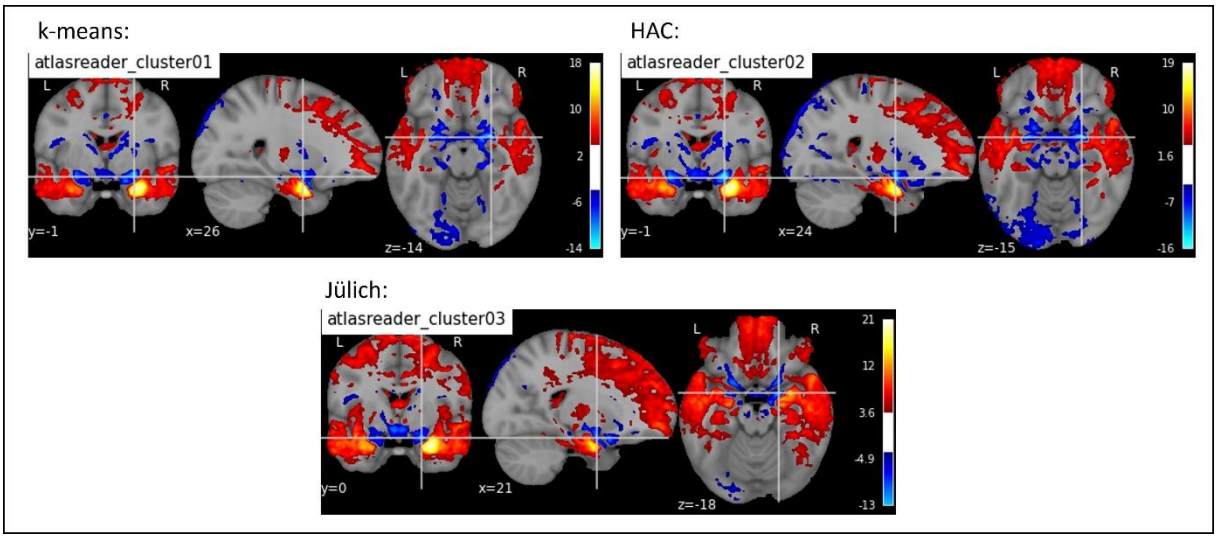

Figure 18 Orthogonal plots at the location of the highest negative cluster peak for right LB in each condition. Cluster ID in the top left corner of each plot correspond to tables in the Appendix. Maps were voxel-wise corrected (*p≤0.001)* and a cluster size thresholded of 200 has been applied.

LB Left

Overlapping PSP in all conditions were only found in the left LB (Fig. 19). Other similarities occurred between k-means and Jülich derived maps in the left PMC and the right Brodmann Area 45 (BA45). Regarding NSP's, only one in the left CM (Fig. 20) was found across all conditions. In the ACC and the left aINS overlaps were found between k-means and HAC derived maps. Converging regions between k-means and Jülich conditions can be seen in nucleus accumbens (NAC) and thalamus (TH).

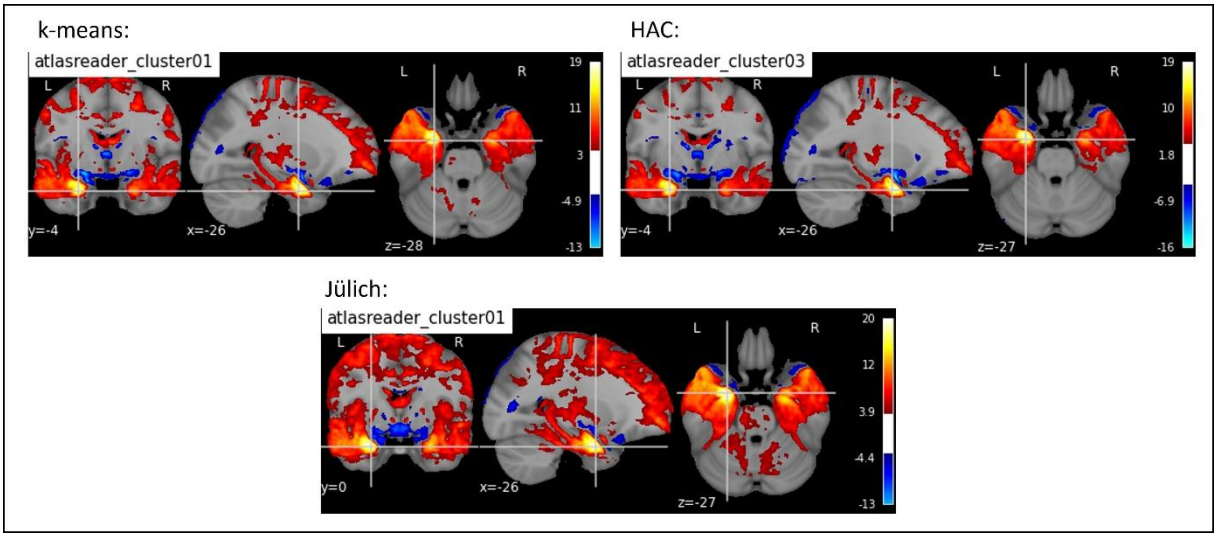

Figure 19 Orthogonal plots at the location of the highest positive cluster peak for left LB in each condition. Cluster ID in the top left corner of each plot correspond to tables in the Appendix. Maps were voxel-wise corrected (*p≤0.001)* and a cluster size thresholded of 200 has been applied.

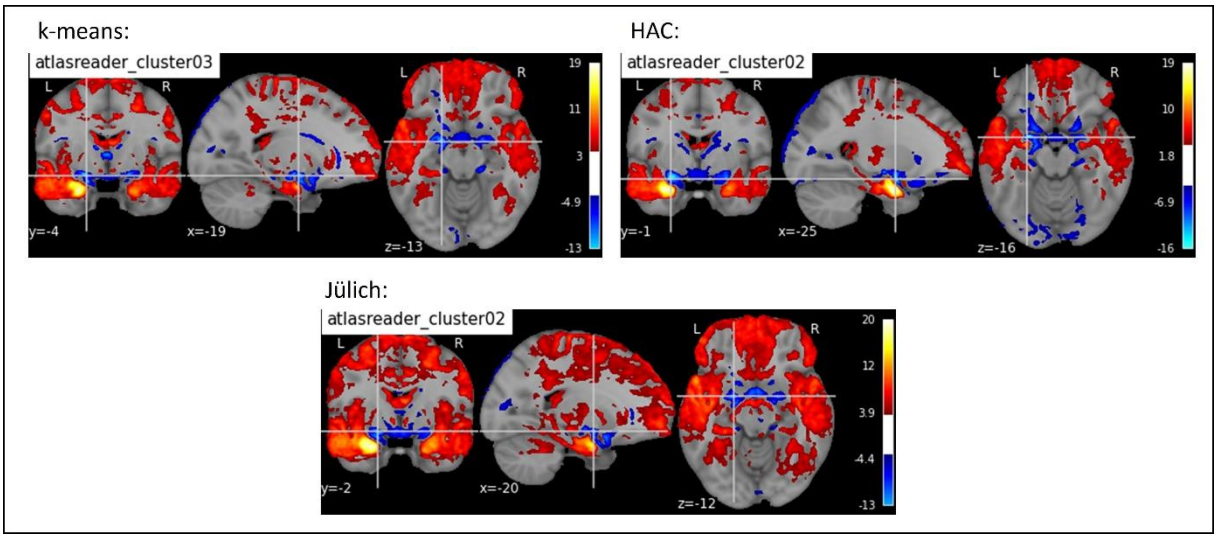

Figure 20 Orthogonal plots at the location of the highest negative cluster peak for left LB in each condition. Cluster ID in the top left corner of each plot correspond to tables in the Appendix. Maps were voxel-wise corrected (*p≤0.001)* and a cluster size thresholded of 200 has been applied.

CM Right

The only overlapping PSP across all conditions was found in the right CM (Fig. 21) itself. All other positive signal similarities occurred between k-means and HAC derived maps, namely peaks in the ACC, the anterior prefrontal cortex (aPFC) and left secondary somatosensory cortex (S2).

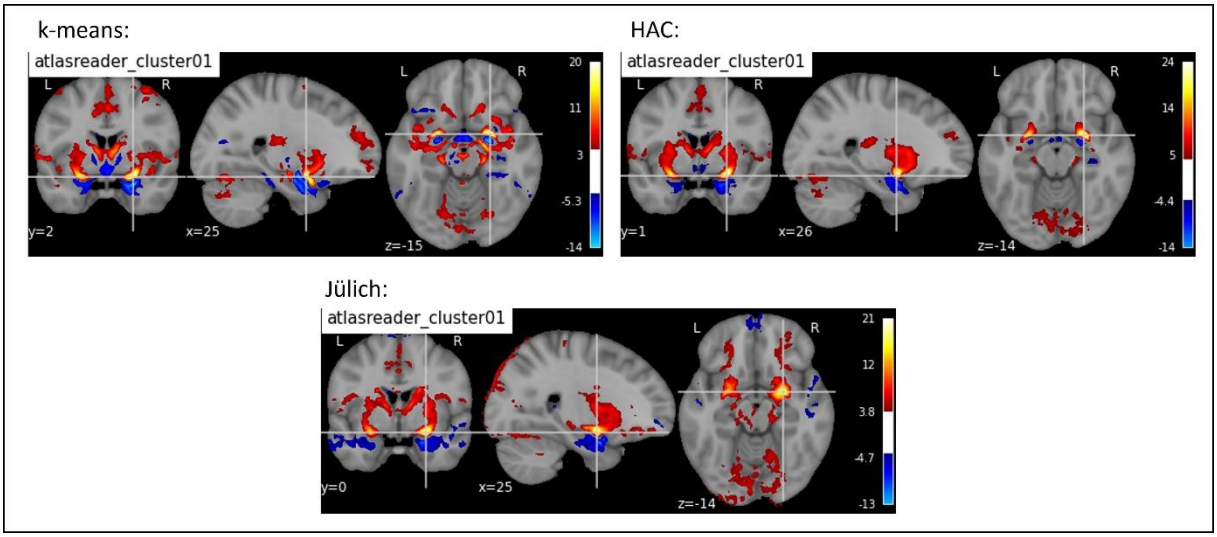

Figure 21 Orthogonal plots at the location of the highest positive cluster peak for right CM in each condition. Cluster ID in the top left corner of each plot correspond to tables in the Appendix. Maps were voxel-wise corrected (*p≤0.001)* and a cluster size thresholded of 200 has been applied.

Table 1

Positive Signal Clusters

	Cluster ID's			
	k-means	HAC	Jülich	Brain Region
LB Right				
	3	1	1	right LB
	9	7		right primary somatosensory cortex BA2
	26	23		right primary somatosensory cortex BA3b
	12	4		ventral tegmental area
		1.2	1.2	premotor cortex
LB Left				
	1	3	1	left LB
	1.2		1.2	left primary moter cortex BA4
	1.3		1.3	right Broca Area BA45
CM Right				
	1	1	(1)	right CM
	2	5		anterior cingulate cortex
	4	9		anterior prefrontal cortex
	9	5		left secondary somatosensory cortex
CM Left				
	2	1	(1)	left CM
	8	3		anterior cingulate cortex
	18	14		brainstem
SF Right				
	3	3	2	right SF
	5	5		nucleus accumbens
	32	31		thalamus
	2	2		right lateral occipital cortex superior division
	7	14		midbrain
SF Left				
	3	3	2	left SF
	5	5	(3)	nucleus accumbens
	7	9		midbrain

Note: The table shows positive signal peaks among the ten highest peaks, that co-occurred in at least two conditions. Cluster ID's refer to atlasreader outputs, which can be found in the appendix for more detailed information. Subitems of one cluster indicate multiple signal peaks found within the same cluster (with at least 100mm distance in between). Cluster ID's in parenthesis indicate that the signal peak is similar to the other(s), but differs considerably nonetheless.

Coinciding NSP's were found bilateral in SF (Fig. 22), although for the right SF k-means and HAC derived maps were more similar opposed to Jülich derived maps. Overlap in the anterior callosum (AC) was found only in k-means and HAC conditions.

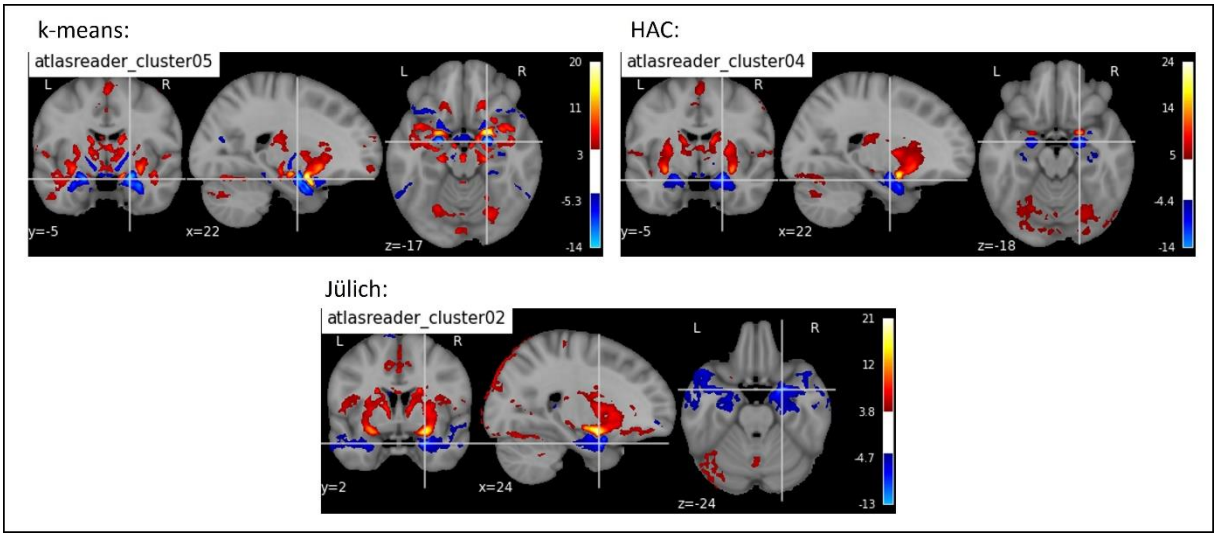

Figure 22 Orthogonal plots at the location of the highest negative cluster peak for right CM in each condition. Cluster ID in the top left corner of each plot correspond to tables in the Appendix. Maps were voxel-wise corrected (*p≤0.001)* and a cluster size thresholded of 200 has been applied.

Table 2

Negative Signal Clusters present in all three conditions

	Cluster ID's			
	k-means	HAC	Jülich	Brain Region
LB Right				
	14	9	12	left frontal pole
	6	3	8	right anterior insula
	1	2	3	right CM
	7	5	13	anterior cingulate cortex
LB Left				
	3	2	2	left CM
	15	10		anterior cingulate cortex
	6	6		left anterioir insula
	9		10	nucleus accumbens
	4		12	thalamus
CM Right				
	5	4	(2)	right SF
	6	6	3	left SF
	8	16		anterior callosum
CM Left				
	4	5	3	left SF
	7	10	(4)	right SF
		11	18	left temporal pole
SF Right				
	1.1	1.1	1.1	right CM
	1.2	1.2	1.2	right premotor cortex
	8	7		primary somatosensory cortex
SF Left				
	1.1	1.1	(1.1)	left CM
	1.2	1.2	(1.2)	right premotor cortex
	1.3	1.3		right cerebellum
	6	4		left primary somatosensory cortex
	20	27		right primary motor cortex

Note: The table shows negative signal peaks among the ten highest peaks, that co-occurred in at least two conditions. Cluster ID's refer to atlasreader outputs, which can be found in the appendix for more detailed information. Subitems of one cluster indicate multiple signal peaks found within the same cluster (with at least 100mm distance in between). Cluster ID's in parenthesis indicate that the signal peak is similar to the other(s), but differs considerably nonetheless.

CM Left

For the left CM parallels in PSP's across all conditions were found in itself (Fig. 23). Like in the right CM, all other similarities can be seen only between k-means and HAC derived maps in

the ACC and the brainstem. NSP's are again similar to the right hemisphere, occurring across all conditions bilaterally in SF (Fig. 24). However, the only other co-occurrence can be found between HAC and Jülich derived maps in the left temporal pole.

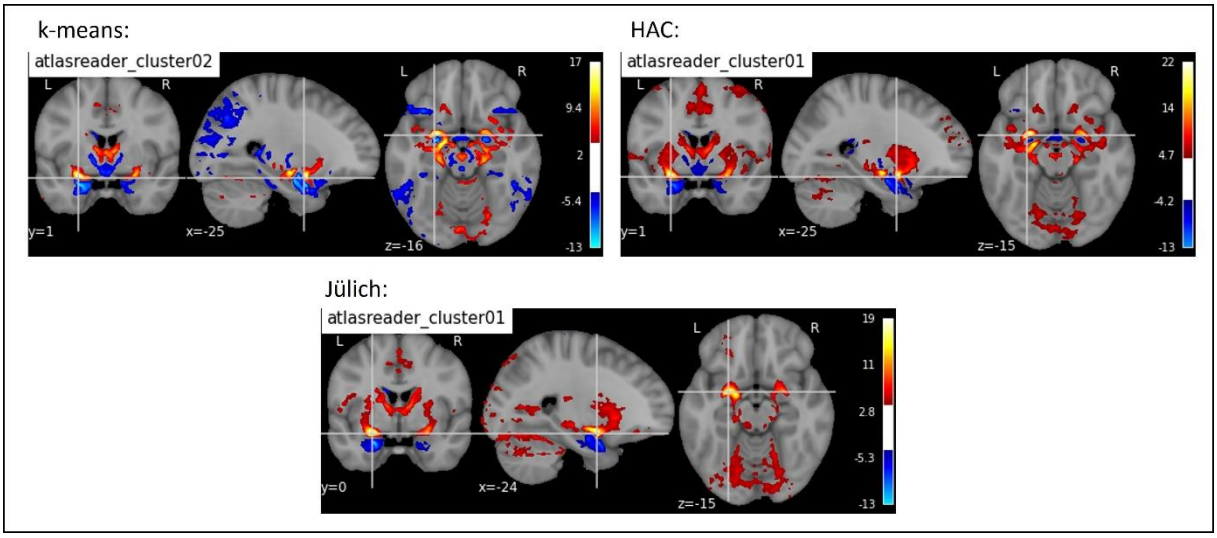

Figure 23 Orthogonal plots at the location of the highest positive cluster peak for left CM in each condition. Cluster ID in the top left corner of each plot correspond to tables in the Appendix. Maps were voxel-wise corrected (*p≤0.001)* and a cluster size thresholded of 200 has been applied.

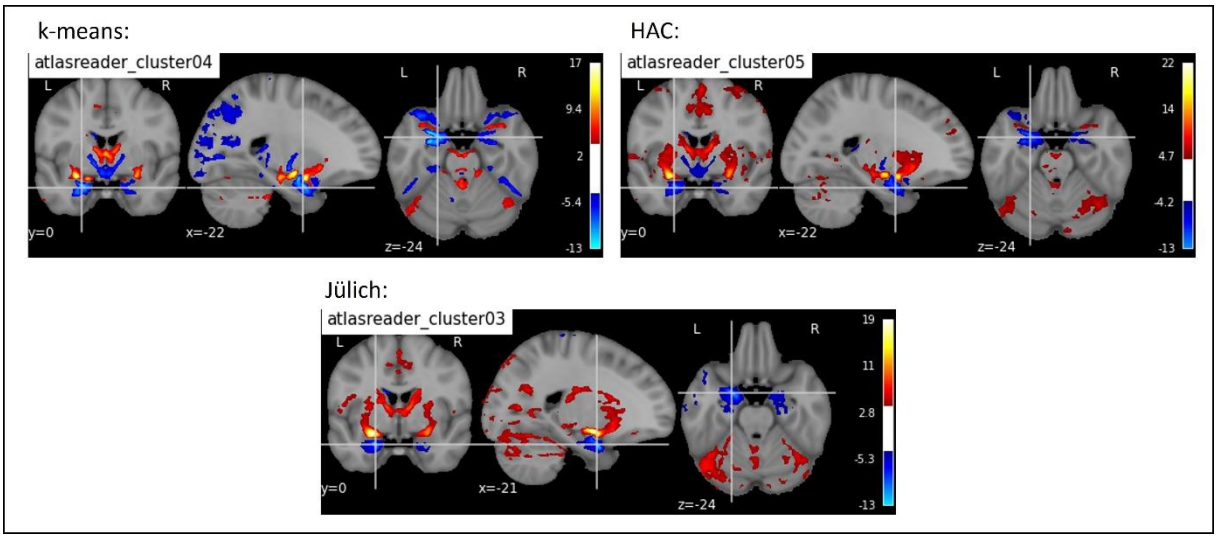

Figure 24 Orthogonal plots at the location of the highest negative cluster peak for left CM in each condition. Cluster ID in the top left corner of each plot correspond to tables in the Appendix. Maps were voxel-wise corrected (*p≤0.001)* and a cluster size thresholded of 200 has been applied.

SF Right

For right hemisphere SF PSP's only the auto-associated cluster was found across all conditions (Fig. 25). All other similar PSP's occurred parallel in k-means and HAC conditions in the anterior callosum, the TH, right lateral occipital cortex and midbrain. For NSP's two peaks in the same cluster were found for all three conditions. The regions these NSP's occurred in were the right

CM (Fig. 26) and the right PMC. The only other similar NSP was found between k-means and HAC derived maps in right S1.

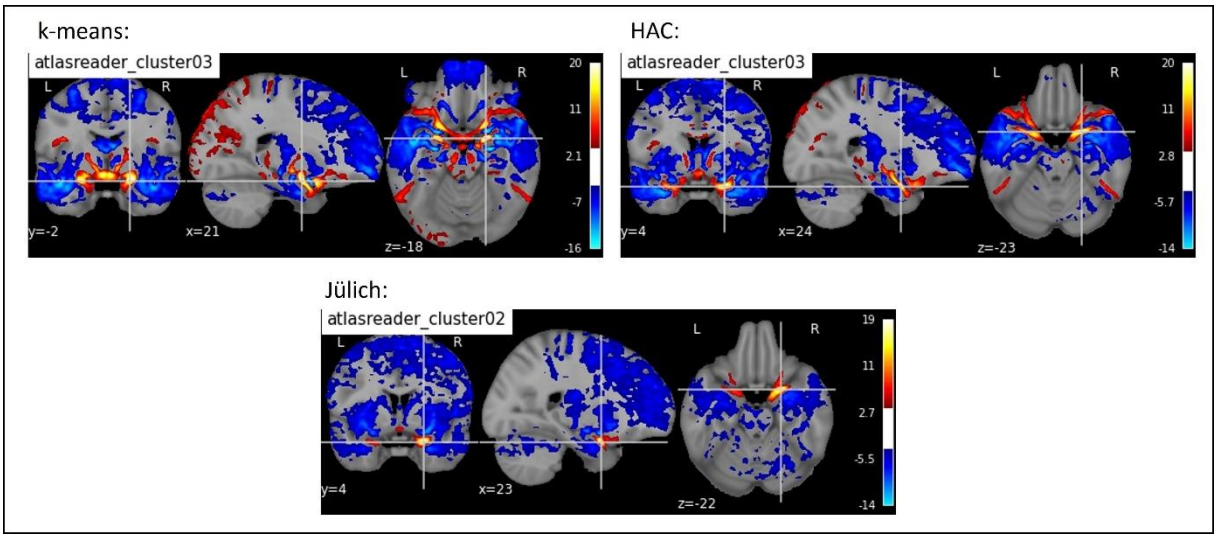

Figure 25 Orthogonal plots at the location of the highest positive cluster peak for right SF in each condition. Cluster ID in the top left corner of each plot correspond to tables in the Appendix. Maps were voxel-wise corrected (*p≤0.001)* and a cluster size thresholded of 200 has been applied.

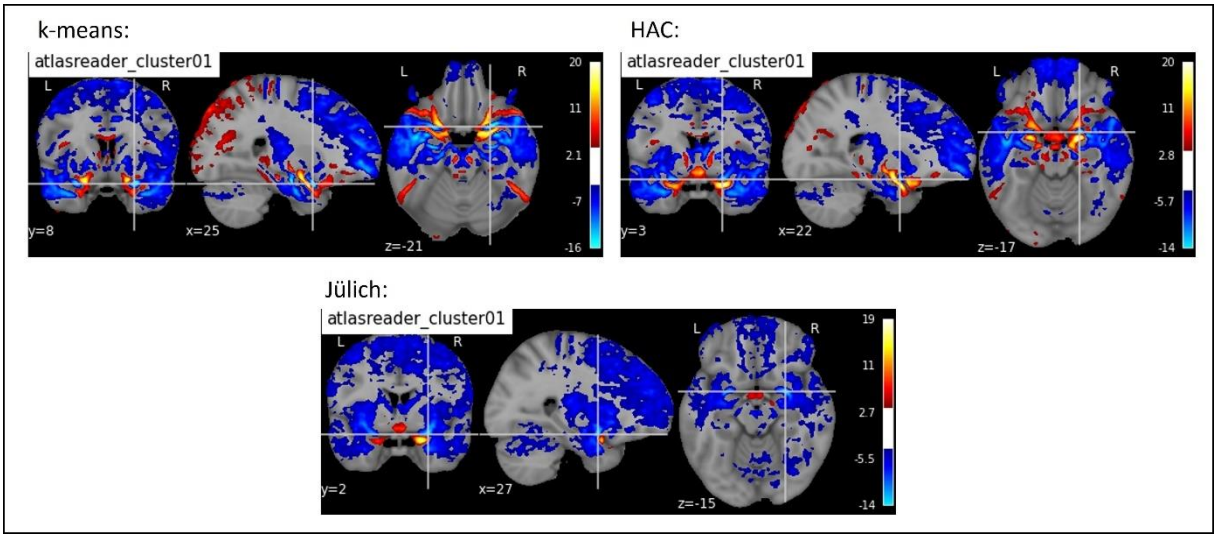

Figure 26 Orthogonal plots at the location of the highest negative cluster peak for right SF in each condition. Cluster ID in the top left corner of each plot correspond to tables in the Appendix. Maps were voxel-wise corrected (*p≤0.001)* and a cluster size thresholded of 200 has been applied.

SF Left

In left hemisphere SF, PSP's occurring in all three conditions can be seen in the left SF (Fig. 27) and the anterior callosum. The only other PSP, found in the midbrain, arose in both k-means and HAC derived maps. Looking at the NSP's it can be seen that three peaks occurred in the same cluster. The first two peaks can be found in all three conditions, in the left CM (Fig. 28) and the right PMC. Another NSP of this cluster that was reported under the selected peaks is located in the right cerebellum for k-means and HAC derived maps. The fact that the cluster

peaks are this far apart, makes it unlikely that they truly belong to the same cluster. However for this comparison the location and intensity of the signal peak are the information of interest. The only other similarities were found between k-means and HAC conditions and occurred in the left S1 and the right PMC.

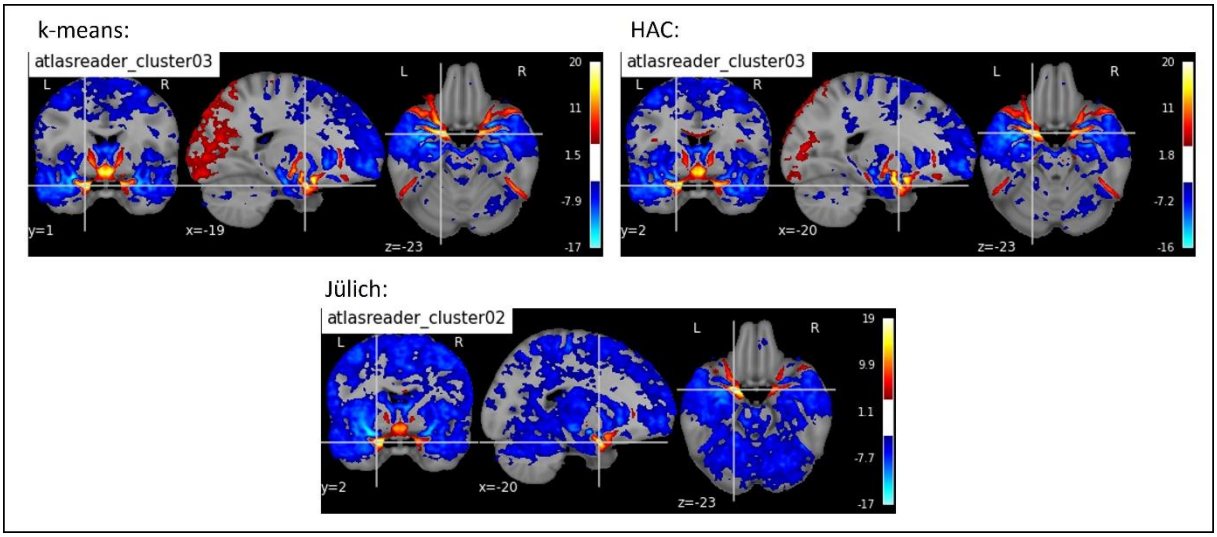

Figure 27 Orthogonal plots at the location of the highest positive cluster peak for left SF in each condition. Cluster ID in the top left corner of each plot correspond to tables in the Appendix. Maps were voxel-wise corrected (*p≤0.001)* and a cluster size thresholded of 200 has been applied.

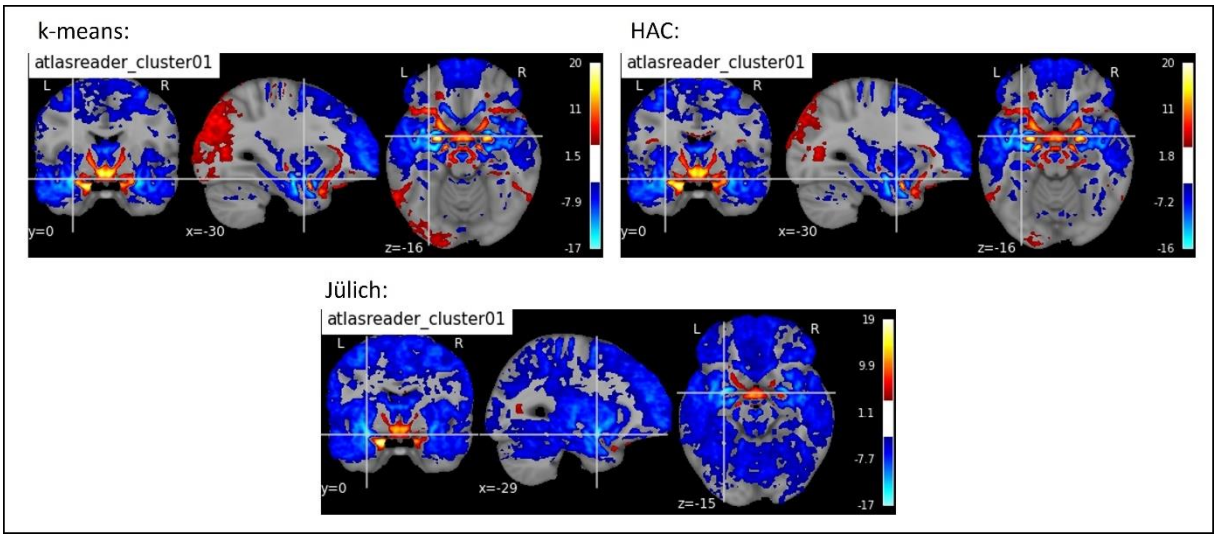

Figure 28 Orthogonal plots at the location of the highest negative cluster peak for left SF in each condition. Cluster ID in the top left corner of each plot correspond to tables in the Appendix. Maps were voxel-wise corrected (*p≤0.001)* and a cluster size thresholded of 200 has been applied.

4. Discussion

Applying the k-means and hierarchical agglomerative clustering algorithms to high resolution resting-state fMRI data, masked by a 50^{th} percentile probabilistic atlas has yielded parcellations into amygdala-subregions that are definitely comparable to the subregions defined by the Jülich probabilistic atlas. As has been shown in the simulation, the algorithms return clusters that are analogous to the ground truth of the simulation data when, in case of k-means clustering, the number of iterations parameter (n_{init}) is set above 50. Of course the simulated data is not an exact resemblance of real fMRI data, but it inherits similar conditions. These conditions are granted by the nature of the used signal weights, which have the highest value at the centre of mass of the subregion they are intended to represent and a continuous decrease towards its periphery. Along with this, the maximal weight-values are differing between the subregions, which represents different (measured) signal strengths, a circumstance which gave insights into how the algorithms would react to these conditions. Even though all analysed signals are standardised, the difference in signal to noise ratio most likely has an impact on the signal amplitudes. Another feature of the simulated data that is shared with real fMRI data is the mixing of signals in the transition areas of adjacent subregions. The assumptions that this signal mixing occurs is not necessarily based on neurophysiological properties, but rather on the probabilistic nature of fMRI group analysis. Even when the signals do not mix in single subject recordings, they probably will do so after group level analysis, as the location of small brain regions as amygdala subregions will not be aligned across all participants. Signal mixing in the simulation does probably not occur in real data in the same way, but again, these circumstances allowed testing of the algorithm's behaviour. As can be seen, when applying the k-means algorithm to masked data with a low n_{init} parameter, the algorithm seems to have problems separating signals of the conjunction between two subregions and declares it as a separate region. This behaviour could be corrected by changing $n_{init} = 1$ to $n_{init} = 50$. Although, the problem reoccurred with increasing noise, where the algorithm seemed to include proportionally larger parts of the transition area between LB and CM into the CM cluster (Fig. 4D). The HAC algorithm on the other hand had seemingly no problems with detecting the transition areas as part of the encircling clusters.

Both algorithms yielded parcellations of the amygdala that resemble the widely used subdivisions defined by the Jülich Probabilistic Brain Atlas (Fig. 7). Although the laterobasal

cluster corresponds quite well between the three parcellations in terms location, the clusters that are suspected to be centromedial and superficial subdivisions are not as homogeneous across the three parcellations regarding their size and shape. In both clustering algorithms SF is noticeably larger than the corresponding structure in the Jülich atlas, especially in HAC. In contrast to Jülich subdivisions (Fig. 7C) the clusters yielded by k-means (Fig. 2A) and HAC (Fig. 2B) show that the supposed SF is extending into large portions of CM. In the k-means condition the CM cluster is wrapping around SF, which means that the CM cluster is present in the anterior/posterior and lateral/medial periphery, although in form of a continuous cluster. This can also be observed in Figure 26 where the positive connectivity cluster of SF and negative connectivity cluster of CM are intertwined. The SF cluster appears to be located in between LB and CM and entails large areas of Jülich CM. A similar case can be observed in the HAC clusters, where CM is on the one hand more concentrated, location wise, but SF is covering a lot of Jülich CM region as well.

As described above, the simulation results give reason to assume that signal mixing in transition areas was not causing substantial distortions in the resulting clusters. This lowers the probability that an area with mixed signals was declared a separate cluster. The case that the whole transition area, or large parts of it, was assigned to SF is possible due to similar behaviour in the simulation, but obtained evidence is not very clear. Furthermore, the fact that measured fMRI signal of a region of interest is tied to the probabilistic spatial properties mentioned above, leads to the assumption that smaller brain regions underlie higher spatial inaccuracies and thus exhibit weaker signal strength. According to the probabilistic properties of the Jülich atlas CM and SF regions, SF had higher probabilistic values than CM. Consequently CM should have been affected more by spatial inaccuracies, which would have led to higher probability of SF signal being dominant in the transition area as opposed to CM signal. The fact that areas that are part of CM in the Jülich atlas were denominated as SF by both clustering algorithms makes this at least a plausible explanation and suggests that differences in signal strength impose a limitation to unsupervised clustering.

Another explanation for this result could be that the algorithms were detecting a signal that is not part of any amygdala subregion and that the supposed CM is either noise or signal that belongs to another neighbouring structure, whereas SF entails both SF and CM. This particular case was not tested in the simulation, but from trials without masking it is evident that both

algorithms were able to detect all three subregions sufficiently without applying a mask. This shows that the algorithms can handle the lack of signal, but do not account for the mask entailing a fourth signal cluster. In this case the mathematical formalities of the algorithms would suggest that they are merging voxels that are most similar to each other. If a non-amygdala signal appears inside the masks border, then it can be assumed that this signal differs from both CM and SF signal more than the two amygdaloid subregions would differ from each other, hence merging CM and SF to one cluster. To clarify whether the clusters found by both algorithms are part of the amygdala and if so, which parts they represent, we have to look at the obtained connectivity maps.

As can be seen in the glass brain plots in section 3.1.1 the signal distribution that varies most across all three parcellations are the ones for CM and SF. In LB differences are apparent as well, but opposed to CM and SF positive and negative signal associations are always in the same location and only the cluster sizes seem to change. For CM maps positive/negative distribution of the left hemisphere k-means derived plots differ substantially from HAC and Jülich derived plots and for SF maps of both hemispheres signal distribution of k-means and HAC plots differ a lot from Jülich plots. These global signal patterns indicate, like the observations of obtained clusters, that there is indeed a difference between CM and SF connectivity maps across at least some of the three methods.

Direct comparison maps of LB vs. CM+SF in the Jülich condition predicted positive signals in the same regions as HAC, namely in striatum, hippocampus, anterior insula, putamen, lateral thalamus, posterior thalamus and ACC. For k-means derived maps we only see this positive signal associations in hippocampus, marginally in lateral thalamus, posterior thalamus and ACC. The centromedial amygdala's role as an output region associated with ACC, putamen, insula and thalamus (Roy, 2009; Davis, 1997) is explained better by the predictions made by HAC and Jülich derived CM. Positive connectivity to the bed nucleus of the stria terminalis (BNST) in all three conditions is in line with literature (Tillman, 2018; Gorka, 2018). The left hemisphere CM cluster connectivity obtained by k-means is missing predictions of signal in the insula, which has been proven to be associated with centromedial amygdala (Kargl et al. 2020; Tillman et al. 2018). Marginal association with the anterior insula cortex can be seen in k-means derived right hemisphere CM, but not as prominent and consistent as in the other two conditions. Another region that is known to be associated with centromedial amygdala nuclei

is the hypothalamus (Weera et al, 2021; Ballotta et al, 2021). Negative signal predictions are made by HAC and k-means CM clusters of the left hemisphere and only for the k-means CM cluster of the right hemisphere. Comparing these findings with existing literature, it is to assume that the CM cluster obtained by the HAC algorithm and the Jülich atlas CM exhibit more plausible functional connectivity. Due to HAC CM's associations with hypothalamus this cluster proofs to be an even better fit than the Jülich atlas CM.

Looking at the direct comparison maps for SF vs. LB+CM, it can be seen that almost all regions associated with k-means and HAC SF clusters are also associated with Jülich SF, except for positive associations of visual cortex and brain stem. In the Jülich derived maps the clusters are spread across large areas of the cortex with no visible regions of high intensity z-values. This could be a sign that the Jülich atlas SF was spatially less accurate than the SF clusters obtained by clustering algorithms. Examining functional connectivity maps of k-means and HAC SF clusters it is evident that there is a more fine grained and detailed spreading of both negative connectivity into limbic regions from the superficial amygdala. Connectivity of SF with ACC, caudate, nucleus accumbens and hippocampus was also found by Roy et al. (2009). Negative associations with vmPFC and LB, with the cluster extending into the temporal lobe indicate a contrasting connectivity of SF to LB. The fact that SF negatively predicted activation in BNST in all three conditions indicates contrast to the CM connectivity maps.

Evidence obtained from the cluster peak analysis shows that positive as well as negative cluster peaks of k-means and HAC conditions are much more similar to each other than to the Jülich condition for CM and SF in both hemispheres. For LB the degree of overlapping cluster peaks vary across the modalities. This suggests that k-means and HAC clustering algorithms parcellated the amygdala into subregions that also compare to each other on a detailed functional connectivity level and at the same time differ from the connectivity maps obtained by the widely used Jülich brain atlas. The cluster peaks obtained from the clustered regions provide evidence that functional connectivity is in line with literature. For instance, positive peaks in right hemisphere CM occur in ACC and anterior prefrontal cortex, which are regions associated with pain, a mechanism the centromedial amygdala is associated with (Neugebauer, 2015)

Signal peaks of SF in brain stem, cerebellum and motor cortex suggest that areas of the CM have been attributed to the wrong cluster since these regions are believed to receive input

from centromedial amygdala nuclei to facilitate fast motor responses (Simons et al., 2014; LeDoux et al. 1988). On the other hand, a study conducted by Koelsch and Skouras (2014) found a functional connectivity network of the superficial amygdala associated with joyful stimuli rather than fearful stimuli. This network connects SF first and foremost to LB, hypothalamus and striatum, but also to hippocampus, thalamus, cerebellum and regions responsible for attention, sensorimotor function and vision. These connections can also be seen in the connectivity maps of SF obtained by the clustering algorithms in form of PSP's in thalamus, midbrain and occipital lobe (see Table 1), NSP's in cerebellum and somatosensory regions (see Table 2) and overall significant signal association in hypothalamus, striatal regions, hippocampus, brain stem and visual cortex (Fig. 15 and 16). Furthermore, connectivity patterns of SF derived from clustering algorithms yield much more detailed connections in contrast to their Jülich atlas counterparts. These qualitative observations paired with the above described parallels to literature do indeed suggest that the clustered SF is fitting the data at hand better than the default Jülich atlas SF.

Lastly, functional connectivity direct comparison of LB vs. CM+SF has been largely consistent across the three conditions and is in line with literature. This can be derived from association with auditory cortex and vmPFC, as well as PSP's in somatosensory cortex, indicating the LB's involvement in regulating sensory processes (Canteras & Swanson, 1992; LeDoux, 2007).

5. Concluding Remarks

Functional connectivity of the obtained clusters has delivered mixed results. On the one hand many connections can be validated by literature, but on the other hand some inconsistencies remain. These inconsistencies most prominently entail significant positive association of regions relevant for motor control with SF instead of CM. Interestingly, the more general signal associations of HAC's and Jülich's CM are more in line with literature than k-means. However, looking at the cluster peaks it is evident that parallels here are almost exclusively shared by the two clustering conditions in CM and SF, indicating a similarity concerning the processing hubs. Nonetheless, these processing hubs are subject to the before mentioned inconsistencies, suggesting that the clustering algorithms are underlying inaccuracies, even when applied to high resolution fMRI data of a large number of subjects. These inaccuracies are most likely due to the algorithms problems of handling data with deviating signal strength

discussed earlier. Moreover, the sample entailed a large proportion of neurodivergent individuals with conditions known to affect amygdala function. In future studies neurodivergent participants have to be accounted for .

Taking a few steps back to look at the whole picture these results suggest that unsupervised clustering methods can indeed be taken as a feasible method to derive parcellations of the human amygdala. Further, it is evident that these derived clusters might even provide a better fit to the data at hand than the normative Jülich atlas. To further build upon this initial proof of concept, steps, such as subjecting the data to principle components analysis, counteracting the problems identified in this thesis, can be implemented. With contemporary amygdala models getting progressively detailed, normative references like the Jülich brain atlas fail more and more to accommodate for this specificity. Thus, effective application for these promising unbiased machine learning based methods have to be found to improve *in vivo* functional examination of the human amygdala.

References

Abraham, A., Pedregosa, F., Eickenberg, M., Gervais, P., Mueller, A., Kossaifi, J., Gramfort, A., Thirion, B., & Varoquaux, G. (2014). Machine learning for neuroimaging with scikit-learn. Frontiers in Neuroinformatics, 8. https://www.frontiersin.org/article/10.3389/fninf.2014.00014

Amunts, K., Kedo, O., Kindler, M., Pieperhoff, P., Mohlberg, H., Shah, N. J., Habel, U., Schneider, F., & Zilles, K. (2005). Cytoarchitectonic mapping of the human amygdala, hippocampal region and entorhinal cortex: Intersubject variability and probability maps. Anatomy and Embryology, 210(5), 343–352. https://doi.org/10.1007/s00429-005-0025-5

Amunts, K., Mohlberg, H., Bludau, S., & Zilles, K. (2020). Julich-Brain: A 3D probabilistic atlas of the human brain's cytoarchitecture. Science, 369(6506), 988–992. https://doi.org/10.1126/science.abb4588

Arthur, D., & Vassilvitskii, S. (2007). k-means++: The advantages of careful seeding. Proceedings of the Eighteenth Annual ACM-SIAM Symposium on Discrete Algorithms, 1027–1035.

Avants, B. B., Tustison, N. J., Song, G., Cook, P. A., Klein, A., & Gee, J. C. (2011). A reproducible evaluation of ANTs similarity metric performance in brain image registration. NeuroImage, 54(3), 2033–2044. https://doi.org/10.1016/j.neuroimage.2010.09.025

Ballotta, D., Talami, F., Pizza, F., Vaudano, A. E., Benuzzi, F., Plazzi, G., & Meletti, S. (2021). Hypothalamus and amygdala functional connectivity at rest in narcolepsy type 1. NeuroImage. Clinical, 31, 102748. https://doi.org/10.1016/j.nicl.2021.102748

Blumensath, T., Jbabdi, S., Glasser, M. F., Van Essen, D. C., Ugurbil, K., Behrens, T. E. J., & Smith, S. M. (2013). Spatially constrained hierarchical parcellation of the brain with resting-state fMRI. NeuroImage, 76, 313–324. https://doi.org/10.1016/j.neuroimage.2013.03.024

Burdach, K. F. (1826). Vom Baue und Leben des Gehirns. Dyk.

Bzdok, D., Laird, A. R., Zilles, K., Fox, P. T., & Eickhoff, S. B. (2013). An investigation of the structural, connectional, and functional subspecialization in the human amygdala. Human Brain Mapping, 34(12), 3247–3266. https://doi.org/10.1002/hbm.22138

Cannon, W. B. (1927). The James-Lange theory of emotions: A critical examination and an alternative theory. The American Journal of Psychology, 39, 106–124. https://doi.org/10.2307/1415404

Canteras, N. S., & Swanson, L. W. (1992). Projections of the ventral subiculum to the amygdala, septum, and hypothalamus: A PHAL anterograde tract-tracing study in the rat. Journal of Comparative Neurology, 324(2), 180–194. https://doi.org/10.1002/cne.903240204

Chen, G., Saad, Z. S., Britton, J. C., Pine, D. S., & Cox, R. W. (2013). Linear mixed-effects modeling approach to FMRI group analysis. NeuroImage, 73, 176–190. https://doi.org/10.1016/j.neuroimage.2013.01.047

Cheng, H., & Fan, Y. (2014). Semi-supervised clustering for parcellating brain regions based on resting state fMRI data. Medical Imaging 2014: Image Processing, 9034, 574–581. https://doi.org/10.1117/12.2043467

Davis, M. (1997). Neurobiology of fear responses: The role of the amygdala. The Journal of Neuropsychiatry and Clinical Neurosciences, 9(3), 382–402. https://doi.org/10.1176/jnp.9.3.382

Davis, M., Walker, D. L., Miles, L., & Grillon, C. (2010). Phasic vs Sustained Fear in Rats and Humans: Role of the Extended Amygdala in Fear vs Anxiety. Neuropsychopharmacology, 35(1), 105–135. https://doi.org/10.1038/npp.2009.109

de Olmos, S. (2004). Amygdala. In The Human Nervous System (pp. 739–868). https://doi.org/10.1016/B978-012547626-3/50023-5

Dice, L. R. (1945). Measures of the Amount of Ecologic Association Between Species. Ecology. https://doi.org/10.2307/1932409

Eickhoff, S. B., Yeo, B. T. T., & Genon, S. (2018). Imaging-based parcellations of the human brain. Nature Reviews Neuroscience, 19(11), Article 11. https://doi.org/10.1038/s41583-018-0071-7

Friston, K. J., Holmes, A. P., Price, C. J., Büchel, C., & Worsley, K. J. (1999). Multisubject fMRI Studies and Conjunction Analyses. NeuroImage, 10(4), 385–396. https://doi.org/10.1006/nimg.1999.0484

Goosens, K. A., & Maren, S. (2001). Contextual and Auditory Fear Conditioning are Mediated by the Lateral, Basal, and Central Amygdaloid Nuclei in Rats. Learning & Memory, 8(3), 148–155. https://doi.org/10.1101/lm.37601

Gorka, A. X., Torrisi, S., Shackman, A. J., Grillon, C., & Ernst, M. (2018). Intrinsic functional connectivity of the central nucleus of the amygdala and bed nucleus of the stria terminalis. NeuroImage, 168, 392–402. https://doi.org/10.1016/j.neuroimage.2017.03.007

Grunau, C., Özüdoğru, A. A., Rozhoň, V., & Tětek, J. (2022). A Nearly Tight Analysis of Greedy k-means++ (arXiv:2207.07949). arXiv. https://doi.org/10.48550/arXiv.2207.07949

Hawrylycz, M. J., Lein, E. S., Guillozet-Bongaarts, A. L., Shen, E. H., Ng, L., Miller, J. A., van de Lagemaat, L. N., Smith, K. A., Ebbert, A., Riley, Z. L., Abajian, C., Beckmann, C. F., Bernard, A., Bertagnolli, D., Boe, A. F., Cartagena, P. M., Chakravarty, M. M., Chapin, M., Chong, J., Jones, A. R. (2012). An anatomically comprehensive atlas of the adult human brain transcriptome. Nature, 489(7416), 391–399. https://doi.org/10.1038/nature11405

Heimer, L., de Olmos, J. S., Alheid, G. F., Pearson, J., Sakamoto, N., Shinoda, K., Marksteiner, J., & Switzer, R. C. (1999). Chapter II - The human basal forebrain. Part II. In F. E. Bloom, A. Björklund, & T. Hökfelt (Eds.), Handbook of Chemical Neuroanatomy (Vol. 15, pp. 57–226). Elsevier. https://doi.org/10.1016/S0924-8196(99)80024-4

Johnston, J. B. (1923). Further contributions to the study of the evolution of the forebrain. The Journal of Comparative Neurology, 35(5), 337–481. https://doi.org/10.1002/cne.900350502

Kargl, D., Kaczanowska, J., Ulonska, S., Groessl, F., Piszczek, L., Lazovic, J., Buehler, K., & Haubensak, W. (2020). The amygdala instructs insular feedback for affective learning. eLife, 9, e60336. https://doi.org/10.7554/eLife.60336

Khosla, M., Jamison, K., Ngo, G. H., Kuceyeski, A., & Sabuncu, M. R. (2019). Machine learning in resting-state fMRI analysis. Magnetic Resonance Imaging, 64, 101–121. https://doi.org/10.1016/j.mri.2019.05.031

Klüver, H. (1939). PRELIMINARY ANALYSIS OF FUNCTIONS OF THE TEMPORAL LOBES IN MONKEYS. Archives of Neurology And Psychiatry, 42(6), 979. https://doi.org/10.1001/archneurpsyc.1939.02270240017001

Klüver, H., & Bucy, P. C. (1939). Preliminary analysis of functions of the temporal lobes in monkeys. 1939 [classical article]. The Journal of Neuropsychiatry and Clinical Neurosciences, 9(4), 606–620. https://doi.org/10.1176/jnp.9.4.606

Klüver, H., & Bucy, P. C. (1997). Preliminary analysis of functions of the temporal lobes in monkeys. 1939. The Journal of Neuropsychiatry and Clinical Neurosciences, 9(4), 606–620. https://doi.org/10.1176/jnp.9.4.606

Koelsch, S., & Skouras, S. (2013). Functional centrality of amygdala, striatum and hypothalamus in a “small-world” network underlying joy: An fMRI study with music. Human Brain Mapping, 35(7), 3485–3498. https://doi.org/10.1002/hbm.22416

LeDoux, J. (2007). The amygdala. Current Biology, 17(20), R868–R874. https://doi.org/10.1016/j.cub.2007.08.005

LeDoux, J. E. (2000). Emotion circuits in the brain. Annual Review of Neuroscience, 23, 155–184. https://doi.org/10.1146/annurev.neuro.23.1.155

LeDoux, J., Iwata, J., Cicchetti, P., & Reis, D. (1988). Different projections of the central amygdaloid nucleus mediate autonomic and behavioral correlates of conditioned fear. The Journal of Neuroscience, 8(7), 2517–2529. https://doi.org/10.1523/JNEUROSCI.08-07-02517.1988

Lloyd, S. (1982). Least squares quantization in PCM. IEEE Transactions on Information Theory, 28(2), 129–137. https://doi.org/10.1109/TIT.1982.1056489

MacLEAN, P. D. (1949). Psychosomatic disease and the visceral brain; recent developments bearing on the Papez theory of emotion. Psychosomatic Medicine, 11(6), 338–353. https://doi.org/10.1097/00006842-194911000-00003

McDONALD, A. J. (2003). Is There an Amygdala and How Far Does It Extend? Annals of the New York Academy of Sciences, 985(1), 1–21. https://doi.org/10.1111/j.1749-6632.2003.tb07067.x

Mezer, A., Yovel, Y., Pasternak, O., Gorfine, T., & Assaf, Y. (2009). Cluster analysis of resting-state fMRI time series. NeuroImage, 45(4), 1117–1125. https://doi.org/10.1016/j.neuroimage.2008.12.015

Neugebauer, V. (2015). 15. Amygdala pain mechanisms. *Handbook of Experimental Pharmacology*, *227*, 261–284. https://doi.org/10.1007/978-3-662-46450-2_13

Notter, M. P., Gale, D., Herholz, P., Markello, R., Notter-Bielser, M.-L., & Whitaker, K. (2019). AtlasReader: A Python package to generate coordinate tables, region labels, and informative figures from statistical MRI images. Journal of Open Source Software, 4(34), 1257. https://doi.org/10.21105/joss.01257

Papez, J. W. (1995). A proposed mechanism of emotion. 1937. The Journal of Neuropsychiatry and Clinical Neurosciences, 7(1), 103–112. https://doi.org/10.1176/jnp.7.1.103

Pedregosa, F., Varoquaux, G., Gramfort, A., Michel, V., Thirion, B., Grisel, O., Blondel, M., Müller, A., Nothman, J., Louppe, G., Prettenhofer, P., Weiss, R., Dubourg, V., Vanderplas, J., Passos, A., Cournapeau, D., Brucher, M., Perrot, M., & Duchesnay, É. (2018). Scikit-learn: Machine Learning in Python (arXiv:1201.0490). arXiv. https://doi.org/10.48550/arXiv.1201.0490

Phelps, E. A., & LeDoux, J. E. (2005). Contributions of the Amygdala to Emotion Processing: From Animal Models to Human Behavior. Neuron, 48(2), 175–187. https://doi.org/10.1016/j.neuron.2005.09.025

Roy, A. K., Shehzad, Z., Margulies, D. S., Kelly, A. M. C., Uddin, L. Q., Gotimer, K., Biswal, B. B., Castellanos, F. X., & Milham, M. P. (2009). Functional connectivity of the human amygdala using resting state fMRI. NeuroImage, 45(2), 614–626. https://doi.org/10.1016/j.neuroimage.2008.11.030

Simons, L. E., Moulton, E. A., Linnman, C., Carpino, E., Becerra, L., & Borsook, D. (2014). The human amygdala and pain: Evidence from neuroimaging. *Human Brain Mapping*, *35*(2), 527–538. https://doi.org/10.1002/hbm.22199

Sladky, R., Friston, K. J., Tröstl, J., Cunnington, R., Moser, E., & Windischberger, C. (2011). Slice-timing effects and their correction in functional MRI. NeuroImage, 58(2), 588–594. https://doi.org/10.1016/j.neuroimage.2011.06.078

Swanson, L. W., & Petrovich, G. D. (1998). What is the amygdala? Trends in Neurosciences, 21(8), 323–331. https://doi.org/10.1016/S0166-2236(98)01265-X

Thirion, B., Varoquaux, G., Dohmatob, E., & Poline, J.-B. (2014). Which fMRI clustering gives good brain parcellations? Frontiers in Neuroscience, 8. https://www.frontiersin.org/articles/10.3389/fnins.2014.00167

Tillman, R. M., Stockbridge, M. D., Nacewicz, B. M., Torrisi, S., Fox, A. S., Smith, J. F., & Shackman, A. J. (2017). Intrinsic functional connectivity of the central extended amygdala. Human Brain Mapping, 39(3), 1291–1312. https://doi.org/10.1002/hbm.23917

Tyszka, J. M., & Pauli, W. M. (2016). In vivo delineation of subdivisions of the human amygdaloid complex in a high-resolution group template. Human Brain Mapping, 37(11), 3979–3998. https://doi.org/10.1002/hbm.23289

Ward, Jr. (1963). Hierarchical Grouping to Optimize an Objective Function. Journal of the American Statistical Association. https://www.tandfonline.com/doi/abs/10.1080/01621459.1963.10500845

Weera, M. M., Shackett, R. S., Kramer, H. M., Middleton, J. W., & Gilpin, N. W. (2021). Central Amygdala Projections to Lateral Hypothalamus Mediate Avoidance Behavior in Rats. *The Journal of Neuroscience: The Official Journal of the Society for Neuroscience*, *41*(1), 61–72. https://doi.org/10.1523/JNEUROSCI.0236-20.2020

Weiskrantz, L. (1956). Behavioral changes associated with ablation of the amygdaloid complex in monkeys. Journal of Comparative and Physiological Psychology, 49(4), 381–391. https://doi.org/10.1037/h0088009

Yarkoni, T., Poldrack, R. A., Nichols, T. E., Van Essen, D. C., & Wager, T. D. (2011). Large-scale automated synthesis of human functional neuroimaging data. Nature Methods, 8(8), Article 8. https://doi.org/10.1038/nmeth.1635

Yilmazer-Hanke, D. M. (2012). Chapter 22—Amygdala. In J. K. Mai & G. Paxinos (Eds.), The Human Nervous System (Third Edition) (pp. 759–834). Academic Press. https://doi.org/10.1016/B978-0-12-374236-0.10022-7

Zhang, X., Cheng, H., Zuo, Z., Zhou, K., Cong, F., Wang, B., Zhuo, Y., Chen, L., Xue, R., & Fan, Y. (2018). Individualized Functional Parcellation of the Human Amygdala Using a Semi-supervised Clustering Method: A 7T Resting State fMRI Study. Frontiers in Neuroscience, 12, 270. https://doi.org/10.3389/fnins.2018.00270

Appendix

Tables of top ten positive and negative cluster peaks identified by *atlasreader* sorted by peak value.

Kmeans left LB

cluster_id	peak_x	peak_y	peak_z	peak_value	volume_mm	juelich	harvard_oxford	aal
1	-26	-4	-28	18,760	371091	100.0% GM_Amygdala_laterobasal_group_L; 11.0% GM_Hippocampus_cornu_ammonis_L; 11.0% GM_Amygdala_superficial_group_L; 10.0% GM_Hippocampus_subiculum_L; 9.0% WM_Optic_radiation_L	37.0% Left_Amygdala; 36.0% Left_Hippocampus; 6.0% Left_Parahippocampal_Gyrus_anterior_division	ParaHippocampal_L
1	-10	-29	73	9,114	371091	43.0% GM_Primary_motor_cortex_BA4a_L; 35.0% GM_Premotor_cortex_BA6_L; 28.0% GM_Primary_somatosensory_cortex_BA3b_L; 24.0% WM_Corticospinal_tract_L; 20.0% GM_Primary_somatosensory_cortex_BA1_L; 10.0% GM_Primary_motor_cortex_BA4p_L; 5.0% GM_Superior_parietal_lobule_5L_L	44.0% Left_Precentral_Gyrus; 10.0% Left_Postcentral_Gyrus	Paracentral_Lobule_L
21	17	4	3	7,784	306	0% no_label	71.0% Right_Pallidum; 6.0% Right_Putamen	Pallidum_R
20	4	-25	60	7,192	335	82.0% GM_Primary_motor_cortex_BA4a_R; 35.0% GM_Premotor_cortex_BA6_R; 9.0% WM_Corticospinal_tract_R	73.0% Right_Precentral_Gyrus	Supp_Motor_Area_R
1	60	22	21	7,017	371091	80.0% GM_Broca's_area_BA45_R; 22.0% GM_Broca's_area_BA44_R	21.0% Right_Inferior_Frontal_Gyrus_pars_opercularis; 14.0% Right_Inferior_Frontal_Gyrus_pars_triangularis	Frontal_Inf_Tri_R
12	5	13	50	6,684	525	53.0% GM_Premotor_cortex_BA6_R	65.0% Right_Paracingulate_Gyrus; 15.0% Right_Superior_Frontal_Gyrus; 6.0% Right_Juxtapositional_Lobule_Cortex_(formerly_Supplementary_Motor_Cortex)	Supp_Motor_Area_R
13	-17	3	3	6,455	507	10.0% WM_Corticospinal_tract_L	72.0% Left_Pallidum; 9.0% Left_Putamen	Pallidum_L
14	-35	-60	13	5,910	499	75.0% WM_Optic_radiation_L; 8.0% WM_Callosal_body	0% no_label	no_label
8	-17	-48	-31	5,639	774	0% no_label	0% no_label	no_label
18	-33	-48	56	5,404	359	44.0% GM_Superior_parietal_lobule_7PC_L; 36.0% GM_Superior_parietal_lobule_7A_L; 32.0% GM_Primary_somatosensory_cortex_BA2_L; 27.0% GM_Anterior_intra-parietal_sulcus_hIP3_L; 20.0% GM_Primary_somatosensory_cortex_BA1_L; 6.0% GM_Superior_parietal_lobule_5L_L	56.0% Left_Superior_Parietal_Lobule	Parietal_Sup_L
6	-34	28	11	-7,610	1221	0% no_label	7.0% Left_Frontal_Operculum_Cortex	Frontal_Inf_Tri_L
15	-1	27	31	-7,844	488	0% no_label	44.0% Left_Paracingulate_Gyrus; 41.0% Left_Cingulate_Gyrus_anterior_division	Cingulate_Mid_L
9	1	17	-3	-7,906	769	26.0% WM_Callosal_body	67.0% Right_Subcallosal_Cortex; 8.0% Left_Subcallosal_Cortex	Olfactory_R
19	19	2	23	-7,928	336	15.0% WM_Superior_occipito-frontal_fascicle_R	30.0% Right_Caudate	Caudate_R
2	-7	-80	54	-8,311	15370	83.0% GM_Superior_parietal_lobule_7P_L; 24.0% GM_Superior_parietal_lobule_7A_L; 6.0% GM_Superior_parietal_lobule_7M_L	24.0% Left_Lateral_Occipital_Cortex_superior_division; 12.0% Left_Precuneous_Cortex	Precuneus_L
16	12	-8	15	-8,513	469	0% no_label	86.0% Right_Thalamus	Thalamus_R
5	-3	22	9	-9,037	2766	67.0% WM_Callosal_body	28.0% Left_Lateral_Ventrical	no_label
25	-10	-5	12	-9,274	237	0% no_label	90.0% Left_Thalamus	no_label
4	-1	-5	5	-11,226	2782	0% no_label	67.0% Left_Thalamus	no_label
3	-19	-4	-13	-12,758	7649	80.0% GM_Amygdala_superficial_group_L; 35.0% GM_Amygdala_centromedial_group_L; 27.0% GM_Amygdala_laterobasal_group_L	74.0% Left_Amygdala	Amygdala_L

Kmeans left CM

cluster_id	peak_x	peak_y	peak_z	peak_value	volume_mm	juelich	harvard_oxford	aal
2	-25	1	-16	16,824	41843	26.0% GM_Amygdala_superficial_group_L	47.0% Left_Amygdala; 5.0% Left_Parahippocampal_Gyrus_anterior_division	Amygdala_L
8	0	13	39	7,945	2824	0% no_label	38.0% Left_Cingulate_Gyrus_anterior_division; 19.0% Left_Paracingulate_Gyrus; 5.0% Right_Cingulate_Gyrus_anterior_division	Cingulate_Mid_L
28	-18	15	18	7,218	229	20.0% WM_Superior_occipito-frontal_fascicle_L	10.0% Left_Caudate	Caudate_L
18	-4	-25	-33	6,099	363	0% no_label	100.0% Brain-Stem	no_label
14	-33	-56	-34	5,784	596	0% no_label	0% no_label	Cerebelum_Crus1_L
24	-53	-8	-35	5,554	278	0% no_label	55.0% Left_Inferior_Temporal_Gyrus_anterior_division; 18.0% Left_Inferior_Temporal_Gyrus_posterior_division; 8.0% Left_Middle_Temporal_Gyrus_posterior_division	Temporal_Inf_L
27	-4	-4	21	5,433	235	24.0% WM_Callosal_body	77.0% Left_Lateral_Ventrical	no_label
2	10	-94	-17	5,351	41843	0% no_label	15.0% Right_Occipital_Pole; 5.0% Right_Lingual_Gyrus	no_label
30	-8	37	51	5,245	217	0% no_label	41.0% Left_Superior_Frontal_Gyrus; 16.0% Left_Frontal_Pole	Frontal_Sup_Medial_L
29	20	17	14	5,235	227	19.0% WM_Superior_occipito-frontal_fascicle_R	31.0% Right_Caudate	Caudate_R
21	-10	-27	-3	-6,547	319	0% no_label	36.0% Left_Thalamus; 8.0% Brain-Stem	no_label
13	-11	-23	37	-6,820	674	0% no_label	37.0% Left_Cingulate_Gyrus_posterior_division	Cingulate_Mid_L
10	18	-35	11	-7,069	1735	75.0% GM_Hippocampus_cornu_ammonis_R; 73.0% WM_Fornix; 24.0% GM_Hippocampus_dentate_gyrus_R; 18.0% WM_Callosal_body	32.0% Right_Lateral_Ventricle	no_label
3	43	-45	-21	-7,668	25159	0% no_label	56.0% Right_Temporal_Occipital_Fusiform_Cortex; 14.0% Right_Inferior_Temporal_Gyrus_temporooccipital_part	Fusiform_R
1	-38	-32	38	-7,904	48656	28.0% GM_Inferior_parietal_lobule_PFt_L; 21.0% GM_Anterior_intra-parietal_sulcus_hIP2_L; 11.0% GM_Anterior_intra-parietal_sulcus_hIP3_L; 10.0% GM_Superior_parietal_lobule_7PC_L	21.0% Left_Supramarginal_Gyrus_anterior_division; 17.0% Left_Postcentral_Gyrus	Parietal_Inf_L
6	9	-4	-8	-9,271	3520	0% no_label	0% no_label	no_label
5	-4	11	9	-9,555	3617	0% no_label	96.0% Left_Lateral_Ventrical	Caudate_L
7	22	-4	-17	-9,633	3501	74.0% GM_Amygdala_superficial_group_R; 54.0% GM_Amygdala_laterobasal_group_R; 10.0% GM_Amygdala_centromedial_group_R; 8.0% GM_Hippocampus_subiculum_R	99.0% Right_Amygdala	Amygdala_R
9	-4	-23	-9	-9,904	2315	0% no_label	0% no_label	no_label
4	-22	0	-24	-12,861	6715	32.0% GM_Amygdala_laterobasal_group_L; 16.0% GM_Amygdala_superficial_group_L; 8.0% GM_Hippocampus_entorhinal_cortex_L	64.0% Left_Amygdala; 26.0% Left_Parahippocampal_Gyrus_anterior_division	Amygdala_L

Kmeans left SF

cluster_id	peak_x	peak_y	peak_z	peak_value	volume_mm	juelich	harvard_oxford	aal
3	-19	1	-23	20,249	19152	29.0% GM_Amygdala_laterobasal_group_L; 17.0% GM_Amygdala_superficial_group_L; 10.0% GM_Hippocampus_entorhinal_cortex_L	41.0% Left_Parahippocampal_Gyrus_anterior_division; 33.0% Left_Amygdala; 6.0% Left_Temporal_Pole	ParaHippocampal_L
5	-4	22	8	12,740	4681	26.0% WM_Callosal_body	40.0% Left_Lateral_Ventrical	no_label
2	46	-47	-22	11,453	116241	0% no_label	58.0% Right_Temporal_Occipital_Fusiform_Cortex; 33.0% Right_Inferior_Temporal_Gyrus_temporooccipital_part	Temporal_Inf_R
7	-5	-24	-14	11,073	2360	0% no_label	17.0% Brain-Stem	no_label
2	-55	-59	45	8,897	116241	5.0% GM_Inferior_parietal_lobule_PFm_L	25.0% Left_Lateral_Occipital_Cortex_superior_division; 20.0% Left_Angular_Gyrus; 7.0% Left_Supramarginal_Gyrus_posterior_division	no_label
12	35	-40	58	7,023	702	77.0% GM_Primary_somatosensory_cortex_BA2_R; 32.0% GM_Superior_parietal_lobule_7PC_R; 20.0% GM_Primary_somatosensory_cortex_BA1_R; 20.0% GM_Anterior_intra-parietal_sulcus_hIP3_R; 9.0% GM_Primary_somatosensory_cortex_BA3b_R	49.0% Right_Superior_Parietal_Lobule; 22.0% Right_Postcentral_Gyrus	Postcentral_R
24	-26	-18	62	7,019	248	74.0% GM_Premotor_cortex_BA6_L; 22.0% WM_Corticospinal_tract_L; 10.0% GM_Primary_motor_cortex_BA4a_L	37.0% Left_Precentral_Gyrus	Precentral_L
19	36	31	6	6,676	354	10.0% GM_Broca's_area_BA45_R	9.0% Right_Inferior_Frontal_Gyrus_pars_triangularis; 8.0% Right_Frontal_Operculum_Cortex; 7.0% Right_Frontal_Orbital_Cortex	Insula_R
13	21	-27	-13	6,455	683	97.0% GM_Hippocampus_subiculum_R; 10.0% GM_Lateral_geniculate_body_R	41.0% Right_Parahippocampal_Gyrus_posterior_division; 13.0% Right_Hippocampus	no_label
18	-37	-40	45	6,452	358	41.0% GM_Anterior_intra-parietal_sulcus_hIP3_L; 11.0% GM_Primary_somatosensory_cortex_BA2_L; 10.0% GM_Superior_parietal_lobule_7PC_L; 5.0% GM_Superior_parietal_lobule_5L_L	28.0% Left_Superior_Parietal_Lobule; 24.0% Left_Postcentral_Gyrus; 10.0% Left_Supramarginal_Gyrus_posterior_division	Parietal_Inf_L
14	18	-48	46	-5,217	543	10.0% GM_Superior_parietal_lobule_5M_R; 10.0% GM_Superior_parietal_lobule_5L_R	6.0% Right_Precuneous_Cortex	no_label
11	47	-39	36	-6,263	716	28.0% GM_Anterior_intra-parietal_sulcus_hIP2_R; 13.0% GM_Anterior_intra-parietal_sulcus_hIP1_R; 10.0% GM_Inferior_parietal_lobule_PF_R	24.0% Right_Supramarginal_Gyrus_posterior_division	SupraMarginal_R
1	31	-81	-33	-6,300	462400	0% no_label	0% no_label	Cerebelum_Crus1_R
9	-21	-23	70	-7,026	1471	28.0% GM_Primary_motor_cortex_BA4a_L; 9.0% WM_Corticospinal_tract_L	46.0% Left_Precentral_Gyrus; 6.0% Left_Postcentral_Gyrus	Precentral_L
20	2	-25	59	-7,174	351	79.0% GM_Primary_motor_cortex_BA4a_R; 26.0% GM_Premotor_cortex_BA6_R; 9.0% GM_Primary_motor_cortex_BA4p_R	52.0% Right_Precentral_Gyrus	Supp_Motor_Area_R
6	-27	-33	67	-7,518	3936	30.0% GM_Primary_somatosensory_cortex_BA3b_L; 28.0% GM_Primary_somatosensory_cortex_BA1_L; 24.0% GM_Primary_motor_cortex_BA4a_L; 20.0% GM_Primary_somatosensory_cortex_BA2_L; 20.0% GM_Primary_motor_cortex_BA4p_L; 18.0% WM_Corticospinal_tract_L; 17.0% GM_Premotor_cortex_BA6_L	60.0% Left_Postcentral_Gyrus; 12.0% Left_Precentral_Gyrus	Postcentral_L
4	35	-33	58	-8,063	4983	87.0% GM_Primary_somatosensory_cortex_BA3b_R; 42.0% GM_Primary_motor_cortex_BA4p_R; 22.0% GM_Primary_motor_cortex_BA4a_R; 8.0% GM_Premotor_cortex_BA6_R; 8.0% GM_Primary_somatosensory_cortex_BA1_R; 6.0% GM_Primary_somatosensory_cortex_BA3a_R	53.0% Right_Postcentral_Gyrus; 5.0% Right_Superior_Parietal_Lobule	Postcentral_R
8	38	-21	66	-9,815	2319	99.0% GM_Premotor_cortex_BA6_R; 10.0% GM_Primary_motor_cortex_BA4a_R; 8.0% WM_Corticospinal_tract_R	55.0% Right_Precentral_Gyrus; 11.0% Right_Postcentral_Gyrus	Precentral_R
1	49	-9	52	-10,887	462400	67.0% GM_Premotor_cortex_BA6_R; 34.0% GM_Primary_somatosensory_cortex_BA1_R; 13.0% GM_Primary_somatosensory_cortex_BA3b_R; 9.0% WM_Corticospinal_tract_R; 8.0% GM_Primary_motor_cortex_BA4a_R	65.0% Right_Precentral_Gyrus; 13.0% Right_Postcentral_Gyrus	Frontal_Mid_2_R
1	-30	0	-16	-17,251	462400	23.0% GM_Amygdala_superficial_group_L; 9.0% WM_Uncinate_fascicle_L	62.0% Left_Amygdala	no_label

Kmeans right LB

cluster_id	peak_x	peak_y	peak_z	peak_value	volume_mm	juelich	harvard_oxford	aal
3	28	0	-26	18,146	35336	83.0% GM_Amygdala_laterobasal_group_R	78.0% Right_Amygdala; 7.0% Right_Parahippocampal_Gyrus_anterior_division	Amygdala_R
4	-28	-6	-27	12,081	29478	88.0% GM_Amygdala_laterobasal_group_L; 21.0% GM_Hippocampus_cornu_ammonis_L; 19.0% GM_Hippocampus_subiculum_L; 10.0% GM_Amygdala_superficial_group_L; 9.0% WM_Optic_radiation_L	54.0% Left_Hippocampus; 21.0% Left_Amygdala; 6.0% Left_Parahippocampal_Gyrus_anterior_division	ParaHippocampal_L
2	7	33	9	8,485	91287	53.0% WM_Callosal_body	40.0% Right_Cingulate_Gyrus_anterior_division	no_label
5	6	20	5	8,018	6979	24.0% WM_Callosal_body	81.0% Right_Lateral_Ventricle	no_label
20	-30	-53	3	6,753	368	0% no_label	69.0% Left_Lateral_Ventrical; 6.0% Left_Lingual_Gyrus	no_label
12	2	-16	-6	6,586	647	0% no_label	0% no_label	no_label
9	52	-21	42	6,238	980	60.0% GM_Primary_somatosensory_cortex_BA2_R; 36.0% GM_Inferior_parietal_lobule_PFt_R; 20.0% GM_Primary_somatosensory_cortex_BA1_R; 10.0% GM_Inferior_parietal_lobule_PFop_R; 8.0% GM_Primary_somatosensory_cortex_BA3b_R	52.0% Right_Postcentral_Gyrus; 14.0% Right_Supramarginal_Gyrus_anterior_division	Postcentral_R
26	61	-12	29	6,238	295	40.0% GM_Primary_somatosensory_cortex_BA3b_R; 22.0% GM_Primary_somatosensory_cortex_BA2_R; 12.0% GM_Secondary_somatosensory_cortex_/_Parietal_operculum_OP4_R; 11.0% GM_Inferior_parietal_lobule_PFop_R; 10.0% GM_Primary_somatosensory_cortex_BA1_R; 10.0% GM_Inferior_parietal_lobule_PFt_R	50.0% Right_Postcentral_Gyrus	Postcentral_R
24	-52	-9	48	5,611	322	72.0% GM_Premotor_cortex_BA6_L; 26.0% GM_Primary_somatosensory_cortex_BA1_L; 23.0% GM_Primary_motor_cortex_BA4a_L; 10.0% GM_Primary_somatosensory_cortex_BA3b_L; 10.0% GM_Primary_motor_cortex_BA4p_L	67.0% Left_Precentral_Gyrus; 10.0% Left_Postcentral_Gyrus	Postcentral_L
16	39	18	-37	5,589	434	0% no_label	69.0% Right_Temporal_Pole	Temporal_Pole_Mid_R
31	-41	25	-27	-6,354	213	0% no_label	39.0% Left_Temporal_Pole	Temporal_Pole_Sup_L
33	28	-6	14	-6,574	207	7.0% GM_Secondary_somatosensory_cortex_/_Parietal_operculum_OP3_R; 5.0% WM_Corticospinal_tract_R	48.0% Right_Putamen	Putamen_R
13	-46	-15	50	-6,644	616	44.0% GM_Primary_motor_cortex_BA4a_L; 31.0% GM_Premotor_cortex_BA6_L; 30.0% GM_Primary_somatosensory_cortex_BA3b_L; 30.0% GM_Primary_somatosensory_cortex_BA1_L; 9.0% WM_Corticospinal_tract_L; 5.0% GM_Primary_motor_cortex_BA4p_L	37.0% Left_Precentral_Gyrus; 33.0% Left_Postcentral_Gyrus	Postcentral_L
8	4	22	9	-6,760	1042	73.0% WM_Callosal_body	24.0% Right_Lateral_Ventricle	no_label
14	-27	41	-11	-6,977	583	0% no_label	63.0% Left_Frontal_Pole; 7.0% Left_Frontal_Orbital_Cortex	Frontal_Mid_2_L
10	52	-36	29	-7,084	791	26.0% GM_Inferior_parietal_lobule_PFcm_R; 20.0% GM_Inferior_parietal_lobule_PFm_R; 10.0% GM_Anterior_intra-parietal_sulcus_hIP2_R; 9.0% GM_Inferior_parietal_lobule_PF_R	24.0% Right_Supramarginal_Gyrus_posterior_division; 18.0% Right_Parietal_Operculum_Cortex; 12.0% Right_Planum_Temporale	SupraMarginal_R
6	35	26	10	-8,045	1739	0% no_label	30.0% Right_Frontal_Operculum_Cortex; 17.0% Right_Inferior_Frontal_Gyrus_pars_triangularis	Frontal_Inf_Tri_R
1	-9	-81	53	-8,617	102475	48.0% GM_Superior_parietal_lobule_7P_L; 24.0% GM_Superior_parietal_lobule_7A_L	25.0% Left_Lateral_Occipital_Cortex_superior_division; 5.0% Left_Precuneous_Cortex	Parietal_Sup_L
7	0	24	32	-9,719	1275	0% no_label	40.0% Left_Cingulate_Gyrus_anterior_division; 23.0% Left_Paracingulate_Gyrus; 10.0% Right_Cingulate_Gyrus_anterior_division; 6.0% Right_Paracingulate_Gyrus	Cingulate_Mid_L
1	26	-1	-14	-14,106	102475	76.0% GM_Amygdala_superficial_group_R; 44.0% GM_Amygdala_laterobasal_group_R	72.0% Right_Amygdala	Amygdala_R

Kmeans right CM

cluster_id	peak_x	peak_y	peak_z	peak_value	volume_mm	juelich	harvard_oxford	aal
1	25	2	-15	19,672	77795	40.0% GM_Amygdala_superficial_group_R	48.0% Right_Amygdala	Amygdala_R
2	2	25	38	8,940	15391	0% no_label	56.0% Right_Paracingulate_Gyrus; 19.0% Right_Cingulate_Gyrus_anterior_division	Frontal_Sup_Medial_L
14	0	-24	28	7,661	727	14.0% WM_Callosal_body	53.0% Left_Cingulate_Gyrus_posterior_division; 9.0% Right_Cingulate_Gyrus_posterior_division	no_label
9	-61	5	1	7,563	2131	10.0% GM_Broca's_area_BA44_L; 8.0% GM_Secondary_somatosensory_cortex_/_Parietal_operculum_OP4_L	15.0% Left_Precentral_Gyrus; 7.0% Left_Temporal_Pole	no_label
10	36	2	61	7,365	998	0% no_label	50.0% Right_Middle_Frontal_Gyrus; 9.0% Right_Precentral_Gyrus	Frontal_Mid_2_R
3	-38	59	19	7,038	9434	0% no_label	6.0% Left_Frontal_Pole	no_label
4	26	50	22	6,833	8165	0% no_label	76.0% Right_Frontal_Pole	Frontal_Sup_2_R
16	-54	11	45	6,213	536	0% no_label	11.0% Left_Middle_Frontal_Gyrus	Precentral_L
19	5	-30	-31	5,980	430	0% no_label	100.0% Brain-Stem	no_label
22	-13	24	-16	5,827	341	0% no_label	34.0% Left_Subcallosal_Cortex; 32.0% Left_Frontal_Orbital_Cortex	Rectus_L
25	52	-68	39	-5,479	306	94.0% GM_Inferior_parietal_lobule_PGp_R	50.0% Right_Lateral_Occipital_Cortex_superior_division	Angular_R
23	-19	-88	1	-5,599	318	42.0% WM_Optic_radiation_L; 18.0% GM_Visual_cortex_V3V_L; 15.0% WM_Callosal_body; 10.0% GM_Visual_cortex_V4_L; 10.0% GM_Visual_cortex_V2_BA18_L; 10.0% GM_Visual_cortex_V1_BA17_L	0% no_label	no_label
21	25	-72	16	-5,678	360	36.0% WM_Optic_radiation_R; 23.0% WM_Callosal_body	0% no_label	no_label
17	24	-31	-22	-5,905	507	0% no_label	61.0% Right_Parahippocampal_Gyrus_posterior_division; 20.0% Right_Temporal_Fusiform_Cortex_posterior_division; 6.0% Right_Temporal_Occipital_Fusiform_Cortex	Fusiform_R
13	44	-45	-21	-6,812	742	0% no_label	55.0% Right_Temporal_Occipital_Fusiform_Cortex; 21.0% Right_Inferior_Temporal_Gyrus_temporooccipital_part	Temporal_Inf_R
20	-5	-24	-14	-7,045	427	0% no_label	17.0% Brain-Stem	no_label
8	4	20	5	-7,673	2862	27.0% WM_Callosal_body	63.0% Right_Lateral_Ventricle	no_label
7	9	-3	-8	-9,218	3084	0% no_label	0% no_label	no_label
6	-20	-5	-18	-11,946	4157	86.0% GM_Amygdala_laterobasal_group_L; 79.0% GM_Amygdala_superficial_group_L; 18.0% GM_Amygdala_centromedial_group_L	98.0% Left_Amygdala	Amygdala_L
5	22	-5	-17	-13,643	4746	66.0% GM_Amygdala_superficial_group_R; 59.0% GM_Amygdala_laterobasal_group_R; 10.0% GM_Hippocampus_subiculum_R; 10.0% GM_Amygdala_centromedial_group_R	97.0% Right_Amygdala	Amygdala_R

Kmeans right SF

cluster_id	peak_x	peak_y	peak_z	peak_value	volume_mm	juelich	harvard_oxford	aal
3	21	-2	-18	20,156	20880	70.0% GM_Amygdala_superficial_group_R; 16.0% GM_Amygdala_laterobasal_group_R; 13.0% GM_Hippocampus_entorhinal_cortex_R; 9.0% GM_Amygdala_centromedial_group_R	95.0% Right_Amygdala	Amygdala_R
5	-3	22	8	13,686	5574	36.0% WM_Callosal_body	30.0% Left_Lateral_Ventrical	no_label
32	-1	-6	5	12,038	348	0% no_label	78.0% Left_Thalamus	no_label
2	53	-68	40	11,486	164225	0% no_label	25.0% Right_Lateral_Occipital_Cortex_superior_division	Angular_R
7	4	-24	-13	11,246	3017	0% no_label	15.0% Brain-Stem	no_label
2	-39	-3	19	9,920	164225	0% no_label	31.0% Left_Central_Opercular_Cortex	no_label
13	26	-23	-16	9,392	1544	100.0% GM_Hippocampus_subiculum_R; 18.0% GM_Hippocampus_dentate_gyrus_R; 17.0% GM_Hippocampus_cornu_ammonis_R; 8.0% WM_Fornix; 7.0% GM_Lateral_geniculate_body_R	73.0% Right_Hippocampus	ParaHippocampal_R
6	-53	-12	54	8,840	5258	0% no_label	25.0% Left_Postcentral_Gyrus; 23.0% Left_Precentral_Gyrus	Postcentral_L
17	-34	40	-9	7,988	782	0% no_label	47.0% Left_Frontal_Pole; 7.0% Left_Frontal_Orbital_Cortex	Frontal_Mid_2_L
18	-23	-25	-15	7,892	741	92.0% GM_Hippocampus_subiculum_L; 19.0% GM_Lateral_geniculate_body_L; 10.0% WM_Fornix	65.0% Left_Hippocampus; 8.0% Left_Parahippocampal_Gyrus_posterior_division	no_label
30	-16	-34	18	-6,521	354	0% no_label	90.0% Left_Lateral_Ventrical	no_label
4	22	-83	-31	-6,668	7225	0% no_label	0% no_label	Cerebelum_Crus1_R
16	6	-39	60	-7,256	821	70.0% GM_Superior_parietal_lobule_5M_R; 40.0% WM_Corticospinal_tract_R; 35.0% GM_Primary_motor_cortex_BA4a_R; 9.0% GM_Superior_parietal_lobule_5Ci_R; 5.0% GM_Primary_somatosensory_cortex_BA3b_R	45.0% Right_Postcentral_Gyrus; 14.0% Right_Precuneous_Cortex	Paracentral_Lobule_R
14	-4	-45	-12	-7,441	1301	0% no_label	0% no_label	Cerebelum_4_5_L
12	47	-38	36	-7,942	1835	18.0% GM_Anterior_intra-parietal_sulcus_hIP2_R; 18.0% GM_Anterior_intra-parietal_sulcus_hIP1_R; 8.0% GM_Inferior_parietal_lobule_PFcm_R; 5.0% GM_Anterior_intra-parietal_sulcus_hIP3_R	22.0% Right_Supramarginal_Gyrus_posterior_division	no_label
28	0	-27	1	-7,998	379	0% no_label	0% no_label	no_label
8	32	-34	59	-9,129	2913	68.0% GM_Primary_somatosensory_cortex_BA3b_R; 50.0% GM_Primary_motor_cortex_BA4p_R; 24.0% GM_Primary_motor_cortex_BA4a_R; 14.0% GM_Primary_somatosensory_cortex_BA2_R; 10.0% GM_Primary_somatosensory_cortex_BA1_R	42.0% Right_Postcentral_Gyrus; 5.0% Right_Supramarginal_Gyrus_anterior_division; 5.0% Right_Superior_Parietal_Lobule	Postcentral_R
9	-35	-34	67	-9,544	2734	83.0% GM_Primary_somatosensory_cortex_BA1_L; 31.0% GM_Primary_motor_cortex_BA4a_L; 28.0% GM_Primary_somatosensory_cortex_BA2_L; 18.0% GM_Primary_somatosensory_cortex_BA3b_L; 10.0% GM_Superior_parietal_lobule_7PC_L; 10.0% GM_Superior_parietal_lobule_5L_L; 10.0% GM_Primary_motor_cortex_BA4p_L	64.0% Left_Postcentral_Gyrus	Postcentral_L
1	-51	-9	48	-9,776	397055	74.0% GM_Premotor_cortex_BA6_L; 25.0% GM_Primary_motor_cortex_BA4a_L; 22.0% GM_Primary_somatosensory_cortex_BA1_L; 10.0% GM_Primary_somatosensory_cortex_BA3b_L; 8.0% GM_Primary_motor_cortex_BA4p_L	61.0% Left_Precentral_Gyrus; 8.0% Left_Postcentral_Gyrus	Postcentral_L
1	25	8	-21	-16,010	397055	6.0% GM_Hippocampus_entorhinal_cortex_R	36.0% Right_Frontal_Orbital_Cortex	Temporal_Pole_Sup_R

Hierarchical left LB

cluster_id	peak_x	peak_y	peak_z	peak_value	volume_mm	juelich	harvard_oxford	aal
3	-26	-4	-27	19,093	52684	100.0% GM_Amygdala_laterobasal_group_L; 19.0% GM_Hippocampus_cornu_ammonis_L; 13.0% GM_Amygdala_superficial_group_L; 10.0% GM_Hippocampus_subiculum_L; 5.0% WM_Optic_radiation_L	48.0% Left_Amygdala; 37.0% Left_Hippocampus; 5.0% Left_Parahippocampal_Gyrus_anterior_division	ParaHippocampal_L
4	27	-6	-27	12,429	35351	90.0% GM_Amygdala_laterobasal_group_R; 60.0% GM_Hippocampus_subiculum_R; 48.0% GM_Hippocampus_cornu_ammonis_R; 11.0% GM_Hippocampus_dentate_gyrus_R; 10.0% GM_Hippocampus_entorhinal_cortex_R; 8.0% GM_Amygdala_superficial_group_R	69.0% Right_Hippocampus; 12.0% Right_Amygdala	no_label
1	25	53	-5	9,534	99702	0% no_label	41.0% Right_Frontal_Pole	Frontal_Sup_2_R
5	28	-22	71	7,958	20756	89.0% GM_Premotor_cortex_BA6_R; 27.0% WM_Corticospinal_tract_R; 24.0% GM_Primary_motor_cortex_BA4a_R; 8.0% GM_Primary_motor_cortex_BA4p_R	50.0% Right_Precentral_Gyrus; 12.0% Right_Postcentral_Gyrus	Precentral_R
33	3	6	-6	7,154	236	0% no_label	0% no_label	no_label
7	56	-19	45	6,809	1935	60.0% GM_Primary_somatosensory_cortex_BA2_R; 43.0% GM_Primary_somatosensory_cortex_BA1_R; 10.0% GM_Inferior_parietal_lobule_PFt_R; 10.0% GM_Inferior_parietal_lobule_PFop_R	55.0% Right_Postcentral_Gyrus; 15.0% Right_Supramarginal_Gyrus_anterior_division	Postcentral_R
1	-55	-4	40	6,806	99702	70.0% GM_Premotor_cortex_BA6_L; 22.0% GM_Primary_motor_cortex_BA4a_L; 12.0% GM_Primary_somatosensory_cortex_BA1_L; 7.0% GM_Primary_somatosensory_cortex_BA3b_L	79.0% Left_Precentral_Gyrus; 6.0% Left_Postcentral_Gyrus	Postcentral_L
12	2	-15	-6	6,546	1025	0% no_label	0% no_label	no_label
13	26	-18	6	6,349	841	68.0% WM_Corticospinal_tract_R	8.0% Right_Putamen; 5.0% Right_Pallidum	no_label
11	-10	18	-14	6,218	1105	7.0% WM_Callosal_body	34.0% Left_Subcallosal_Cortex	Rectus_L
27	-40	24	-26	-6,466	335	0% no_label	46.0% Left_Temporal_Pole; 7.0% Left_Frontal_Orbital_Cortex	Temporal_Pole_Sup_L
32	28	-3	14	-6,539	239	8.0% WM_Corticospinal_tract_R	49.0% Right_Putamen	Putamen_R
18	52	-35	27	-6,694	588	57.0% GM_Inferior_parietal_lobule_PFcm_R; 10.0% GM_Anterior_intra-parietal_sulcus_hIP2_R	32.0% Right_Parietal_Operculum_Cortex; 17.0% Right_Planum_Temporale; 14.0% Right_Supramarginal_Gyrus_posterior_division	SupraMarginal_R
20	46	23	-24	-7,013	489	0% no_label	60.0% Right_Temporal_Pole	Temporal_Pole_Sup_R
19	-28	42	-11	-7,405	517	0% no_label	68.0% Left_Frontal_Pole	Frontal_Mid_2_L
8	35	26	10	-7,781	1573	0% no_label	30.0% Right_Frontal_Operculum_Cortex; 17.0% Right_Inferior_Frontal_Gyrus_pars_triangularis	Frontal_Inf_Tri_R
6	-34	29	10	-8,897	2193	0% no_label	9.0% Left_Frontal_Operculum_Cortex	Frontal_Inf_Tri_L
10	-1	27	31	-9,177	1141	0% no_label	44.0% Left_Paracingulate_Gyrus; 41.0% Left_Cingulate_Gyrus_anterior_division	Cingulate_Mid_L
2	-6	-79	54	-9,586	79165	84.0% GM_Superior_parietal_lobule_7P_L; 23.0% GM_Superior_parietal_lobule_7A_L; 12.0% GM_Superior_parietal_lobule_7M_L	24.0% Left_Lateral_Occipital_Cortex_superior_division; 23.0% Left_Precuneous_Cortex	Precuneus_L
2	-25	-1	-16	-15,559	79165	56.0% GM_Amygdala_superficial_group_L; 12.0% GM_Amygdala_laterobasal_group_L; 10.0% GM_Amygdala_centromedial_group_L	79.0% Left_Amygdala	Amygdala_L

Hierarchical left CM

cluster_id	peak_x	peak_y	peak_z	peak_value	volume_mm	juelich	harvard_oxford	aal
1	-25	1	-15	22,345	68739	34.0% GM_Amygdala_superficial_group_L	40.0% Left_Amygdala	Amygdala_L
2	-2	-62	1	8,480	18158	0% no_label	27.0% Left_Lingual_Gyrus	Vermis_4_5
3	1	15	42	8,119	17678	0% no_label	33.0% Right_Paracingulate_Gyrus; 15.0% Left_Paracingulate_Gyrus; 12.0% Right_Cingulate_Gyrus_anterior_division; 5.0% Left_Cingulate_Gyrus_anterior_division	Frontal_Sup_Medial_L
18	-13	-43	-5	7,418	372	15.0% GM_Hippocampus_subiculum_L	49.0% Left_Lingual_Gyrus; 15.0% Left_Parahippocampal_Gyrus_posterior_division; 11.0% Left_Cingulate_Gyrus_posterior_division	Lingual_L
15	-50	-14	44	7,387	546	62.0% GM_Primary_somatosensory_cortex_BA3b_L; 46.0% GM_Primary_somatosensory_cortex_BA1_L; 38.0% GM_Primary_somatosensory_cortex_BA2_L; 30.0% GM_Primary_motor_cortex_BA4a_L; 9.0% GM_Primary_motor_cortex_BA4p_L; 8.0% WM_Corticospinal_tract_L; 5.0% GM_Premotor_cortex_BA6_L	39.0% Left_Precentral_Gyrus; 34.0% Left_Postcentral_Gyrus	Postcentral_L
4	26	50	23	7,158	3382	0% no_label	80.0% Right_Frontal_Pole	Frontal_Sup_2_R
6	54	-8	53	6,693	2478	80.0% GM_Premotor_cortex_BA6_R; 26.0% GM_Primary_somatosensory_cortex_BA1_R; 10.0% GM_Primary_somatosensory_cortex_BA3b_R	26.0% Right_Precentral_Gyrus; 11.0% Right_Postcentral_Gyrus	Frontal_Mid_2_R
20	0	-80	33	6,564	361	21.0% GM_Visual_cortex_V2_BA18_R; 21.0% GM_Superior_parietal_lobule_7M_R; 10.0% GM_Superior_parietal_lobule_7P_R	48.0% Left_Cuneal_Cortex; 16.0% Left_Precuneous_Cortex; 11.0% Right_Cuneal_Cortex	Cuneus_L
12	-3	-100	14	6,558	823	67.0% GM_Visual_cortex_V1_BA17_L; 41.0% GM_Visual_cortex_V2_BA18_L	45.0% Left_Occipital_Pole	Cuneus_L
14	-6	-30	-32	6,422	640	0% no_label	100.0% Brain-Stem	no_label
17	-29	-41	6	-6,421	501	16.0% WM_Callosal_body; 6.0% GM_Hippocampus_cornu_ammonis_L	37.0% Left_Lateral_Ventrical	no_label
11	-38	18	-25	-7,252	883	0% no_label	69.0% Left_Temporal_Pole; 13.0% Left_Frontal_Orbital_Cortex	Temporal_Pole_Sup_L
9	-22	-13	-8	-8,108	2252	30.0% GM_Hippocampus_hippocampal-amygdaloid_transition_area_L; 26.0% GM_Amygdala_centromedial_group_L; 24.0% GM_Hippocampus_cornu_ammonis_L; 19.0% GM_Hippocampus_dentate_gyrus_L; 15.0% GM_Amygdala_superficial_group_L; 10.0% WM_Corticospinal_tract_L; 6.0% WM_Optic_radiation_L	12.0% Left_Pallidum	no_label
8	6	14	15	-8,515	2369	54.0% WM_Callosal_body	74.0% Right_Lateral_Ventricle	no_label
10	22	-4	-17	-9,309	1573	74.0% GM_Amygdala_superficial_group_R; 54.0% GM_Amygdala_laterobasal_group_R; 10.0% GM_Amygdala_centromedial_group_R; 8.0% GM_Hippocampus_subiculum_R	99.0% Right_Amygdala	Amygdala_R
5	-22	0	-24	-13,021	3340	32.0% GM_Amygdala_laterobasal_group_L; 16.0% GM_Amygdala_superficial_group_L; 8.0% GM_Hippocampus_entorhinal_cortex_L	64.0% Left_Amygdala; 26.0% Left_Parahippocampal_Gyrus_anterior_division	Amygdala_L

Hierarchical left SF

cluster_id	peak_x	peak_y	peak_z	peak_value	volume_mm	juelich	harvard_oxford	aal
3	-20	2	-23	19,854	17073	23.0% GM_Amygdala_laterobasal_group_L; 12.0% GM_Amygdala_superficial_group_L; 10.0% GM_Hippocampus_entorhinal_cortex_L	39.0% Left_Parahippocampal_Gyrus_anterior_division; 26.0% Left_Amygdala; 13.0% Left_Temporal_Pole	ParaHippocampal_L
5	-4	22	8	13,781	5721	26.0% WM_Callosal_body	40.0% Left_Lateral_Ventrical	no_label
23	-1	-6	5	11,453	359	0% no_label	78.0% Left_Thalamus	no_label
9	5	-24	-14	10,295	1190	0% no_label	17.0% Brain-Stem	no_label
7	-6	-20	-20	10,259	1394	0% no_label	61.0% Brain-Stem	no_label
12	49	-50	-23	9,840	887	0% no_label	53.0% Right_Inferior_Temporal_Gyrus_temporooccipital_part; 31.0% Right_Temporal_Occipital_Fusiform_Cortex	Temporal_Inf_R
2	48	-73	41	8,917	31625	61.0% GM_Inferior_parietal_lobule_PGp_R	35.0% Right_Lateral_Occipital_Cortex_superior_division	Angular_R
8	-47	-45	-24	7,889	1382	0% no_label	28.0% Left_Inferior_Temporal_Gyrus_temporooccipital_part; 22.0% Left_Temporal_Fusiform_Cortex_posterior_division; 20.0% Left_Inferior_Temporal_Gyrus_posterior_division; 14.0% Left_Temporal_Occipital_Fusiform_Cortex	Temporal_Inf_L
17	-27	42	-11	7,328	472	0% no_label	66.0% Left_Frontal_Pole	Frontal_Sup_2_L
2	-54	-65	40	7,089	31625	0% no_label	42.0% Left_Lateral_Occipital_Cortex_superior_division	no_label
29	57	-28	32	-5,573	253	41.0% GM_Inferior_parietal_lobule_PFcm_R; 36.0% GM_Inferior_parietal_lobule_PF_R; 27.0% GM_Inferior_parietal_lobule_PFop_R; 20.0% GM_Secondary_somatosensory_cortex_/_Parietal_operculum_OP1_R; 20.0% GM_Inferior_parietal_lobule_PFt_R; 10.0% GM_Anterior_intra-parietal_sulcus_hIP2_R	37.0% Right_Supramarginal_Gyrus_anterior_division; 17.0% Right_Parietal_Operculum_Cortex	SupraMarginal_R
20	-33	-49	57	-5,955	433	52.0% GM_Superior_parietal_lobule_7PC_L; 42.0% GM_Superior_parietal_lobule_7A_L; 27.0% GM_Primary_somatosensory_cortex_BA2_L; 27.0% GM_Anterior_intra-parietal_sulcus_hIP3_L; 20.0% GM_Primary_somatosensory_cortex_BA1_L	53.0% Left_Superior_Parietal_Lobule	Parietal_Sup_L
28	-3	-44	-13	-6,123	270	0% no_label	0% no_label	Vermis_3
11	-15	-47	-25	-6,432	928	0% no_label	0% no_label	Cerebelum_4_5_L
1	31	-80	-33	-6,505	469402	0% no_label	0% no_label	Cerebelum_Crus1_R
25	-32	33	-12	-7,160	342	0% no_label	47.0% Left_Frontal_Orbital_Cortex; 27.0% Left_Frontal_Pole	Frontal_Inf_Orb_2_L
27	6	-25	58	-7,254	303	75.0% GM_Primary_motor_cortex_BA4a_R; 42.0% GM_Premotor_cortex_BA6_R; 10.0% WM_Corticospinal_tract_R	59.0% Right_Precentral_Gyrus	Supp_Motor_Area_R
4	-27	-33	66	-9,444	6345	30.0% GM_Primary_somatosensory_cortex_BA3b_L; 25.0% GM_Primary_motor_cortex_BA4a_L; 22.0% GM_Primary_somatosensory_cortex_BA1_L; 20.0% GM_Primary_somatosensory_cortex_BA2_L; 20.0% GM_Primary_motor_cortex_BA4p_L; 19.0% WM_Corticospinal_tract_L; 14.0% GM_Premotor_cortex_BA6_L	66.0% Left_Postcentral_Gyrus; 12.0% Left_Precentral_Gyrus	Postcentral_L
1	49	-9	52	-11,874	469402	67.0% GM_Premotor_cortex_BA6_R; 34.0% GM_Primary_somatosensory_cortex_BA1_R; 13.0% GM_Primary_somatosensory_cortex_BA3b_R; 9.0% WM_Corticospinal_tract_R; 8.0% GM_Primary_motor_cortex_BA4a_R	65.0% Right_Precentral_Gyrus; 13.0% Right_Postcentral_Gyrus	Frontal_Mid_2_R
1	-30	0	-16	-16,246	469402	23.0% GM_Amygdala_superficial_group_L; 9.0% WM_Uncinate_fascicle_L	62.0% Left_Amygdala	no_label

Hierarchical right LB

cluster_id	peak_x	peak_y	peak_z	peak_value	volume_mm	juelich	harvard_oxford	aal
1	29	0	-26	18,830	238344	79.0% GM_Amygdala_laterobasal_group_R	67.0% Right_Amygdala	Amygdala_R
4	3	-15	-7	8,214	1616	0% no_label	0% no_label	no_label
1	7	-3	72	8,024	238344	100.0% GM_Premotor_cortex_BA6_R	36.0% Right_Juxtapositional_Lobule_Cortex_(formerly_Supplementary_Motor_Cortex); 27.0% Right_Superior_Frontal_Gyrus; 10.0% Right_Precentral_Gyrus	Supp_Motor_Area_R
10	26	-18	6	6,382	844	68.0% WM_Corticospinal_tract_R	8.0% Right_Putamen; 5.0% Right_Pallidum	no_label
7	52	-20	43	6,329	1246	67.0% GM_Primary_somatosensory_cortex_BA2_R; 24.0% GM_Inferior_parietal_lobule_PFt_R; 22.0% GM_Primary_somatosensory_cortex_BA1_R; 10.0% GM_Primary_somatosensory_cortex_BA3b_R; 10.0% GM_Inferior_parietal_lobule_PFop_R; 5.0% GM_Primary_motor_cortex_BA4a_R	59.0% Right_Postcentral_Gyrus; 10.0% Right_Supramarginal_Gyrus_anterior_division	Postcentral_R
21	42	-49	-23	6,274	348	0% no_label	69.0% Right_Temporal_Occipital_Fusiform_Cortex; 6.0% Right_Inferior_Temporal_Gyrus_temporooccipital_part	Fusiform_R
23	61	-12	29	6,271	322	40.0% GM_Primary_somatosensory_cortex_BA3b_R; 22.0% GM_Primary_somatosensory_cortex_BA2_R; 12.0% GM_Secondary_somatosensory_cortex_/_Parietal_operculum_OP4_R; 11.0% GM_Inferior_parietal_lobule_PFop_R; 10.0% GM_Primary_somatosensory_cortex_BA1_R; 10.0% GM_Inferior_parietal_lobule_PFt_R	50.0% Right_Postcentral_Gyrus	Postcentral_R
28	-55	-22	48	5,906	217	72.0% GM_Primary_somatosensory_cortex_BA1_L; 62.0% GM_Primary_somatosensory_cortex_BA2_L; 20.0% GM_Inferior_parietal_lobule_PFt_L	69.0% Left_Postcentral_Gyrus	Parietal_Inf_L
11	13	-40	75	5,847	779	40.0% GM_Superior_parietal_lobule_5L_R; 28.0% GM_Primary_somatosensory_cortex_BA3b_R; 20.0% GM_Primary_somatosensory_cortex_BA1_R; 20.0% GM_Primary_motor_cortex_BA4a_R; 14.0% GM_Primary_motor_cortex_BA4p_R; 10.0% GM_Primary_somatosensory_cortex_BA2_R	56.0% Right_Postcentral_Gyrus; 6.0% Right_Superior_Parietal_Lobule	Postcentral_R
19	31	-20	18	5,800	428	33.0% GM_Secondary_somatosensory_cortex_/_Parietal_operculum_OP2_R; 26.0% WM_Superior_longitudinal_fascicle_R; 11.0% GM_Insula_Ig2_R	13.0% Right_Insular_Cortex	Insula_R
22	54	-53	-22	-6,231	341	0% no_label	70.0% Right_Inferior_Temporal_Gyrus_temporooccipital_part; 8.0% Right_Temporal_Occipital_Fusiform_Cortex	Temporal_Inf_R
6	-43	-19	68	-6,876	1260	0% no_label	7.0% Left_Postcentral_Gyrus	Precentral_L
9	-27	41	-11	-7,518	882	0% no_label	63.0% Left_Frontal_Pole; 7.0% Left_Frontal_Orbital_Cortex	Frontal_Mid_2_L
8	-53	-11	54	-7,650	1028	0% no_label	27.0% Left_Precentral_Gyrus; 19.0% Left_Postcentral_Gyrus	Postcentral_L
14	7	-23	-21	-7,754	557	0% no_label	91.0% Brain-Stem	no_label
13	45	24	-26	-7,761	626	0% no_label	58.0% Right_Temporal_Pole	Temporal_Pole_Sup_R
3	35	26	10	-8,419	2387	0% no_label	30.0% Right_Frontal_Operculum_Cortex; 17.0% Right_Inferior_Frontal_Gyrus_pars_triangularis	Frontal_Inf_Tri_R
2	-2	-84	40	-9,660	185899	27.0% GM_Superior_parietal_lobule_7P_L; 10.0% GM_Superior_parietal_lobule_7M_L	24.0% Left_Cuneal_Cortex; 22.0% Left_Precuneous_Cortex	Cuneus_L
5	0	22	34	-9,986	1320	0% no_label	39.0% Left_Cingulate_Gyrus_anterior_division; 28.0% Left_Paracingulate_Gyrus; 8.0% Right_Cingulate_Gyrus_anterior_division; 6.0% Right_Paracingulate_Gyrus	Cingulate_Mid_L
2	24	-1	-15	-15,569	185899	59.0% GM_Amygdala_superficial_group_R; 34.0% GM_Amygdala_laterobasal_group_R	91.0% Right_Amygdala	Amygdala_R

Hierarchical right CM

cluster_id	peak_x	peak_y	peak_z	peak_value	volume_mm	juelich	harvard_oxford	aal
1	26	1	-14	23,795	48445	44.0% GM_Amygdala_superficial_group_R; 7.0% GM_Amygdala_laterobasal_group_R	52.0% Right_Amygdala	Amygdala_R
3	3	15	39	8,179	7621	10.0% GM_Premotor_cortex_BA6_R	49.0% Right_Cingulate_Gyrus_anterior_division; 41.0% Right_Paracingulate_Gyrus	Cingulate_Mid_L
7	0	-54	52	7,935	1879	12.0% GM_Superior_parietal_lobule_7P_R; 9.0% GM_Superior_parietal_lobule_7A_R; 6.0% GM_Superior_parietal_lobule_5M_R	33.0% Left_Precuneous_Cortex; 23.0% Right_Precuneous_Cortex	Precuneus_L
2	-1	-77	-12	7,672	14130	0% no_label	21.0% Left_Lingual_Gyrus; 8.0% Right_Lingual_Gyrus	Vermis_6
5	-62	6	1	7,225	2941	10.0% GM_Secondary_somatosensory_cortex_/_Parietal_operculum_OP4_L; 9.0% GM_Broca's_area_BA44_L; 5.0% GM_Broca's_area_BA45_L	9.0% Left_Precentral_Gyrus	no_label
8	1	-46	-2	7,223	1493	0% no_label	0% no_label	Vermis_4_5
22	13	-81	8	6,466	280	100.0% GM_Visual_cortex_V1_BA17_R; 16.0% WM_Optic_radiation_R	66.0% Right_Intracalcarine_Cortex	Calcarine_R
14	0	-31	27	6,404	533	15.0% WM_Callosal_body	62.0% Left_Cingulate_Gyrus_posterior_division; 8.0% Right_Cingulate_Gyrus_posterior_division	no_label
9	26	50	22	6,103	968	0% no_label	76.0% Right_Frontal_Pole	Frontal_Sup_2_R
10	7	-36	51	6,096	906	68.0% GM_Superior_parietal_lobule_5M_R; 40.0% GM_Superior_parietal_lobule_5Ci_R; 29.0% GM_Primary_motor_cortex_BA4a_R; 7.0% WM_Corticospinal_tract_R	29.0% Right_Precuneous_Cortex; 25.0% Right_Postcentral_Gyrus; 15.0% Right_Precentral_Gyrus; 13.0% Right_Cingulate_Gyrus_posterior_division	Paracentral_Lobule_R
15	3	-4	-13	-5,950	430	29.0% GM_Mamillary_body; 16.0% WM_Fornix	0% no_label	no_label
21	31	-20	-16	-6,527	292	90.0% GM_Hippocampus_cornu_ammonis_R; 82.0% GM_Hippocampus_dentate_gyrus_R; 49.0% GM_Hippocampus_subiculum_R	99.0% Right_Hippocampus	Hippocampus_R
16	6	15	15	-7,184	391	61.0% WM_Callosal_body	61.0% Right_Lateral_Ventricle	no_label
11	-8	5	21	-7,338	843	49.0% WM_Callosal_body	70.0% Left_Lateral_Ventrical	no_label
6	-20	-6	-19	-11,267	2193	89.0% GM_Amygdala_laterobasal_group_L; 72.0% GM_Amygdala_superficial_group_L; 13.0% GM_Hippocampus_cornu_ammonis_L; 9.0% GM_Amygdala_centromedial_group_L	88.0% Left_Amygdala; 11.0% Left_Hippocampus	Hippocampus_L
4	22	-5	-18	-13,814	3702	62.0% GM_Amygdala_superficial_group_R; 60.0% GM_Amygdala_laterobasal_group_R; 10.0% GM_Hippocampus_subiculum_R; 10.0% GM_Amygdala_centromedial_group_R	94.0% Right_Amygdala	Amygdala_R

Hierarchical right SF

cluster_id	peak_x	peak_y	peak_z	peak_value	volume_mm	juelich	harvard_oxford	aal
3	24	4	-23	19,677	19057	14.0% GM_Hippocampus_entorhinal_cortex_R	36.0% Right_Amygdala; 24.0% Right_Parahippocampal_Gyrus_anterior_division; 19.0% Right_Temporal_Pole	ParaHippocampal_R
5	-3	22	8	12,412	4813	36.0% WM_Callosal_body	30.0% Left_Lateral_Ventrical	no_label
31	-1	-6	5	10,543	296	0% no_label	78.0% Left_Thalamus	no_label
2	53	-68	40	9,494	62964	0% no_label	25.0% Right_Lateral_Occipital_Cortex_superior_division	Angular_R
2	-48	-68	46	8,971	62964	0% no_label	56.0% Left_Lateral_Occipital_Cortex_superior_division	no_label
9	25	-23	-16	8,800	1303	100.0% GM_Hippocampus_subiculum_R; 10.0% GM_Hippocampus_dentate_gyrus_R; 7.0% GM_Lateral_geniculate_body_R; 7.0% GM_Hippocampus_cornu_ammonis_R	70.0% Right_Hippocampus; 6.0% Right_Parahippocampal_Gyrus_posterior_division	ParaHippocampal_R
17	45	-46	-22	8,405	674	0% no_label	59.0% Right_Temporal_Occipital_Fusiform_Cortex; 27.0% Right_Inferior_Temporal_Gyrus_temporooccipital_part	Temporal_Inf_R
6	-39	-3	19	8,213	4280	0% no_label	31.0% Left_Central_Opercular_Cortex	no_label
14	4	-24	-12	8,182	739	0% no_label	13.0% Brain-Stem	no_label
11	36	31	6	7,959	791	10.0% GM_Broca's_area_BA45_R	9.0% Right_Inferior_Frontal_Gyrus_pars_triangularis; 8.0% Right_Frontal_Operculum_Cortex; 7.0% Right_Frontal_Orbital_Cortex	Insula_R
39	-32	25	2	-5,930	219	0% no_label	46.0% Left_Insular_Cortex; 18.0% Left_Frontal_Operculum_Cortex; 18.0% Left_Frontal_Orbital_Cortex	Insula_L
26	-50	-38	39	-5,973	385	48.0% GM_Inferior_parietal_lobule_PF_L; 36.0% GM_Anterior_intra-parietal_sulcus_hIP2_L; 11.0% GM_Inferior_parietal_lobule_PFm_L; 7.0% GM_Inferior_parietal_lobule_PFt_L	15.0% Left_Supramarginal_Gyrus_anterior_division; 12.0% Left_Supramarginal_Gyrus_posterior_division	Parietal_Inf_L
19	-51	-23	45	-5,994	557	99.0% GM_Primary_somatosensory_cortex_BA2_L; 46.0% GM_Primary_somatosensory_cortex_BA1_L; 26.0% GM_Primary_somatosensory_cortex_BA3b_L; 22.0% GM_Inferior_parietal_lobule_PFt_L	64.0% Left_Postcentral_Gyrus; 6.0% Left_Supramarginal_Gyrus_anterior_division	Postcentral_L
40	34	32	-12	-6,010	215	0% no_label	42.0% Right_Frontal_Orbital_Cortex; 25.0% Right_Frontal_Pole	Frontal_Inf_Orb_2_R
42	-8	-69	-15	-6,416	202	0% no_label	0% no_label	Cerebelum_6_L
23	-16	-48	-30	-6,610	475	0% no_label	0% no_label	no_label
7	32	-34	59	-7,235	1487	68.0% GM_Primary_somatosensory_cortex_BA3b_R; 50.0% GM_Primary_motor_cortex_BA4p_R; 24.0% GM_Primary_motor_cortex_BA4a_R; 14.0% GM_Primary_somatosensory_cortex_BA2_R; 10.0% GM_Primary_somatosensory_cortex_BA1_R	42.0% Right_Postcentral_Gyrus; 5.0% Right_Supramarginal_Gyrus_anterior_division; 5.0% Right_Superior_Parietal_Lobule	Postcentral_R
4	42	-49	-25	-7,491	8828	0% no_label	42.0% Right_Temporal_Occipital_Fusiform_Cortex	Fusiform_R
1	-50	-9	53	-8,644	388307	32.0% GM_Premotor_cortex_BA6_L; 12.0% GM_Primary_somatosensory_cortex_BA1_L; 6.0% GM_Primary_motor_cortex_BA4a_L	76.0% Left_Precentral_Gyrus; 7.0% Left_Postcentral_Gyrus	Postcentral_L
1	22	3	-17	-14,144	388307	29.0% GM_Amygdala_superficial_group_R; 9.0% GM_Hippocampus_entorhinal_cortex_R	36.0% Right_Amygdala; 9.0% Right_Parahippocampal_Gyrus_anterior_division	Amygdala_R

Jülich left LB

cluster_id	peak_x	peak_y	peak_z	peak_value	volume_mm	juelich	harvard_oxford	aal
1	-26	0	-27	20,434	685568	72.0% GM_Amygdala_laterobasal_group_L; 9.0% GM_Amygdala_superficial_group_L	47.0% Left_Amygdala; 20.0% Left_Parahippocampal_Gyrus_anterior_division; 5.0% Left_Temporal_Pole	Amygdala_L
1	-13	-27	72	10,848	685568	50.0% GM_Premotor_cortex_BA6_L; 48.0% GM_Primary_motor_cortex_BA4a_L; 30.0% WM_Corticospinal_tract_L; 20.0% GM_Primary_somatosensory_cortex_BA3b_L; 16.0% GM_Primary_somatosensory_cortex_BA1_L	42.0% Left_Precentral_Gyrus; 5.0% Left_Postcentral_Gyrus	Paracentral_Lobule_L
1	60	22	21	8,372	685568	80.0% GM_Broca's_area_BA45_R; 22.0% GM_Broca's_area_BA44_R	21.0% Right_Inferior_Frontal_Gyrus_pars_opercularis; 14.0% Right_Inferior_Frontal_Gyrus_pars_triangularis	Frontal_Inf_Tri_R
18	-62	-29	33	6,956	338	70.0% GM_Inferior_parietal_lobule_PF_L; 34.0% GM_Inferior_parietal_lobule_PFop_L; 32.0% GM_Inferior_parietal_lobule_PFt_L; 10.0% GM_Secondary_somatosensory_cortex_/_Parietal_operculum_OP1_L	71.0% Left_Supramarginal_Gyrus_anterior_division; 16.0% Left_Postcentral_Gyrus	SupraMarginal_L
4	17	-48	-29	6,494	4533	0% no_label	0% no_label	no_label
16	40	-86	1	5,425	365	16.0% GM_Visual_cortex_V4_R; 6.0% GM_Visual_cortex_V3V_R	53.0% Right_Lateral_Occipital_Cortex_inferior_division; 15.0% Right_Occipital_Pole	Occipital_Mid_R
13	-26	-66	28	5,384	526	10.0% GM_Anterior_intra-parietal_sulcus_hIP1_L	31.0% Left_Lateral_Occipital_Cortex_superior_division	Occipital_Mid_L
19	21	-55	17	5,150	285	12.0% WM_Callosal_body; 7.0% WM_Optic_radiation_R	35.0% Right_Precuneous_Cortex; 10.0% Right_Supracalcarine_Cortex	Calcarine_R
1	51	-77	-5	5,132	685568	8.0% GM_Visual_cortex_V4_R	69.0% Right_Lateral_Occipital_Cortex_inferior_division	Occipital_Inf_R
23	22	-62	11	4,954	207	56.0% GM_Visual_cortex_V1_BA17_R; 39.0% WM_Optic_radiation_R; 27.0% GM_Visual_cortex_V2_BA18_R; 9.0% WM_Callosal_body	21.0% Right_Precuneous_Cortex; 18.0% Right_Supracalcarine_Cortex; 17.0% Right_Intracalcarine_Cortex	Calcarine_R
15	41	22	-25	-7,512	480	0% no_label	76.0% Right_Temporal_Pole; 6.0% Right_Frontal_Orbital_Cortex	Temporal_Pole_Sup_R
20	7	-21	-20	-7,560	284	0% no_label	66.0% Brain-Stem	no_label
8	-3	-40	-1	-7,563	1093	0% no_label	0% no_label	no_label
6	-28	-73	10	-7,795	1620	60.0% WM_Callosal_body; 22.0% WM_Optic_radiation_L; 10.0% GM_Visual_cortex_V1_BA17_L	0% no_label	no_label
3	-6	-81	52	-8,011	7792	72.0% GM_Superior_parietal_lobule_7P_L; 6.0% GM_Superior_parietal_lobule_7A_L	18.0% Left_Lateral_Occipital_Cortex_superior_division; 14.0% Left_Precuneous_Cortex	Precuneus_L
22	12	-8	15	-8,303	209	0% no_label	86.0% Right_Thalamus	Thalamus_R
10	1	17	-3	-9,099	847	26.0% WM_Callosal_body	67.0% Right_Subcallosal_Cortex; 8.0% Left_Subcallosal_Cortex	Olfactory_R
5	-3	22	8	-9,594	2714	36.0% WM_Callosal_body	30.0% Left_Lateral_Ventrical	no_label
12	-1	-5	5	-11,272	584	0% no_label	67.0% Left_Thalamus	no_label
2	-20	-2	-12	-12,654	8479	78.0% GM_Amygdala_superficial_group_L; 15.0% GM_Amygdala_centromedial_group_L; 5.0% GM_Amygdala_laterobasal_group_L	30.0% Left_Amygdala	Amygdala_L

Jülich left CM

cluster_id	peak_x	peak_y	peak_z	peak_value	volume_mm	juelich	harvard_oxford	aal
1	-24	0	-15	19,140	149486	61.0% GM_Amygdala_superficial_group_L	54.0% Left_Amygdala	Amygdala_L
2	-1	26	32	9,782	6856	0% no_label	44.0% Left_Paracingulate_Gyrus; 42.0% Left_Cingulate_Gyrus_anterior_division	Cingulate_Mid_L
1	-1	-79	49	8,545	149486	61.0% GM_Superior_parietal_lobule_7P_L; 25.0% GM_Superior_parietal_lobule_7M_L	32.0% Left_Precuneous_Cortex	Precuneus_L
5	54	-36	32	7,359	1689	30.0% GM_Inferior_parietal_lobule_PFcm_R; 21.0% GM_Inferior_parietal_lobule_PF_R; 19.0% GM_Inferior_parietal_lobule_PFm_R; 10.0% GM_Anterior_intra-parietal_sulcus_hIP2_R	19.0% Right_Supramarginal_Gyrus_posterior_division; 18.0% Right_Parietal_Operculum_Cortex; 6.0% Right_Supramarginal_Gyrus_anterior_division; 5.0% Right_Planum_Temporale	SupraMarginal_R
16	9	-31	-20	6,435	305	0% no_label	100.0% Brain-Stem	no_label
9	59	-46	49	6,164	443	65.0% GM_Inferior_parietal_lobule_PFm_R; 9.0% GM_Inferior_parietal_lobule_PF_R; 8.0% GM_Inferior_parietal_lobule_Pga_R	28.0% Right_Angular_Gyrus; 16.0% Right_Supramarginal_Gyrus_posterior_division	Parietal_Inf_R
10	0	-53	-22	6,160	427	0% no_label	0% no_label	Vermis_4_5
14	-59	-61	-8	6,068	356	0% no_label	38.0% Left_Middle_Temporal_Gyrus_temporooccipital_part; 27.0% Left_Lateral_Occipital_Cortex_inferior_division; 16.0% Left_Inferior_Temporal_Gyrus_temporooccipital_part	Temporal_Inf_L
17	51	-48	36	6,009	255	54.0% GM_Inferior_parietal_lobule_PFm_R; 30.0% GM_Inferior_parietal_lobule_Pga_R	43.0% Right_Angular_Gyrus; 17.0% Right_Supramarginal_Gyrus_posterior_division	Angular_R
12	10	-45	42	5,865	408	10.0% GM_Superior_parietal_lobule_5Ci_R; 5.0% GM_Superior_parietal_lobule_5M_R	43.0% Right_Precuneous_Cortex; 20.0% Right_Cingulate_Gyrus_posterior_division	Precuneus_R
7	-61	-13	-18	-4,969	672	0% no_label	44.0% Left_Middle_Temporal_Gyrus_posterior_division; 23.0% Left_Middle_Temporal_Gyrus_anterior_division	Temporal_Mid_L
13	-11	-26	75	-5,321	384	63.0% GM_Premotor_cortex_BA6_L; 53.0% GM_Primary_motor_cortex_BA4a_L; 40.0% WM_Corticospinal_tract_L; 20.0% GM_Primary_somatosensory_cortex_BA3b_L; 14.0% GM_Primary_somatosensory_cortex_BA1_L	49.0% Left_Precentral_Gyrus; 5.0% Left_Postcentral_Gyrus	Paracentral_Lobule_L
18	-46	9	-25	-5,329	240	0% no_label	39.0% Left_Temporal_Pole	Temporal_Pole_Sup_L
19	-30	-48	1	-5,789	219	6.0% WM_Callosal_body	73.0% Left_Lateral_Ventrical	no_label
6	-5	10	14	-7,405	1589	0% no_label	97.0% Left_Lateral_Ventrical	no_label
4	20	-6	-19	-7,954	1837	66.0% GM_Amygdala_superficial_group_R; 47.0% GM_Amygdala_laterobasal_group_R; 20.0% GM_Hippocampus_entorhinal_cortex_R; 17.0% GM_Hippocampus_subiculum_R; 16.0% GM_Hippocampus_hippocampal-amygdaloid_transition_area_R; 10.0% GM_Amygdala_centromedial_group_R	80.0% Right_Amygdala; 18.0% Right_Hippocampus	Hippocampus_R
3	-21	0	-24	-13,461	3434	32.0% GM_Amygdala_laterobasal_group_L; 14.0% GM_Amygdala_superficial_group_L; 8.0% GM_Hippocampus_entorhinal_cortex_L	59.0% Left_Amygdala; 32.0% Left_Parahippocampal_Gyrus_anterior_division	Amygdala_L

Jülich left SF

cluster_id	peak_x	peak_y	peak_z	peak_value	volume_mm	juelich	harvard_oxford	aal
2	-20	2	-23	18,671	8 525	23.0% GM_Amygdala_laterobasal_group_L; 12.0% GM_Amygdala_superficial_group_L; 10.0% GM_Hippocampus_entorhinal_cortex_L	39.0% Left_Parahippocampal_Gyrus_anterior_division; 26.0% Left_Amygdala; 13.0% Left_Temporal_Pole	ParaHippocampal_L
3	5	23	7	9,963	3 392	75.0% WM_Callosal_body	33.0% Right_Lateral_Ventricle	no_label
5	-44	-82	35	5,685	322	0% no_label	20.0% Left_Lateral_Occipital_Cortex_superior_division	no_label
4	-31	-63	4	5,601	447	41.0% WM_Callosal_body; 29.0% WM_Optic_radiation_L; 7.0% GM_Visual_cortex_V1_BA17_L	0% no_label	no_label
1	5	-94	16	-7,106	1 131 430	0% no_label	59.0% Right_Occipital_Pole; 7.0% Right_Supracalcarine_Cortex; 5.0% Left_Occipital_Pole	Cuneus_R
1	53	-8	51	-10,811	1 131 430	76.0% GM_Premotor_cortex_BA6_R; 30.0% GM_Primary_somatosensory_cortex_BA1_R; 13.0% GM_Primary_somatosensory_cortex_BA3b_R; 11.0% GM_Primary_motor_cortex_BA4a_R	57.0% Right_Precentral_Gyrus; 19.0% Right_Postcentral_Gyrus	Frontal_Mid_2_R
1	-29	0	-15	-16,501	1 131 430	27.0% GM_Amygdala_superficial_group_L; 10.0% WM_Uncinate_fascicle_L	57.0% Left_Amygdala	no_label

Jülich right LB

cluster_id	peak_x	peak_y	peak_z	peak_value	volume_mm	juelich	harvard_oxford	aal
1	29	0	-26	20,503	428333	79.0% GM_Amygdala_laterobasal_group_R	67.0% Right_Amygdala	Amygdala_R
1	7	-3	72	9,933	428333	100.0% GM_Premotor_cortex_BA6_R	36.0% Right_Juxtapositional_Lobule_Cortex_(formerly_Supplementary_Motor_Cortex); 27.0% Right_Superior_Frontal_Gyrus; 10.0% Right_Precentral_Gyrus	Supp_Motor_Area_R
17	17	4	3	8,829	317	0% no_label	71.0% Right_Pallidum; 6.0% Right_Putamen	Pallidum_R
16	0	-18	-23	6,998	324	0% no_label	95.0% Brain-Stem	no_label
4	-8	-40	32	6,595	2883	30.0% WM_Cingulum_L	28.0% Left_Cingulate_Gyrus_posterior_division	Cingulate_Mid_L
19	-15	-51	-30	6,016	294	0% no_label	0% no_label	no_label
20	-19	-45	62	5,458	291	81.0% GM_Superior_parietal_lobule_5L_L; 25.0% GM_Primary_somatosensory_cortex_BA2_L; 16.0% GM_Primary_somatosensory_cortex_BA3b_L; 10.0% GM_Superior_parietal_lobule_5Ci_L; 6.0% GM_Primary_somatosensory_cortex_BA1_L; 5.0% GM_Superior_parietal_lobule_7A_L	37.0% Left_Postcentral_Gyrus; 22.0% Left_Superior_Parietal_Lobule	Parietal_Sup_L
1	-65	-37	-17	4,170	428333	0% no_label	45.0% Left_Middle_Temporal_Gyrus_posterior_division; 28.0% Left_Inferior_Temporal_Gyrus_posterior_division	Temporal_Mid_L
14	7	-23	-21	-6,962	358	0% no_label	91.0% Brain-Stem	no_label
8	35	27	10	-7,320	977	0% no_label	22.0% Right_Inferior_Frontal_Gyrus_pars_triangularis; 18.0% Right_Frontal_Operculum_Cortex	Frontal_Inf_Tri_R
13	0	25	32	-7,324	367	0% no_label	33.0% Left_Cingulate_Gyrus_anterior_division; 26.0% Left_Paracingulate_Gyrus; 9.0% Right_Cingulate_Gyrus_anterior_division; 8.0% Right_Paracingulate_Gyrus	Cingulate_Mid_L
12	-27	41	-11	-7,478	426	0% no_label	63.0% Left_Frontal_Pole; 7.0% Left_Frontal_Orbital_Cortex	Frontal_Mid_2_L
15	-19	10	20	-7,734	341	35.0% WM_Superior_occipito-frontal_fascicle_L	9.0% Left_Caudate	Caudate_L
9	34	21	-27	-8,265	592	0% no_label	59.0% Right_Temporal_Pole; 10.0% Right_Frontal_Orbital_Cortex	Temporal_Pole_Sup_R
2	-19	-85	48	-8,399	50337	0% no_label	37.0% Left_Lateral_Occipital_Cortex_superior_division	Occipital_Sup_L
5	-33	26	12	-9,239	2398	10.0% GM_Broca's_area_BA45_L	14.0% Left_Frontal_Operculum_Cortex; 6.0% Left_Inferior_Frontal_Gyrus_pars_triangularis	Frontal_Inf_Tri_L
6	2	-4	4	-10,632	1853	25.0% WM_Fornix	77.0% Right_Thalamus	no_label
3	21	0	-18	-13,340	13777	64.0% GM_Amygdala_superficial_group_R; 13.0% GM_Hippocampus_entorhinal_cortex_R; 13.0% GM_Amygdala_laterobasal_group_R	84.0% Right_Amygdala; 7.0% Right_Parahippocampal_Gyrus_anterior_division	Amygdala_R

Jülich right CM

cluster_id	peak_x	peak_y	peak_z	peak_value	volume_mm	juelich	harvard_oxford	aal
1	25	0	-14	20,568	146910	70.0% GM_Amygdala_superficial_group_R; 30.0% GM_Amygdala_laterobasal_group_R	65.0% Right_Amygdala	Amygdala_R
1	0	-95	10	8,144	146910	60.0% GM_Visual_cortex_V1_BA17_R; 27.0% GM_Visual_cortex_V2_BA18_R	53.0% Left_Occipital_Pole; 10.0% Right_Occipital_Pole	Calcarine_L
8	-1	-63	-32	7,733	608	0% no_label	0% no_label	Vermis_8
7	53	-36	31	7,460	813	22.0% GM_Inferior_parietal_lobule_PFcm_R; 21.0% GM_Inferior_parietal_lobule_PFm_R; 21.0% GM_Inferior_parietal_lobule_PF_R; 10.0% GM_Anterior_intra-parietal_sulcus_hIP2_R	19.0% Right_Parietal_Operculum_Cortex; 18.0% Right_Supramarginal_Gyrus_posterior_division; 6.0% Right_Planum_Temporale; 6.0% Right_Supramarginal_Gyrus_anterior_division	SupraMarginal_R
20	26	-22	-9	6,727	248	86.0% GM_Lateral_geniculate_body_R; 39.0% WM_Optic_radiation_R; 7.0% GM_Hippocampus_subiculum_R	22.0% Right_Hippocampus	no_label
4	16	-44	-34	6,337	1636	0% no_label	0% no_label	no_label
13	-47	22	-6	6,318	368	14.0% GM_Broca's_area_BA45_L; 5.0% GM_Broca's_area_BA44_L	38.0% Left_Frontal_Orbital_Cortex; 24.0% Left_Frontal_Operculum_Cortex	Frontal_Inf_Orb_2_L
12	-42	-56	61	6,275	402	6.0% GM_Superior_parietal_lobule_7A_L; 6.0% GM_Anterior_intra-parietal_sulcus_hIP3_L	11.0% Left_Superior_Parietal_Lobule; 6.0% Left_Lateral_Occipital_Cortex_superior_division	Parietal_Inf_L
15	-21	-31	61	6,091	342	39.0% GM_Primary_motor_cortex_BA4p_L; 25.0% WM_Corticospinal_tract_L; 24.0% GM_Primary_somatosensory_cortex_BA3b_L; 20.0% GM_Premotor_cortex_BA6_L; 19.0% GM_Primary_somatosensory_cortex_BA1_L; 14.0% GM_Primary_motor_cortex_BA4a_L; 10.0% GM_Primary_somatosensory_cortex_BA2_L	39.0% Left_Postcentral_Gyrus; 23.0% Left_Precentral_Gyrus	Postcentral_L
21	56	-2	14	5,958	247	39.0% GM_Secondary_somatosensory_cortex_/_Parietal_operculum_OP4_R; 8.0% GM_Secondary_somatosensory_cortex_/_Parietal_operculum_OP3_R; 6.0% GM_Primary_somatosensory_cortex_BA3b_R	23.0% Right_Central_Opercular_Cortex; 14.0% Right_Precentral_Gyrus	Rolandic_Oper_R
14	-7	3	73	-5,346	346	80.0% GM_Premotor_cortex_BA6_L	57.0% Left_Superior_Frontal_Gyrus	Supp_Motor_Area_L
17	27	52	-4	-5,440	303	0% no_label	45.0% Right_Frontal_Pole	Frontal_Sup_2_R
19	6	-16	75	-5,530	264	90.0% GM_Premotor_cortex_BA6_R; 10.0% GM_Primary_motor_cortex_BA4a_R	47.0% Right_Precentral_Gyrus; 9.0% Right_Juxtapositional_Lobule_Cortex_(formerly_Supplementary_Motor_Cortex); 8.0% Right_Superior_Frontal_Gyrus	Supp_Motor_Area_R
11	-11	-29	74	-5,590	453	40.0% GM_Primary_motor_cortex_BA4a_L; 36.0% GM_Premotor_cortex_BA6_L; 30.0% GM_Primary_somatosensory_cortex_BA3b_L; 28.0% WM_Corticospinal_tract_L; 20.0% GM_Primary_somatosensory_cortex_BA1_L; 10.0% GM_Superior_parietal_lobule_5L_L	50.0% Left_Precentral_Gyrus; 11.0% Left_Postcentral_Gyrus	Paracentral_Lobule_L
18	18	-34	15	-5,988	270	16.0% WM_Fornix	84.0% Right_Lateral_Ventricle	no_label
5	-3	60	-12	-6,138	1450	0% no_label	86.0% Left_Frontal_Pole	Frontal_Med_Orb_L
6	-4	10	12	-7,241	1099	0% no_label	99.0% Left_Lateral_Ventrical	no_label
10	10	-9	19	-7,389	579	0% no_label	62.0% Right_Lateral_Ventricle; 22.0% Right_Thalamus	no_label
3	-23	-9	-20	-7,998	8812	85.0% GM_Amygdala_laterobasal_group_L; 63.0% GM_Hippocampus_cornu_ammonis_L; 33.0% GM_Amygdala_superficial_group_L; 20.0% GM_Hippocampus_subiculum_L; 10.0% GM_Hippocampus_hippocampal-amygdaloid_transition_area_L	57.0% Left_Hippocampus; 39.0% Left_Amygdala	Hippocampus_L
2	24	2	-24	-13,061	9922	21.0% GM_Hippocampus_entorhinal_cortex_R; 20.0% GM_Amygdala_laterobasal_group_R; 10.0% GM_Amygdala_superficial_group_R	63.0% Right_Amygdala; 23.0% Right_Parahippocampal_Gyrus_anterior_division; 5.0% Right_Temporal_Pole	Amygdala_R

Jülich right SF

cluster_id	peak_x	peak_y	peak_z	peak_value	volume_mm	juelich	harvard_oxford	aal
2	23	4	-22	19,063	2175	16.0% GM_Hippocampus_entorhinal_cortex_R	36.0% Right_Amygdala; 26.0% Right_Parahippocampal_Gyrus_anterior_division; 15.0% Right_Temporal_Pole	ParaHippocampal_R
5	-3	1	-11	8,500	1258	8.0% GM_Mamillary_body; 7.0% WM_Fornix	0% no_label	no_label
6	-20	1	-22	8,001	627	27.0% GM_Amygdala_laterobasal_group_L; 14.0% GM_Amygdala_superficial_group_L; 10.0% GM_Hippocampus_entorhinal_cortex_L	44.0% Left_Amygdala; 31.0% Left_Parahippocampal_Gyrus_anterior_division; 6.0% Left_Temporal_Pole	Amygdala_L
11	-21	9	-20	6,156	281	0% no_label	71.0% Left_Frontal_Orbital_Cortex	OFCpost_L
13	46	-34	19	-5,152	209	21.0% GM_Inferior_parietal_lobule_PFcm_R; 10.0% GM_Secondary_somatosensory_cortex_/_Parietal_operculum_OP1_R	33.0% Right_Planum_Temporale; 31.0% Right_Parietal_Operculum_Cortex; 6.0% Right_Supramarginal_Gyrus_posterior_division	Temporal_Sup_R
10	-61	4	8	-5,302	299	30.0% GM_Broca's_area_BA44_L; 20.0% GM_Secondary_somatosensory_cortex_/_Parietal_operculum_OP4_L	69.0% Left_Precentral_Gyrus	Rolandic_Oper_L
8	-37	-38	-21	-5,492	492	0% no_label	55.0% Left_Temporal_Fusiform_Cortex_posterior_division; 5.0% Left_Temporal_Occipital_Fusiform_Cortex	Fusiform_L
12	60	-31	31	-5,495	215	73.0% GM_Inferior_parietal_lobule_PF_R; 52.0% GM_Inferior_parietal_lobule_PFcm_R	38.0% Right_Supramarginal_Gyrus_anterior_division; 21.0% Right_Parietal_Operculum_Cortex; 10.0% Right_Planum_Temporale; 8.0% Right_Supramarginal_Gyrus_posterior_division	SupraMarginal_R
7	-27	-27	-17	-5,497	585	57.0% GM_Hippocampus_subiculum_L; 52.0% GM_Hippocampus_cornu_ammonis_L; 26.0% GM_Hippocampus_dentate_gyrus_L	42.0% Left_Hippocampus; 10.0% Left_Parahippocampal_Gyrus_posterior_division	ParaHippocampal_L
4	-28	-31	68	-5,590	1283	40.0% GM_Primary_somatosensory_cortex_BA1_L; 34.0% GM_Primary_somatosensory_cortex_BA3b_L; 22.0% GM_Premotor_cortex_BA6_L; 20.0% GM_Primary_motor_cortex_BA4p_L; 20.0% GM_Primary_motor_cortex_BA4a_L; 16.0% GM_Primary_somatosensory_cortex_BA2_L; 15.0% WM_Corticospinal_tract_L; 10.0% GM_Superior_parietal_lobule_5L_L	65.0% Left_Postcentral_Gyrus; 13.0% Left_Precentral_Gyrus	Postcentral_L
3	45	-40	31	-5,685	2020	20.0% GM_Anterior_intra-parietal_sulcus_hIP2_R; 14.0% GM_Inferior_parietal_lobule_PFm_R; 10.0% GM_Anterior_intra-parietal_sulcus_hIP1_R	6.0% Right_Supramarginal_Gyrus_posterior_division	SupraMarginal_R
9	-32	-57	-18	-5,765	392	0% no_label	78.0% Left_Temporal_Occipital_Fusiform_Cortex; 11.0% Left_Occipital_Fusiform_Gyrus	Fusiform_L
1	-53	-9	48	-7,112	455725	70.0% GM_Premotor_cortex_BA6_L; 36.0% GM_Primary_somatosensory_cortex_BA1_L; 21.0% GM_Primary_motor_cortex_BA4a_L; 10.0% GM_Primary_somatosensory_cortex_BA3b_L; 10.0% GM_Primary_motor_cortex_BA4p_L	67.0% Left_Precentral_Gyrus; 14.0% Left_Postcentral_Gyrus	Postcentral_L
1	27	2	-15	-13,627	455725	27.0% GM_Amygdala_superficial_group_R	49.0% Right_Amygdala	Amygdala_R